Functions and Water Interaction Mechanisms of Micro/Nanostructures on Insect Cuticle Surfaces

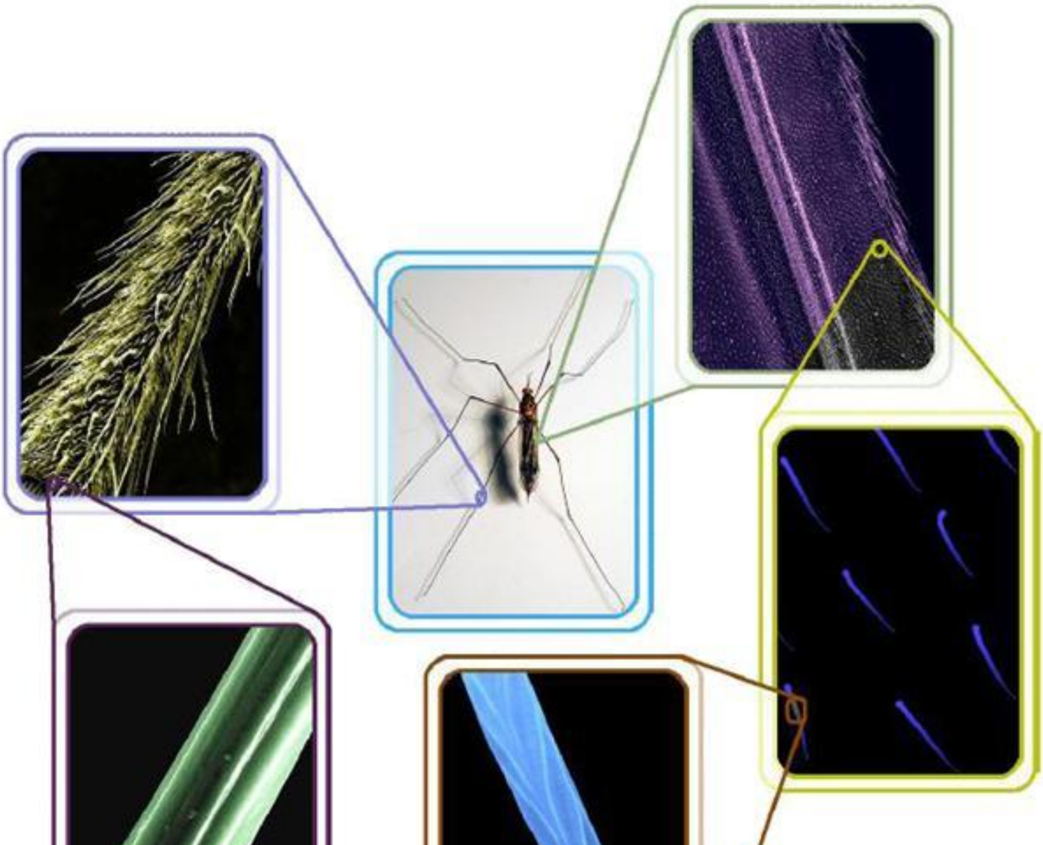

By Simon Hsuan-Ming Hu

Submitted in total fulfilment of the requirements of the Degree of Doctor of Philosophy
School of Pharmacy and Molecular Sciences - James Cook University 2014

STATEMENT

This work has never previously been submitted for a degree or diploma in any University and to the best of my knowledge and belief contains no material previously published or written by any other person except where due reference is made.

Parts of the work described here have been previously published in the following publications:

Hu, H. M.; Watson, J. A.; Cribb, B. W.; Watson, G. S. Fouling of Nanostructured Insect Cuticle: Adhesion of Natural and Artificial Contaminants. *Biofouling* **2011,** *27* (10), 1125-1137.

Hu, H. M. S.; Watson, G. S.; Cribb, B. W.; Watson, J. A. Non-Wetting Wings and Legs of the Cranefly Aided by Fine Structures of the Cuticle. *Journal of Experimental Biology* **2011,** *214* (6), 915-920.

Hu, H. M.; Watson, G. S.; Watson, J. A.; Cribb, B. W. Multi-Functional Insect Cuticles: Informative Designs for Man-Made Surfaces. *World Academy of Science, Engineering and Technology* **2011,** *5* (59), 1370-1371.

Watson, G. S.; Hu, S.; Cribb, B. W.; Myhra, S.; Brown, C. L.; Watson, J. A. Micro and Nano-Structures Found on Insect Wings - Designs for Minimising Adhesion and Friction. In *2nd International Conference on Advanced Nano Materials*; Journal of Nanoscience and Nanotechnology: Aveiro, Portugal **2008**; Vol. 8.

Watson, J. A.; Cribb, B. W.; Hu, H. M.; Watson, G. S. A Dual Layer Hair Array of the Brown Lacewing: Repelling Water at Different Length Scales. *Biophysical Journal* **2011,** *100* (4), 1149-1155.

Watson, G. S.; Brown, C. L.; Myhra, S.; Roch, N. C.; Hu, S.; Watson, J. A 'Patterning' Frictional Differentiation to a Polymer Surface by Atomic force Microscopy - art. no. 60371B. In *Device and Process Technologies for Microelectronics, MEMS, and Photonics IV*, Chiao, J. C.; Dzurak,

A. S.; Jagadish, C.; Thiel, D. V., Eds.; Spie-Int Soc Optical Engineering: Bellingham, **2006**; Vol. 6037, pp B371-B371.

Chapter #	Details of publication(s) on which chapter is based	Nature and extent of the intellectual input of each author	I confirm the candidate's contribution to this paper and consent to the inclusion of the paper in thisthesis
4~6	Fouling of nanostructured insect cuticle: adhesion of natural and artificial contaminants.	Gregory Watson: Project guidance and advisor	
		Jolanta Watson: Project guidance and advisor	
		Bronwen Cribb: SEM imaging & Entomological input	
		Hsuan-Ming Hu: Experiments and results analysis	
7	Non-wetting wings and legs of the cranefly aided by fine structures of the cuticle	Gregory Watson: Project guidance and advisor	
		Jolanta Watson: Project guidance and advisor	
		Bronwen Cribb: SEM imaging & Entomological input	
		Hsuan-Ming Hu: Experiments and results analysis	

* 'Hu, H. M.', 'Hu, H. M. S.' and 'Hu, S.' are all initials of Simon Hsuan-Ming Hu.

Simon Hsuan-Ming Hu

ACKNOWLEDGEMENT

This incredible journey has been made possible because of the generous support from many people.

The most invaluable guidance came from my University parents Dr. Gregory Watson and Dr. Jolanta Watson. Thanks for unplugging me into the real world and showing me the way of The Force. They have been there for me since before the beginning of this candidature, patiently mentoring me to gain confidence and ambition not just for science but in many aspects of life.

Thanks also to Professor Peter Junk for getting me over the line as well as Dr Bronwen Cribb for her expertise in Entomology and Scanning Electron Microscopy and the supportive colleagues and friends from the School of Pharmacy and Molecular Sciences.

Lastly thanks to the Graduate Research School for the guidance and the kind scholarship to ease my financial burdens.

ABSTRACT

Understanding the tribology and adhesion between surfaces at a wide range of length scales is essential for creating the next generation of contamination resistant and super adhesive surfaces. Adhesion and frictional control between solid-solid or solid-liquid surface contacts impact on all aspects of life and is important in a variety of industrial applications and future technologies. Many studies have investigated micro-structures (arrays) on the scale from a few to a hundred micrometres but so far researches on smaller scales have been limited. This study will focus on the contact area and wettability of surfaces on the micro/nanoscale.

Insect cuticles, one of the most noteworthy naturally occurring nano-composite materials are considered a free and potentially rich source of technology 'invented' by natural selection. Many are multi-functional with efficiencies beyond that of artificially created surfaces. Insects with large wings are unable to clean themselves with their extremities. Contaminants (water and/or contaminating particles) on the wing have a negative effect on the flight capabilities of insects. Insects with a very high wing surface-body mass ratio (SM) index are more susceptible and greatly affected by contamination. A number of these insects exhibit unique structures to decrease wing contamination.

Recent studies show that some of these cuticles exhibit impressive superhydrophobic properties. Little was understood about their surface characteristics on the nano-scale prior to the invention of instrumentations and techniques such as the Atomic Force Microscope (AFM) and the Scanning Electron Microscope (SEM). This study utilises the AFM to investigate the tribological properties, including adhesional properties, on a range of insect wing membranes at different length scales. The SEM has been useful to visualise and analyse the nanostructures and properties of surfaces.

New methodologies have been employed for micro and nano-scale investigation to determine the functions, functional efficiencies and potential applications of a range of micro/nanostructures recently found on the cuticle of insect wings. Interactions of natural contaminant mimicking spherical surfaces (of different size and chemistry) with insect cuticles were observed and tribological properties were measured. The project will address

a number of scientific problems focusing on the control of adhesional properties between surfaces (solid-solid and solid-liquid interactions). A newly discovered water ridding mechanism due to hairs on the lacewing could lead to the creation of a true water repellent surface.

TABLE OF CONTENTS

LIST OF FIGURES

LIST OF TABLES

LIST OF EQUATIONS

LIST OF ABBREVIATIONS AND SYMBOLS

α	half angle of the tip
AFM	atomic force microscope
C	slope of approach curve of the cantilever pushing against an incompressible surface
CA	contact angle
CAH	contact angle hysteresis
D	deflection of the cantilever
ddH_2O	double-distilled water
Δx_{tip}	tip displacement
E	Young's Modulus
E^*	Relative Young's Modulus
E_{sample}	Young's Modulus of the sample
E_{tip}	Young's Modulus of the tip
ϕ	angle of tip displacement
F	meniscus force between a sphere and a flat surface
f_1	the surface area fraction under the droplet in contact with the solid substrate
f_{air}	tip displacement as an angle of twist
ϕ_B	ratio of the basal area of the protrusion over the total area
F_{cone}	loading force from a cone shaped tip
F-D	force distance
F_L	lateral loading force of the AFM cantilever
F_N	normal loading force of the AFM cantilever
F_{STW}	solvent adhesive forces
F_{vdW}	van der Waal forces
G	shear constant
γ	solid-vapour interfacial energies/tensions
γ_{LV}	solid-vapour interfacial energies/tensions
γ_{SL}	solid-liquid interfacial energies/tensions

γ_{SV}	**liquid-vapour interfacial energies/tensions**
h	**height of tip**
I_A	**intensity of the light received by quadrant A of the PSPD**
I_B	**intensity of the light received by quadrant B of the PSPD**
I_C	**intensity of the light received by quadrant C of the PSPD**
I_D	**intensity of the light received by quadrant D of the PSPD**
k	**cantilever spring constant of the bending of the cantilever in the z-direction**
k_0	**contributing to the tip displacement in the y-direction**
k_{Cb}	**cantilever spring constant of the shear deformation of the tip in the x-direction**
k_{Csx}	**cantilever spring constant of the shear deformation of the tip in the z-direction**
k_{Csz}	**standard cantilever spring constant**
k_L	**lateral force constant of the AFM cantilever**
k_N	**normal force constant of the AFM cantilever**
k_T	**twisting force constant of the AFM cantilever**
L	**cantilever length**
M	**end mass**
m	**mass of beam cantilever**
μ	**Poisson's ratio**
PDMS	**polydimethylsiloxane**
PMMA	**Poly[methyl methacrylate]**
PSPD	**position sensitive photo-detector**
θ_0	**static CA formed with a smooth surface**
θ_a	**advancing contact angle**
θ_{air}	**CA formed with air = 180°**
θ_C	**static apparent CA of a droplet in the Cassie-Baxter regime**
θ_r	**receding contact angle**
θ_w	**static apparent CA of a droplet in the Wenzel regime**
ρ	**material density**
r	**roughness**
R	**tip radius**
r_2	**roughness on surface features (secondary roughness)**

RH	**relative humidity**
σ	**indentation**
SEM	**scanning electron microscope**
SM	**surface body mass ratio**
t	**cantilever thickness**
υ_0	**resonance frequency of the cantilever**
υ_1	**perturbs the resonance frequency of the cantilever**
w	**cantilever width**
X	**horizontal position of the centre of the light spot with respect to the centre on the quadrant detector**
Y	**vertical position of the centre of the light spot with respect to the centre on the quadrant detector**

FEATURE ARTICLE

INSIDE JEB (March 15, 2011)

NON-STICK HAIRS KEEP CRANEFLIES DRY

Large animals think nothing of walking through a heavy mist: water droplets simply role off their hides. However, smaller insects are at constant risk of entrapment by the sticky forces of surface tension. Craneflies, which set up home in boggy settings and riverbanks, routinely encounter damp surfaces and mist that could prove fatal, yet they shrug off droplets with ease and can even stand on water. Jolanta Watson and colleagues from James Cook University and the University of Queensland, Australia, decided to take a close look at the insect's fragile legs and wings to find out how craneflies avoid getting stuck in water.

Photographing cranefly legs at increasing magnification, the team could see that the insect's legs are covered with water-repelling hairs: thick long (90 μm) hairs with a rough grooved surface, shorter thick curved hairs, even shorter fine hairs and the shortest hairs of all found clustered at the base of the longest thick hairs. The insect's wings are also covered in fine hairs, with 12 μm long hairs distributed evenly across the membrane and 90 μm long hairs coating the wing veins.

To find out how repellent the hairy surfaces are, the team photographed water droplets on the insect's legs and wings. They saw that instead of spreading over the insect, the droplets formed perfect spheres, characteristic of the way water is repelled by a hydrophobic surface. And when they laid a cranefly leg on water, the hairs formed tiny dimples in the surface instead of piercing it.

Finally, the team tested how the grooves on the longer hairs help the insects repel water by coating the long hairs with hydrophobic polydimethylsiloxane to fill the grooves. Poking coated and uncoated hairs into water droplets, the team could see that the coated hairs no longer repelled water and penetrated the droplets with ease, while the uncoated hairs were unable to pierce the droplets.

So craneflies avoid getting trapped in sticky water with a coating of rough hydrophobic hairs. Watson and her colleagues are keen to design cranefly-inspired water-repelling and self-cleaning surfaces.

(See Chapter 7)

1 INTRODUCTION

The promise of controlling the tribology and adhesion between surfaces at various length scales, and more importantly an advanced understanding of the processes involved, will ultimately lead to the next generation of contamination resistant and super adhesive surfaces (Blossey, 2003). Adhesion and frictional control between surfaces, whether as solid-solid or solid-liquid contacts, impact on all aspects of life from the need to keep surfaces clean, to the state-of-the-art of droplet-based micro-fluidics systems (Blossey, 2003, Lehto et al., 1999). The Holy Grail in regards to adhesion would be the ability to fabricate surfaces at two extremes - a surface that adheres to anything and a surface that nothing will adhere to.

Controlling adhesion between solid-solid and solid-liquid contacts is critical in a number of industrial applications and more important for predicted future technologies. For example, advances in nanotechnology, including micro/nanoelectromechanical systems (MEMS/NEMS) has stimulated development and the need to design surfaces with ultra-low adhesion (Burton and Bhushan, 2005). When considering the functionalities of micromechanical and nano-sized devices that require materials with tailored tribological properties, the issues addressed in this project become more critical (Burton and Bhushan, 2005). The contact area and wettability will affect the adhesion, friction and wear, and may inhibit, possibly prohibit, the functionalities of micromechanical and nano-sized devices, as well as impact on their ultimate life expectancy (Burton and Bhushan, 2005, Abdelsalam et al., 2005, Ando and Ino, 1998). Many studies have investigated well-ordered structures (arrays) on the scale from a few to a hundred micrometres. However, so far there have been only a limited number of studies of nm-sized structures (Burton and Bhushan, 2005).

Naturally occurring nano-structures are a much-neglected, but potentially rich, source of products exhibiting finely tuned functional efficiencies. While the pharmaceutical industry has long recognized the value of natural compounds, the emerging industries based on nanotechnology have so far made relatively little use of ‘free’ technology that has been ‘invented’ by the imperatives of species survival. One of the most noteworthy naturally occurring nano-composite material is the insect cuticle (Vincent and Wegst, 2004). Many micro/nano-structures found on cuticles of insects are multi-functional and some have efficiencies beyond that of artificially created surfaces. Recently natural micro- and nano-structures found on insect cuticles have been shown to exhibit a range of impressive and remarkable properties such as superhydrophobicity, directed wetting and ultra-low adhesion (Parker and Lawrence, 2001, Gorb et al., 2000, Watson et al., 2008b).

A study and seminal work by Wagner *et al* showed that there was a correlation between contaminability, wettability and the wing area of many insects (Wagner et al., 1996). They showed that large winged insects such as butterflies demonstrated extremely low contamination and have very unwettable wings, while smaller winged insects (e.g., flies) showed the opposite trend. Additional weight due to contamination (water and/or contaminating particles) can potentially have a detrimental effect on the flight capabilities of large wing insects (Wagner et al., 1996). Insects with a very high wing surface-body mass ratio (SM) index will have an even greater susceptibility to these effects. A number of insects which have large wings and/or high SM values exhibit unique structures to combat wing contamination from foreign bodies such as water and particulates (Gorb et al., 2000, Fang et al., 2007, Large et al., 2007, Tada et al., 1998) . The result in most instances provides an extremely hydrophobic and in some cases superhydrophobic surface. These superhydrophobic surfaces will not only reduce the effects of contact with particulates but also promote other functional properties (Watson et al., 2008b) such as self-cleaning for removing foreign bodies such as dust (Wagner et al., 1996).

The mechanisms and functional efficiency of nano-structures identified on a variety of insects has as yet not received a great deal of attention. One of the major obstacles to a better understanding of these structures has been the inability to undertake surface and interface characterization on the nano-scale. The invention of instrumentation and techniques such as the Atomic Force Microscope (AFM), and the latest generation of imaging and analytical electron-optical techniques has given the scientific community new tools with which to visualise and analyse the structure and properties of surfaces and interfaces on the nano- and meso-scale.

In this study the latest instrumentation and methodologies for nano and micro-scale investigation was utilized in order to determine the function, functional efficiency and potential applications of a range of novel nano- and-micro scale structures recently discovered by Watson *et al.* (Watson et al., 2008b, Watson and Watson, 2004, Watson et al., 2007) and by others (Wagner et al., 1996) on the cuticle of insect wings. In particular, this study will utilise the AFM to investigate the tribological properties including adhesional properties on a range of insect wing membranes at different length scales.

A previously unreported water ridding mechanism is included in Chapter 8. Understanding surface functional mechanisms provides clearer directions towards creating new and more efficient surface functionalities to help meet the standard and demands of upcoming nanotechnologies.

Information required prior to the experiments are contained in Chapter 2 and 3. Chapter 4, 5 and 6 investigate the insect wing structures on a range of species and their nano, micro and macro scale properties particularly wetting (Chapter 5) and adhesion with solids (Chapter 6). Chapter 7 highlights the importance and efficiency of surface structures in non-wetting of the hairs on craneflies. Moving onto a larger insect for a more in-depth investigation of the role of cuticle hairs Chapter 8 examines the mechanistic processes involved in wetting prevention, self-cleaning and water repelling by the hairs on lacewing cuticles.

2 THEORETICAL BACKGROUND

2.1 THE ATOMIC FORCE MICROSCOPE (AFM)

The Atomic Force Microscope (AFM) is a sub-family member of Scanning Probe Microscopy (SPM) and in its early days was typically used for imaging beyond the optical microscope limit. However, its unique imaging method of using a probe to interact with the sample surface allows other surface features/properties to be determined. The AFM's potential as a force sensing instrument on surfaces is a significant factor contributing to its popularity. The basic elementary function common to all SPMs is using the probe to interact with surfaces. At high resolutions this interaction can occur primarily between several atoms on the apex of the tip and atoms on the surface. The amount of interaction can be plotted as a function of the lateral position to produce an image. Its unique imaging method of using a probe to interact with the sample surface allows other surface properties such as surface adhesive forces, frictional forces and material spring constants (Gibson et al., 1997, Watson, 2001) to be determined as well as surface manipulation (Watson et al., 2006a, Watson et al., 2008c, Watson, 2005).

2.1.1 AFM COMPONENTS & BASIC OPERATIONS

Typically the main elements of the AFM consist of the laser, detector, scanner and most importantly the probe. The probes consist of a cantilever and tip which constitutes the interface between the sample and the other components of the AFM. The other two important components of the AFM are the laser and the position-sensitive-photo-detector (PSPD) which combine to monitor the deflection of the cantilever. During the AFM operation, the laser reflects off the top surface of the cantilever and its intensity is received typically by the four quadrants on the PSPD. The amount of intensity each quadrant receives during scanning will constantly change as the tip interacts with the sample surface.

Generally for imaging the tip is held in contact with the surface, with a piezoelectric scanner responsible for moving the sample or the probe in a raster pattern during the process of operation. Most AFM instruments allow the user to set various scanning parameters: scan speed, scan area; resolution (i.e., increment in the y-direction), scan angle, response sensitivity (feedback) etc.

As the tip moves over a structure, the cantilever will bend, buckle and/or twist corresponding to any change in topography height, adhesion and surface friction. The software converts the cantilever movements into a topographical image or a surface force map.

The PSPD implemented in the instrumentation used in this thesis is composed of four separate quadrants (ABCD (Figure 2.1-1)) where the position of the centre of the laser is determined from the relative intensities received by the quadrants. The top and bottom part of the PSPD (AB and CD respectively) detects bending (and buckling in some cases) of the cantilever which corresponds to changes to the sample topography given by Equation 2.1-1.

$$Y = \frac{(I_A + I_B) - (I_C + I_D)}{I_A + I_B + I_C + I_D}$$

Equation 2.1-1

Where *Y* is the vertical position of the centre of the light spot with respect to the centre on the quadrant detector and I_A, I_B, I_C and I_D are the intensities of the light received by each of the quadrants *A*, *B*, *C* and *D* respectively.

Similarly, the quadrant pairs AC and BD measure the lateral twisting of the cantilever due to the frictional/lateral forces with the sample given by Equation 2.1-2.

$$X = \frac{(I_A + I_D) - (I_B + I_C)}{I_A + I_B + I_C + I_D}$$

Equation 2.1-2

Where *X* is the horizontal position of the centre of the light spot with respect to the centre on the quadrant detector.

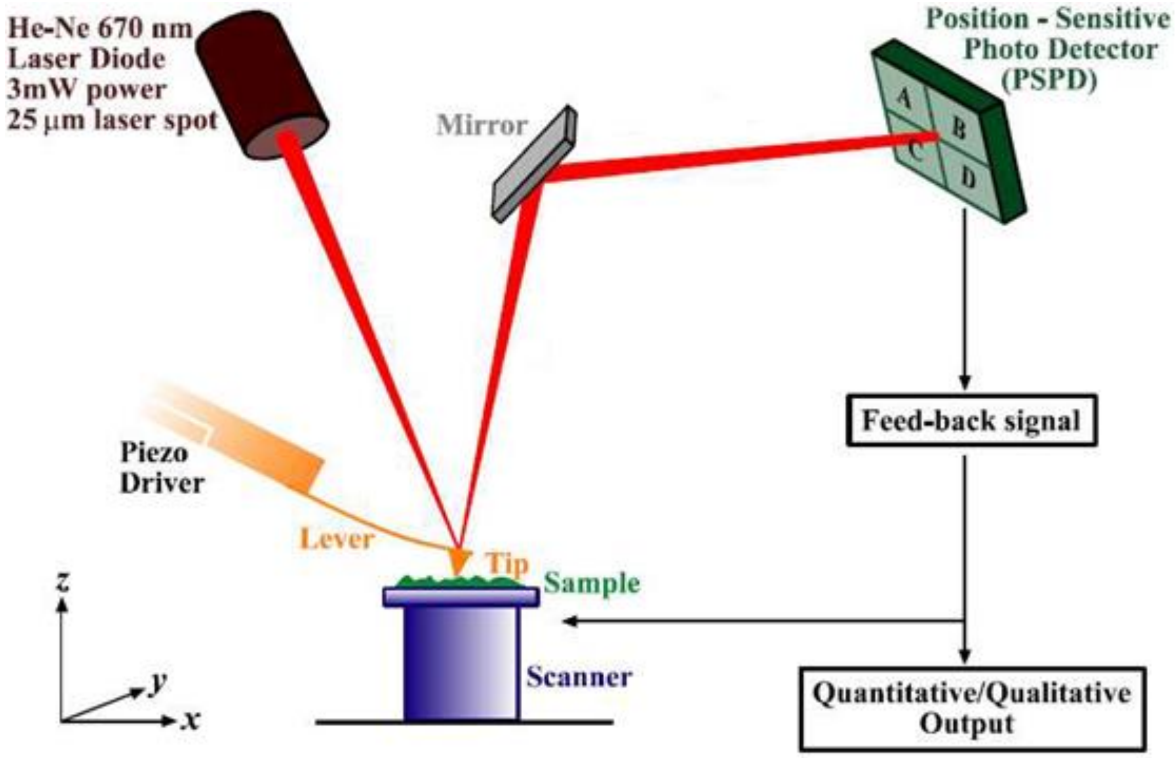

Figure 2.1-1. The path of the laser in a typical AFM instrument reflecting off the cantilever, mirror and onto the detector.

2.1.1.1 THE CANTILEVER & THE TIP/PROBE

Interaction with the sample surface is probed at the free end of a cantilever. Cantilevers are available in a wide range of dimensions/shapes, chemistries and stiffnesses. Most of the cantilevers consist of a sharp tip at the free end. The tips are also commercially available in a wide variety of dimensions/shapes and chemistries.

Choosing between the wide range of AFM probes will depend on the purpose and the surface being scanned. Beam shaped cantilevers were predominately used for the studies in this thesis (Figure 2.1-3) (discussed in greater detail in sections 2.1.1.2, 2.1.1.3). V-shaped cantilevers were designed to minimise twisting and improve topographical imaging quality, however Sader (Sader et al., 2003) suggests that V shaped cantilevers actually twist more than beam shaped cantilevers. Tipless cantilevers can be employed for attachment of particles of specific sizes and chemistry both anthropogenic and natural in origin. For example, particles such as pollen and silica beads which mimic natural contaminants can be attached to tipless cantilevers under an optical microscope (Section 3.1.3 for hair attachment procedure). The particles can be characterised by scanning over an array of spikes (with radius << radius of beads) i.e. reverse-imaged (Hellemans et al., 1991) (Figure 2.1.2). Resonance frequency measurements can be carried out prior and after their attachment to measure other parameters such as spring constants.

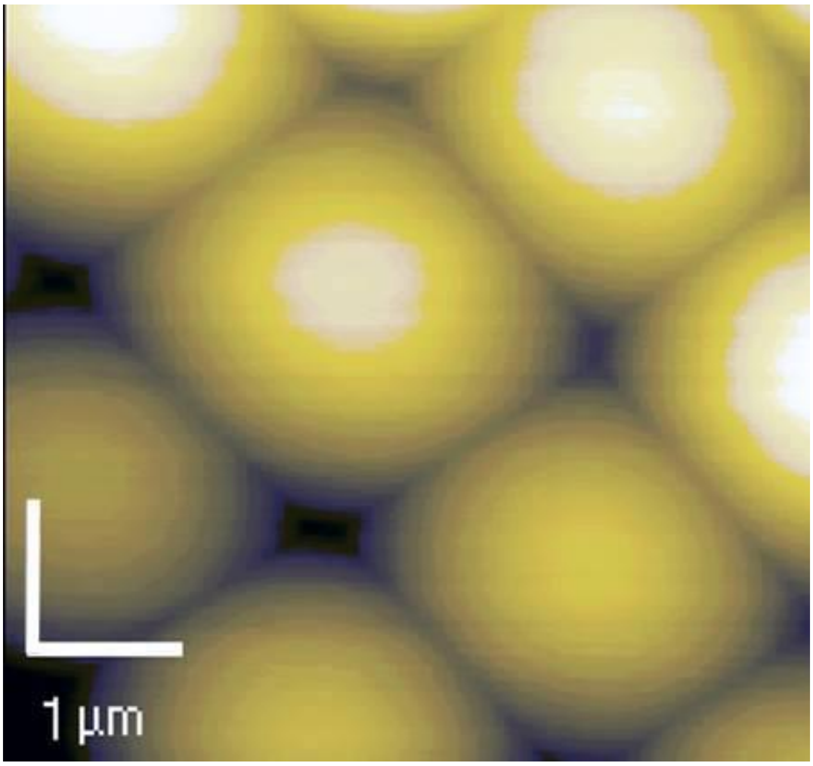

Figure 2.1-2. Reverse image of a 31 μm bead revealing a clean surface.

The deflections of the cantilever due to any surface features allow a topographical image or a map of the force (e.g., frictional) to be produced. The bending (in the z-direction) and twisting (in the x-direction) of the cantilever corresponds predominantly to changes in topography and the surface friction, respectively (refer to Figure 2.1-3 for the directions). The choice of cantilever force constants will depend on the surface being scanned and the magnitude of the interacting forces.

During imaging in the common constant force mode, a feedback system responds to the deflections of the lever to maintain constant loading force by moving the probe up or down to counter the deflection due to a bump or depression, respectively. For contact mode imaging keeping a constant loading force is important in both topographical and lateral scanning. If the force exerted on the surface is great enough, manipulation of the surface and the creation of structures on the micro and nano-scale can occur (Watson et al., 2006b).

2.1.1.2 CANTILEVER LOADING (NORMAL) FORCE CONSTANT

The spring constant (k_N) is dependent on the cantilever's dimensions and material properties. Obtaining k_N is especially important in the force-distance operation (Sections 2.1.4 and 2.1.5). Silicon nitride and silicon are two of the most common materials for probes. For a beam-shaped cantilever with dimensions (length, width and thickness (*L, w, t*)) and Young's Modulus (*E*) (= 130 Gpa for Si (Hopcroft et al., 2010)) the spring constant is:

$$k_N = \frac{Et^3 w}{4L^3}$$

Equation 2.1-3

V-shape cantilevers are often approximated as two parallel beams and Equation 2.1-3 becomes $k_N = \frac{Et^3 w}{2L^3}$ where *L* in this case is the distance of the tip from the cantilever (Sader, 1995). Measuring the lever parameters like cantilever thickness (typically a few μm) to a high accuracy requires the Scanning Electron Microscopy (SEM). Reflective or additional coatings of different physical properties on cantilevers can alter the spring constant (by less than 0.005N/m for the cantilevers used in the experimental sections).

There are methods which reduce or eliminate the power of the dimension terms by introducing other terms such as the resonance frequency of the cantilever (υ_0) and cantilever material density (ρ). The resonant frequency of the cantilever is also dependent on the cantilever's dimensions and density of its material and hence can be used to replace the thickness term in Equation 2.1-3. The spring constant of a beam shaped cantilever can be obtained using Equation 2.1-4:

$$k_N = 2\pi^3 L^3 w \left(\frac{\rho^3}{E} \right)^{1/2} \upsilon_0{}^3$$

Equation 2.1-4

Where ρ = 2340kg/m^3 (in this case for Si) (Watson, 2005).

For non-tipless cantilevers (where L/w > 5) (Sader et al., 1999)), the extra weight (*M*) due to the tip perturbs the resonance frequency measurement to become υ_1 (Harris and Crede, 1976, Jing et al., 2007):

$$\upsilon_1 = \frac{1}{2\pi}\sqrt{\frac{k_N}{M + 0.2427m}}$$

Equation 2.1-5

for an extra mass of ~1/3 of the beam lever, υ_0 could be dampened by ~15% and hence reducing k_N by ~34%.

Static loading methods are simple and direct and are applicable to various cantilevers and can also be used to measure the stiffness of microtrichia (small hairs on the wings and bodies of insects), as described in greater detail in Section 3.1.2. The cantilever's deflection due to a known loading force applied above the cantilever tip is obtained to determine the spring constant according to Hooke's law (Force = k_N X deflection). Using an AFM with a calibration cantilever (with a well determined 'known' spring constant) an unknown cantilever's force constant can be accurately determined using force-distance (f-d) curves. The slope of the curve *D* represents the deflection of the cantilever and hence k_N is given by (Gibson et al., 1996):

$$k_N = \frac{K_0}{C/D - 1}$$

Equation 2.1-6

where K_0 is the standard cantilever spring constant and *C* is the slope of the cantilever pushing against an incompressible surface (slope of approach curve 1, Figure 2.1-10).

The accuracy depends on the precision of the loading force and the point of loading which is associated with the dexterity, judgement and experience of the operator (Gibson et al.,

1996) however accuracy is generally lower for cantilevers with low spring constants (i.e. k_N < 1N/m) (Butt et al., 2005, Ying et al., 2007).

For beam shaped cantilevers, the inaccuracies can be reduced by taking deflections due to loading forces applied along the cantilever(Ying et al., 2007). The offset in the loading point ΔL on a beam cantilever will cause the spring constant to change by Δk_N approximated by (Ying et al., 2007):

$$\Delta k_N = -k_N \frac{3\Delta L}{L}$$

Equation 2.1-7

for $|\Delta L| << L$.

An image of the loading point allows the location to be chosen close to the tip of the unknown cantilever. The unknown cantilever should have a spring constant within an ideal range between (Gibson et al., 1996) 0.3K_0 to 3.0K_0,. Using several cantilevers within that spring constant range for calibration will improve accuracy.

Other alternative methods of determining spring constants include measuring the resonance frequency under different density liquids (Sader et al., 1999) or with a known mass attached (Harris and Crede, 1976, Jing et al., 2007).

In the experiments involved in this thesis, resonance and static loading techniques using pre calibrated cantilevers were utilised to accurately determine cantilever and hair spring constants, respectively. As well, whenever possible, measurements on several different surface samples were taken using the same set of cantilevers under the same conditions to compare adhesion values.

2.1.1.3 CANTILEVER FORCE CONSTANTS DEFORMATION DURING AFM OPERATION

Bending, buckling and twisting of the cantilever are an important part of the AFM operation. These deformations are results of tip interactions with the local forces of the sample surface. Forces acting along the z-, y- and x-direction correspond to the bending (in the normal direction), (longitudinal) buckling and twisting of the cantilever, respectively. The bending of the cantilever in the z-direction (as discussed above) will also contribute to the tip displacement in the y-direction. The force constants k_N, k_L, k_T shown in Figure 2.1-3 are given by Equation 2.1-3 (Section 2.1.1.2), Equation 2.1-8 and Equation 2.1-9 (Gibson et al., 1997, Ogletree et al., 1996, Warmack et al., 1994) which describes the deformation of the lever by the lowest order modes of a long thin beam:

$$k_L = \frac{k_N L^2}{3h^2}$$

Equation 2.1-8

$$k_T = \frac{Gwt^3}{3Lh^2}$$

Equation 2.1-9

where *h* is the height of the tip, *G* is the shear constant of the cantilever = $E[2(1-\mu)]^{-1}$ (Watson, 2005) and μ is the Poisson's ratio (≈0.4 in this case for Si)(Watson, 2005).

If the normal spring constant of the probe is known then the lateral twisting force constant can be calculated using Equation 2.1-10:

$$k_T = k_N \left[\frac{2L^2}{3(1+\mu)h^2} \right]$$

Equation 2.1-10

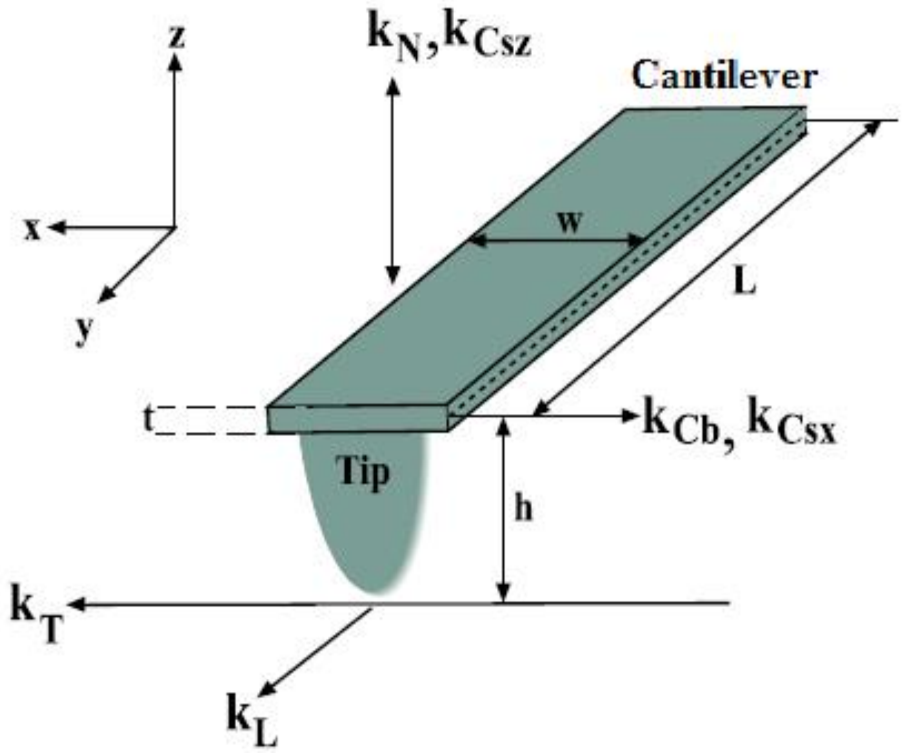

Figure 2.1-3. The relevant force constants of a beam shaped cantilever.

The bending of the cantilever in the z-direction will also contribute to the tip displacement in the y-direction which is typically small and is neglected in this work. This spring constant k_{Cb} is given by (Watson, 2005):

$$k_{Cb} = k_N \frac{w^2}{t^2}$$

Equation 2.1-11

The shear deformation of the tip will be small and will be also neglected. However the deformation in the x- and z-direction are respectively given by (Watson, 2005):

$$k_{Csx} = G_x t \frac{w^2}{L}$$

Equation 2.1-12

$$k_{Csz} = G_z t \frac{w^2}{L}$$

Equation 2.1-23

2.1.2 IMAGING

During scanning, the AFM instrumentation (JEOL and the Topometrix instruments use in this thesis (Section 3.1)) operate by measuring tip deflections and scanner motion (generally in a raster pattern). The deflections of the cantilever due to any surface features allow a topographical image or force map to be produced. The bending (in the z-direction) and twisting (in the x-direction) of the cantilever corresponds to changes in topography height (or adhesion in the non-contact cases, see Section 2.1.4) and the surface friction (Section 2.1.5), respectively. In this study, the fast scanning direction of the tip is always along the x-direction by convention and the loading force is always applied in the z-direction (Figure 2.1-3).

A requirement of constant force imaging is that deflection of the cantilever needs to be kept as constant as possible by the feedback system. This means when the tip travels over a rise or a drop on the surface, the deflection in the cantilever sensed by quadrant changes on the PSPD cause the stage/sample to move down or up to counter the deflection. The loading force can be varied depending on the experimental requirements, e.g., high for incompressible surface imaging or intentional surface manipulation (Blach et al., 2004, Watson and Watson, 2008, Watson, 2005, Watson et al., 2006c), and generally low for biological/compliant surfaces (e.g., cells, polymers) (Meyer, 2004, Watson, 2001, Watson, 2005). Unless manipulation is intended, the amount of force applied from the tip to the surface should not cause irreversible damage to the sample. The choice of cantilever spring constant will depend on the surface being scanned. The spring constant of the elastic surface should be close to the spring constant of the lever for general purposes. For a surface with higher friction, a stiffer or V-shaped cantilever can reduce twisting during scanning.

Tip geometry, the condition of the tip and their adhesiveness have a decisive role in the overall image quality as well as lateral force and force-distance measurements. Wearing and breakage of the tip and unwanted adherent contaminates can significantly modify the interaction between the probe and the sample.

2.1.2.1 TIP CONTAMINATION AND BREAKAGE

The condition of the tip determines the quality of the image where the lateral resolution is dependent on the radius of curvature of the tips. Tip geometry and their adhesiveness have a decisive role in the overall image quality. For high precision scanning, contaminated tips are a big problem. Tip contamination happens when an unwanted substance/material attaches itself onto the tip. It occurs particularly with soft, adherent polymer samples especially when the tip collides with steep features or loose particles. Unwanted adherents may reduce the clarity of the image as seen in Figure 2.1-4 (Watson and Watson, 2008) (sometimes producing a double image called 'ghost') and also affect the adhesion section on the force-distance curve.

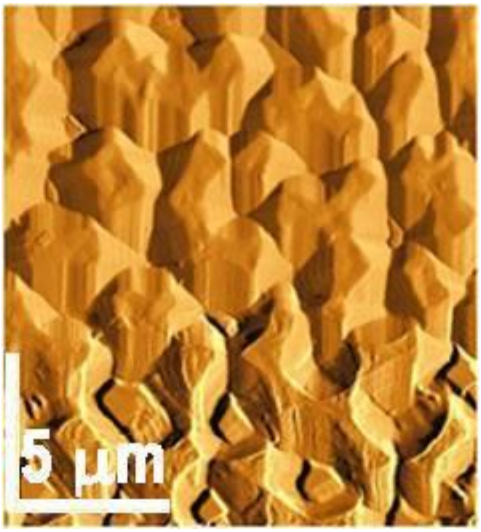

Figure 2.1-4. Shows an AFM image where the top half was scanned with a contaminated tip. The contaminant was detached by the scanning procedure around half way through the imaging process and hence the image became more detailed.

Wearing and breakage is inevitable for all AFM tips. Usually wearing results in the tip becoming blunt which means the tip has an increased contact area with the sample surface and produces a less detail image. The interaction between a broken tip and the sample surface is also different as a different tip shape changes the resolution, indentation and adhesion with the surface. Ghost images (Figure 2.1-5 (A)). that are generally produced by tip contamination can also happen when a tip breaks into two sharp ends (Figure 2.1-5 (B)).

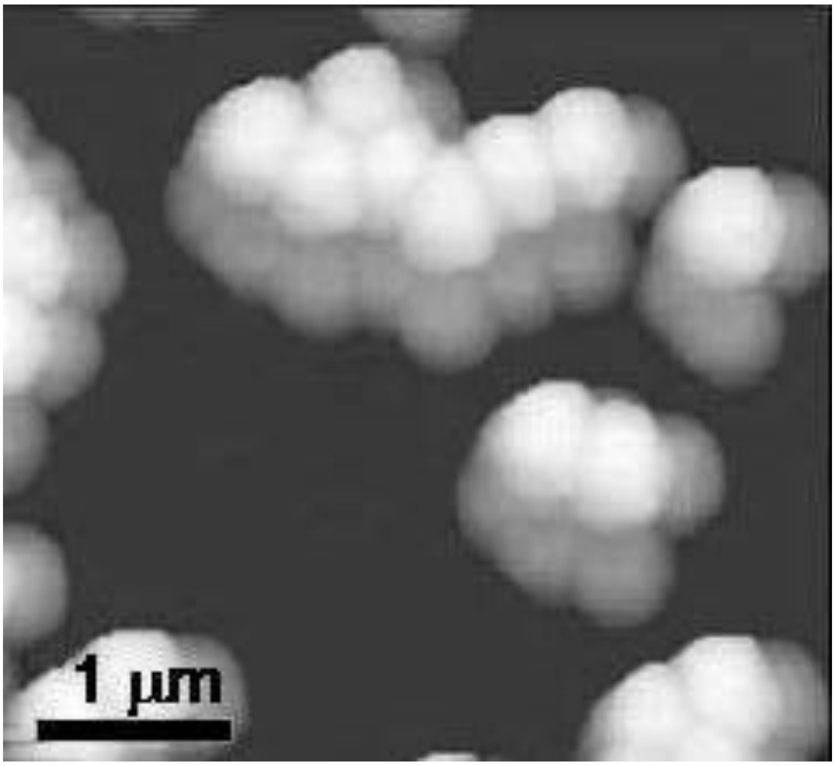

Figure 2.1-5. (A). Double tip resulting in a ghost image to be produced.

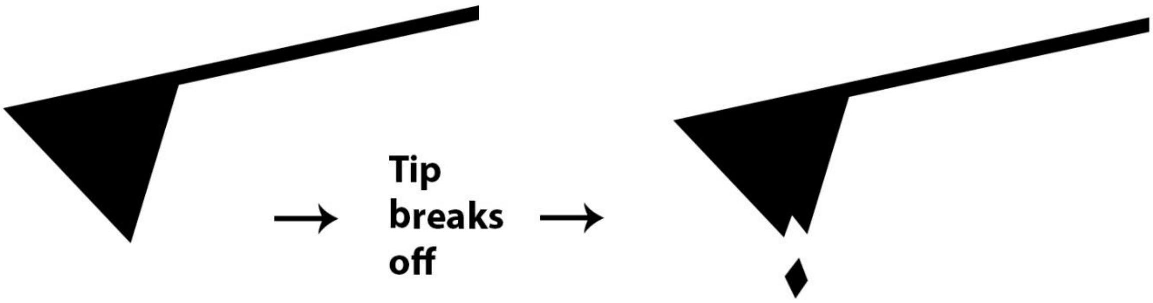

Figure 2.1-6. (B). The end of the tip chips off creating a double tip.

2.1.2.2 INACCESSIBLE AREAS DURING IMAGING OPERATION

There are some structures of samples that are unable to be scanned. These structures include holes (Figure 2.1-6 (A)) which are smaller than the tip radius or deeper than the tip height. As a result, the topography of the hole obtained will represent the shape of the tip and not the actual hole itself. Other features include steep surfaces and steeply curved surfaces (Figure 2.1-6 (B)) where the probe is unable to proceed into the area making contact at the tip apex. An example of this is the inside of a small cylindrical structure. Finally Figure 2.1-6 (C) shows the area beside a steep bump, which is usually left out by the tip scanning in the direction from the other side.

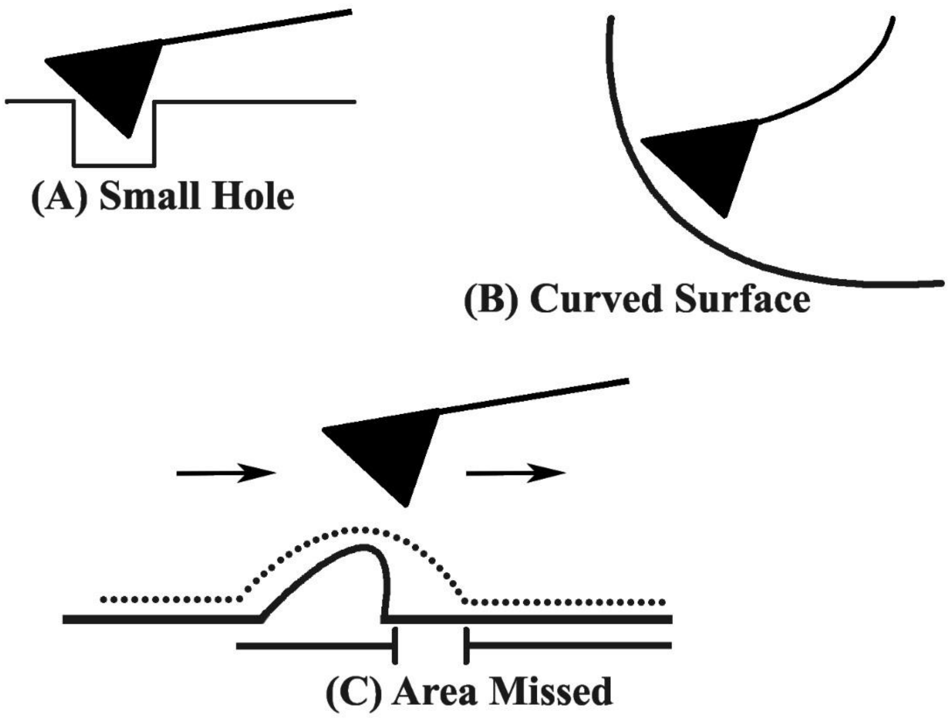

Figure 2.1-7. (A) Shows the tip is unable to reach the bottom of a small hole. (B) The large curved surface does not allow the tip to proceed into it. (C) A tip scans over a bump on the surface and misses a small area beside it.

2.1.3 LATERAL FORCE

2.1.3.1 FRICTION LOOPS

Static and dynamic friction between the tip and the surface are measured via friction loops which can be observed during a scanning process on an oscilloscope or on the computer screen via appropriate hardware/software such as MacLab/4s ADInstruments (instrument and its software Scope version 3.6.69 alias). The friction loop (Figure 2.1-7 (A)) is a plot of the amount of lateral twisting in the cantilever against the distance that the contacting sample is moved. The total height is equal to the sum of the lateral force of the forward and reverse direction. The magnitude of the lateral force corresponds to the amount of twisting on the tip with the reflected positions of the laser detected by the PSPD.

Starting at position 1 and moving to position 2 on the friction loop in Figure 2.1-7 (A), the tip-surface interaction forces the tip to remain fixed to the surface and subsequent twisting of the cantilever (static friction regime). Therefore, the sharp end of the tip remains at the same position while the cantilever twists causing the laser to be reflected to the right of the detector. The distance that the tip has deflected is called the tip displacement, Δx_{Tip} (Figure 2.1-7 (C)).

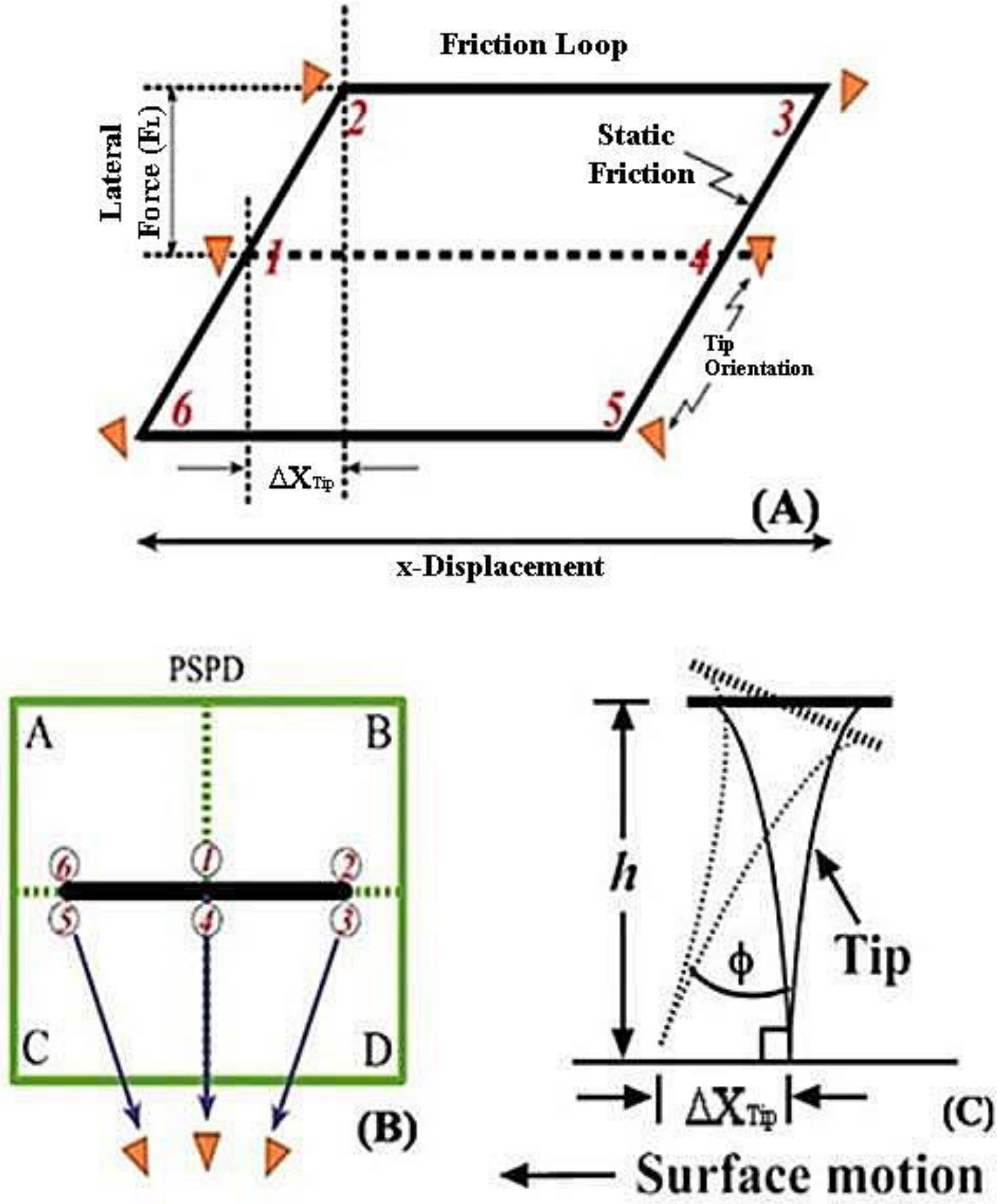

Figure 2.1-8. Schematic diagram of a friction loop (A) and the corresponding positions of points 1-6 on the PSPD. A – D represent the four PSPD quadrants. (B) The orange triangles on both (A) and (B) show the tip orientation (see section 1.2.3.3) at the relative positions. (C) Surface motion and its lateral force will cause a tip displacement of Δx_{tip} which corresponds to an angle of ϕ for a tip with height *h*.

Once the lateral force applied has overcome the static force the tip begins to undergo dynamic friction (points 2 to 3) without further twisting. The displacement in the x direction comes to a stop between points 3 and 4 and from here, the sequence is reversed. Lateral force (F_L) calculations require the tip displacement (Δx_{tip}) which is found as an angle (ϕ) first before being converted into a distance using simple geometry.

Therefore knowing the twisting spring constant K_T (Equation 2.1-9), the lateral force can be obtained:

$$F_L = k_T \Delta x_{Tip}$$

Equation 2.1-3

2.1.4 FORCE DISTANCE RELATION BETWEEN TIP AND SAMPLE

Forces along the z direction (Figure 2.1-3) such as electrostatic, van der Waals and capillary (Section 2.1.6) mechanical responses (just to name a few) can be detected in a force versus distance mode using tip-sample separation curve. The force effects are typically detected before the tip apex and sample contact. Figure 2.1-8 illustrates the general force and distance relationship observed by AFM translation of the tip and/or sample along the z direction and shows a representation of an approach (red) and retract (blue) force versus distance (F-D) curve taken on an incompressible surface in an ambient air environment (Watson, 2005).

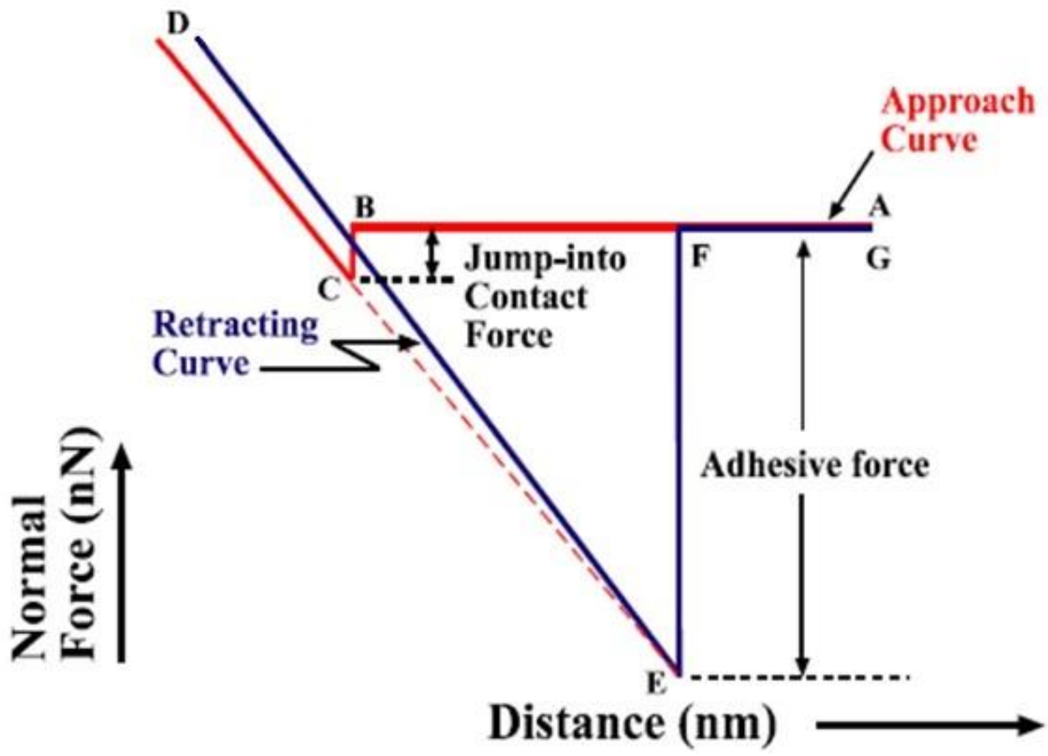

Figure 2.1-9. Representative Force distance curve of a tip contacting a hard surface experiencing both attraction and repulsion.

The horizontal scale is the amount of distance that the stage is moved by the scanner in the z-direction. The vertical axis is the cantilever force measured along the z-direction by way of tip interactions with surface using Hooke's law. Section A-B along the approach (red) curve represents the Figure 2.1-8 cantilever still not in contact and approaching the surface with no or negligible forces acting on it (Figure 2.1-9 (A)).

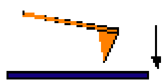

Figure 2.1-10. (A) Shape of the cantilever corresponding to section A-B.

Section B-C (Figure 2.1-8) shows the attractive force exceeding the spring constant of the lever causing the lever to snap into contact on the surface (Figure 2.1-9 (B)). This snap-on feature is common on F-D curves taken in air due to the large meniscus attraction between the tip and the surface (which can be reduced or eliminated when working in liquid or under vacuum (Section 2.1.6).

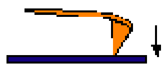

Figure 2.1-10. (B) Cantilever jumping into contact with the surface corresponding to section B-C.

Section C-D (Figure 2.1-8) represents an additional force being applied from the tip down onto the surface bending the cantilever (Figure 2.1-9 (C)). This loading force can be pre-determined depending on the desired interaction force, or eliminated in order to determine adhesive forces made at contact.

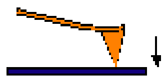

Figure 2.1-10. (C) Shape of the cantilever corresponding to section C-D where an additional loading force is applied.

Section D-E (Figure 2.1-8) represents the cantilever beginning to retract with the tip apex remaining in contact with the surface and insufficient cantilever bending to overcome surface attractive forces (Figure 2.1-9 (D)).

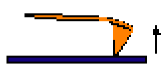

Figure 2.1-10. (D) Shape of the cantilever as it starts to retract from the surface.

Section E-F (Figure 2.1-8) represents the retraction force where the spring constant is sufficient to overcome the adhesive force (e.g., capillary force) (Figure 2.1-9 (E)).

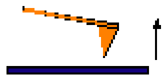

Figure 2.1-10. (E) The tip has detached from the surface.

Section F-G (Figure 2.1-8) is when the tip is far from the surface and experiences no forces (Figure 2.1-9 (F)).

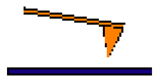

Figure 2.1-10. (F) The cantilever retains its original figure.

The hysteresis between sections C-D and D-E (Figure 2.1-8) is due to friction and the shape and angle of the tip. For example, when the loading force is applied along the cantilever and the tip is in contact with the sample, the tip may move slightly forward along the y direction and then results in the hysteresis which is a consequence of the detector system responding to both bending and buckling of the lever.

2.1.5 FORCE DISTANCE CURVE AND INDENTATION

The loading force (F_N) of the tip to the surface can be obtained through knowing the cantilever spring constant (k_N) and deflection and the adhesion force between the tip and the sample. The deflection and adhesion (section E-F in Figure 2.1-8) are represented as the intensity on the PSPD which can be converted into F_N using k_N and the gradient of the red approach curve (C) between points C and D (Figure 2.1-8).

$$F_N = k_N \frac{[adhesion\ force\ +\ (final\ detector\ value\ -\ initial\ detector\ value)]}{C}$$

Equation 2.1-4

2.1.5.1 INDENTATION AND FORCE DISTANCE CURVE ON A SOFT SURFACE

On soft surfaces such as some polymeric materials (e.g., PDMS, a silicon based polymer (Section 3.5), significant amounts of tip indentation into the sample occurs. Lines C-D and D-E (Figure 2.1-8) on the force distance curve are no longer straight but curved downwards (Figure 2.1-10).

When the F-D curve for a soft surface is calibrated against an F-D curve for a hard surface. The amount of indentation (σ) (Figure 2.1-10) can be measured by calibrating the points of contact (green X) between the tip and the surface of both graphs to the same distance (preferably both at zero). Indentation of the tip and the hard surface chosen (Silicon wafer in most cases) is small enough to be neglected.

Sneddon's formula for the force applied to a cone tip surface is given by (Sneddon, 1965):

$$F_{cone}(\sigma) = \frac{2E^*\sigma^2}{\pi \tan\alpha}$$

Equation 2.1-16

Where F_{cone} is the F_N from a cone shaped tip, α is the half angle of the tip (given by manufacturer typically ~15°) and E* is the relative Young's Modulus which is given by(Sneddon, 1965):

$$\frac{1}{E^*} = \frac{1-\mu_{tip}{}^2}{E_{tip}} + \frac{1-\mu_{sample}{}^2}{E_{sample}} \approx \frac{1-\mu^2}{E_{sample}}$$

Equation 2.1-15

where ($E_{tip} >> E_{sample}$)

Forcing a tip into an elastic surface can cause compression of the material underneath the tip. The contact area between the tip and the compressible surface increases with indentation. Sneddon's formula makes one assumption and that is the indented sample adopts the shape of the tip, in this case a cone with an angle 2α (there are other formulas for other tip shapes (Watson, 2001)). It also assumes that the surface is perfectly flat and does not take into account surface energies.

Another obvious difference between the curves for a hard surface and for an elastic surface is the size of the adhesion force. When the tip is being pulled away from the surface, the adhesion force may cause the surface to be pulled away with the tip. Hence there seems to be a larger adhesion force.

2.1.6 CAPILLARY FORCE

Due to condensation, water capillary bridges can form on contacting surfaces between an AFM tip and a sample. The small space between the tip and the sample surfaces is an area of high adsorption capability because of the overlapping adsorption potentials (Nevshupa et al., 2002, Wei and Zhao, 2007). Capillary force between the AFM tip and the sample surface, which can be as small as 4 nm in radius (Sedin and Rowlen, 2000), is partly responsible for the adhesion between the two surfaces.

The capillary bridge volume grows with the increase of relative humidity (RH) and contact time between the AFM tip and the sample, thus causing the capillary force to vary. The capillary force does not necessary increase with increasing capillary volume but rather the force increases with the meniscus area and the pressure difference. However the pressure difference will decrease as a result of the capillary volume expansion.

The van der Waal forces (F_{vdW}) are the dominant adhesion force in cases when the capillary bridge does not exist. At very low RH, prior to the capillary formation, F_{vdW} can be more than 5 times greater than capillary force (Xiao and Qian, 2000). At certain RH values the adhesion on hydrophobic samples may be humidity-independent as there is maybe no meniscus formation between an AFM tip and the hydrophobic sample (Xiao and Qian, 2000). Humidity also has a negligible effect on the cantilever spring constant (Thundat et al., 1994)

Capillary adhesion can be eliminated by conducting measurements in a liquid environment (Ducker et al., 1991, Frisbie et al., 1994, McKendry et al., 1998, Williams et al., 1996). However the solvent will affect the adhesive force (F_{STW}) through solvation and solvent exclusion (Sinniah et al., 1996).

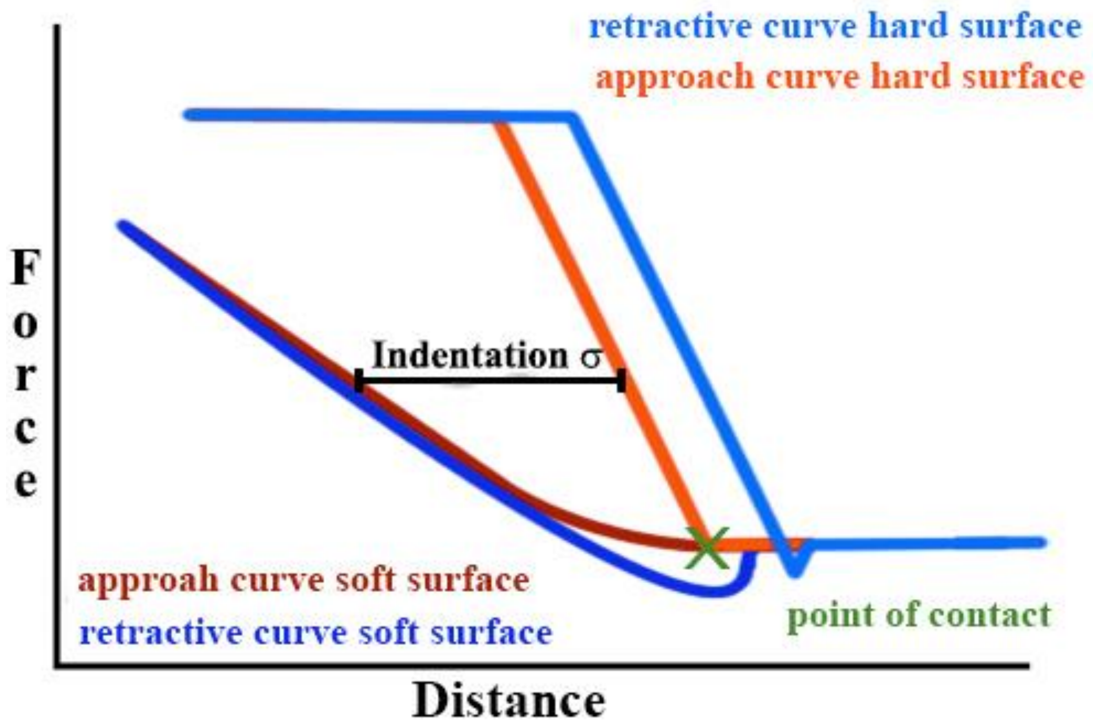

Figure 2.1-11. F-D curve on a soft PDMS surface (red) calibrated against an F-D curve on a hard surface (orange) to show the amount of indentation at a particular force.

2.2 WETTABILITY

2.2.1 HYDROPHILICITY, HYDROPHOBICITY AND SELF-CLEANING

Hydrophilicity and hydrophobicity in simple terms means water loving and fearing, respectively. These two terms are usually used to describe the characteristics of solid surfaces. Water molecules have a dipole moment of 1.85 Debye and forms hydrogen bonds with other water molecules. The high cohesion between water molecules gives water a strong surface tension, a force that acts to reduce the surface area of free liquid as molecules at the liquid surface are in an energetically unfavourable state.

The terms hydrophilicity and hydrophobicity are sometimes also applied to the contact of a solid surface with other liquids. For a small drop of liquid ($\leq$ 100 μL where gravitational effect can be neglected) the contact angle (CA) is the angle at which a liquid/vapour interface meets the solid surface. A drop of water that shows a CA greater than 90° on a surface means that its cohesion is stronger than adhesion and hence the surface is hydrophobic. The opposite is true for a hydrophilic surface where the CA is less than 90°. Hence the CA can represent the 'wettability' of a liquid on a solid surface.

Young's equation relates the CA to surface energies of the liquid and solid surfaces (γ_{SL}). The interfacial tension between solid and vapour (γ_{SV}) and liquid and vapour (γ_{LV}) are also involved as described in:

$$\cos(\theta_0) = \frac{(\gamma_{SV} - \gamma_{SL})}{\gamma_{LV}}$$

Equation 2.2-1

Where θ_0 is the static CA formed with a smooth surface.

Hydrophobic surfaces are desirable in liquid flow applications whereas the hydrophilicity of surfaces should be enhanced in adhesive surfaces. Both surface properties can be enhanced by introducing surface roughness (Section 2.2.3 for further details). Superhydrophilic (CA <~30°) and superhydrophobic (CA >~150°) surfaces could both be considered self-cleaning surfaces.

Superhydrophilic surfaces enhance the ability of water droplets to spread over large areas. Droplets will combine to cover the whole surface and eventually run off the edge dragging the rest of its volume with it through cohesion. Superhydrophilic surfaces are usually created by altering surface chemistry and can be structurally enhanced (Section 2.2.3.1). Titanium dioxide films, which are commonly found on antifogging glass sheets and mirrors, contain a layer of OH groups on the surface (after UV irradiation) making the surface tension almost the same as water and a CA of virtually 0°.

Unlike superhydrophilic surfaces, water rolls off superhydrophobic surfaces when there is only a small inclination or movement. Natural self-cleaning surfaces can be found on wings of insects (Chapter 4) which rely heavily on clean wings for survival and leaves of plants which live in muddy or dusty habitats.

Micro/nanoscale roughness plays an important role in superhydrophobicity (Section 2.2.3.2). Surface structures that hold up a droplet on their peaks are small so that they are not become a significant physical barrier to the droplets' movement across the surface. The area of the surface interacting with the droplet is reduced and thus results in a smaller apparent value of γ_{SL} than it otherwise would have been on the same surface without the roughness. Roughness is essential in all superhydrophobic surfaces.

2.2.2 CONTACT ANGLE AND CONTACT ANGLE HYSTERESIS

Young's Equation (Equation 2.2-1) is a theoretical approach to finding CAs for ideal liquid and solid surfaces. Due to derivations of surfaces from ideal conditions (defects and inhomogeneous roughness and chemistry) there exists a spectrum of CAs ranging from the receding angle up to the advancing angle.

For a drop of liquid on a surface, the advancing angle (θ_a) is the maximum CA obtainable by tilting the surface or by increasing the droplet volume. Likewise, the receding angle (θ_r) is the minimum CA obtainable by tilting the surface or by decreasing the droplet volume (Figure 2.2.1). The difference between the two angles is called the contact angle hysteresis (CAH), which exists because the imperfections on a surface resist the movement of the contact line, and is defined as:

$$CAH = \theta_a - \theta_r$$

Equation 2.2-2

The force required to move a droplet along the surface plane is approximated by (Gao and McCarthy, 2006b):

$$Force \sim \gamma_{LV}(\cos\theta_r - \cos\theta_a)$$

Equation 2.2-3

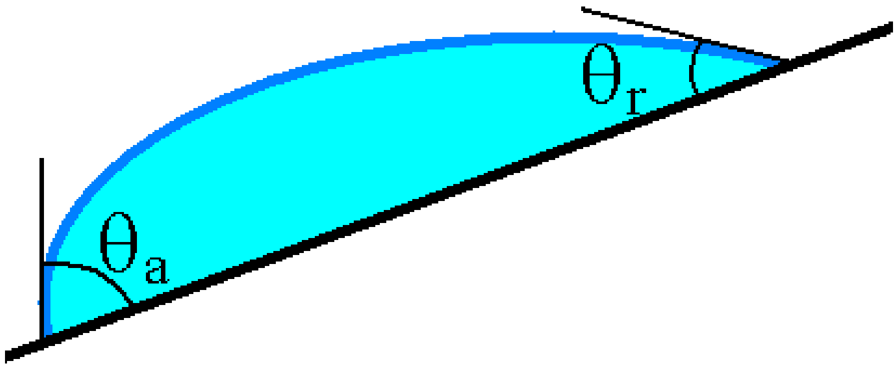

Figure 2.2-1. The advancing (θ_a) and receding (θ_r) angles of a droplet on a tilted surface.

Contact angle hysteresis indicates a resistance to the motion of the droplet which may be contributed to by the nanoscale roughness or sharp edges (Section 2.2.3.3). When droplets roll, it is very likely that they move similar to tank tread at the front while sliding at the backend (Gao and McCarthy, 2006a). Unless CAH = 0, droplet shape changes when droplets move (from ground state shape and back and forth to transition state shape). Both the CA and CAH indicate how much surface energy there is between the surface of the liquid drop and the solid plane and hence the adhesion, or the mobility, of the droplet on the solid surface.

2.2.3 WENZEL AND CASSIE-BAXTER MODELS

2.2.3.1 WENZEL MODEL

While Young's equation was useful to find the CA of a liquid on an ideal smooth surface, in 1936 Wenzel (Wenzel, 1936) modified the equation under the condition of taking into account the effect of uniform surface roughness (Figure 2.2.2). He stated that the solid area under the liquid has a different superficial energy compared to a dry surface. The superficial energy of the wetted area is lowered if the surface is hydrophilic. For an increase in the geometric surface of the wetted area, the actual surface wetted is larger if the surface is rough. Consequently, there is a greater decrease of net energy. Same reasoning applies for a hydrophobic surface where the (completely wetted) area under the droplet has a higher superficial energy. More surface area involved for a roughened surface results in a greater increase of net energy. Hence Wenzel modified the Young's equation by multiplying a roughness factor *r* given by:

$$r = \frac{actual\_surface}{geometric\_surface} = \frac{\cos\theta_{rough\_surface}}{\cos\theta_{smooth\_surface}} = \frac{\cos\theta_W}{\cos\theta_0}$$

Equation 2.2-4

where θ_W is the CA of a droplet in the Wenzel regime. This implies that $\cos\theta_0$ increases by the same factor as roughness increases the surface area (for a smooth surface, r = 1). This equation can not be applied for a large r where complete wetting can not be achieved (but be a composite regime, Section 2.2.3.2) or roughness asperity dimension becomes large enough to physically affect the droplet.

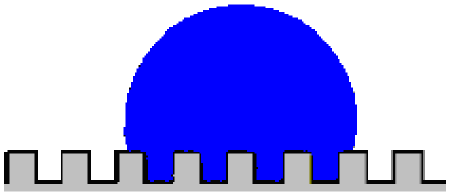

Figure 2.2-2. Droplet in the Wenzel regime.

2.2.3.2 CASSIE-BAXTER (C-B) MODEL

In another experiment, Lee (Lee, 1938) attempted to wet rough surfaces of limestone underwater with road tar. Immersed in water, the rough surfaces could not be wetted with road tar, while highly polished limestone surfaces were wetted easily. The explanation for this was because water had already occupied the minute crevices of the rough surface. Too much energy was required to replace the limestone-water interface by a limestone-tar interface.

While the Wenzel regime amplifies the surface wettability, the solid-liquid contact area is reduced in the Cassie-Baxter (C-B) regime. In hydrophobic porous surfaces, the protrusions can sometimes trap air and only allow the surface to be partially wetted (Figure 2.2-3). This means the droplet on the surface has two CAs. The apparent angle in the C-B regime (θ_C) therefore is expressed as the sum of the contributions from the two CAs; θ_0 (the CA on f_1) and θ_{air} (the CA on f_{air}):

$$\cos\theta_c = f_1\cos\theta_0 + f_{air}\cos\theta_{air}$$

Equation 2.2-5

where f_1 is the surface area fraction of the solid substrate touching the droplet and f_{air} is the remainder of the surface area fraction underneath the droplet (not in contact with the solid substrate) and $f_1 + f_{air} = 1$. As $\theta_{air} = 180^{\circ}$ due to having no contact with the solid surface:

$$\cos\theta_c = f_1\cos\theta_0 - f_{air}$$

Equation 2.2-6

In the case where the solid in contact with the droplet also has a significant secondary roughness and contacts the water in a Wenzel regime, the equation is modified to become:

$$\cos\theta_C = rf_1 \cos\theta_0 + f_1 - 1$$

Equation 2.2-7

where *r* is the roughness factor defined by the solid-liquid area to its projection on a flat plane (the roughness factor of the wetted area).

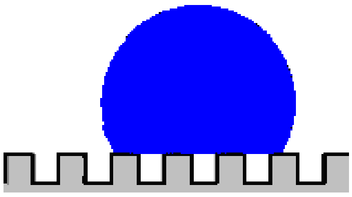

Figure 2.2-3. Droplet in the Cassie-Baxter regime.

Retaining a large solid-air fraction on surfaces is essential for self-cleaning surfaces. These composite surfaces are not completely wetted by water droplets as air remains amongst the structures underneath the droplet. Droplets in the C-B regime show high contact angles and low contact angle hysteresis and are easily mobile. The highest CA with lowest CAH are achieved with hexagonally packed cylindrical pillars with rounded tops (Nosonovsky and Bhushan, 2005). Surfaces with hierarchical structuring however, where the roughness features are also covered with secondary features, promote higher self-cleaning efficiencies.

Composite regime usually only occurs with surfaces with a hydrophobic chemistry, otherwise it would be more favourable for the liquid interface to drop down to the bottom of the asperities. However Herminghaus (Herminghaus, 2000) believed that indentation on hydrophilic surfaces can support droplets in the composite regime as long as there are overhangs on the side of the indentations (Section 2.2.3.3). Quéré (Quéré, 2004) and

Lafuma and Quéré (Lafuma and Quéré, 2003) have also observed composite regimes on hydrophilic materials.

2.2.3.3 STABILITY IN THE C-B REGIME

On surfaces where both wetting regimes can be achieved, transition between C-B and Wenzel states can occur via experiencing external forces. When smoothly deposited on rough surfaces, droplets could temporarily reside in a metastable composite state even though the wetted regime is the configuration with the absolute minimum energy. To transit down to the Wenzel state the drop needs to overcome an energy barrier to fill in between the surface asperities. A large energy barrier indicates a more stable C-B drop.

The C-B state is favoured if $\cos\theta_0$ is smaller than $\cos\theta_W$, Equation 2.2-8 is derived by equating the C-B (Equation 2.2-6) and Wenzel (Equation 2.2-4) equations,

$$\cos\theta_0 = \frac{1-f_1}{f_1 - r}$$

Equation 2.2-8

This situation is sometimes found on rough structures with a pitch spacing of less than 5μm.

The contact angle of a droplet on a sharp edge can vary between the values corresponding to the contact with the horizontal and inclined surface. This gives rise to contact angle hysteresis which increases with the sharpness of the edge. Some nanostructures on hierarchical surfaces may pin the contact line to resist the advancement of the droplet towards the bottom of the surface and hence stabilizes the droplet in the C-B regime. However, it may also be unfavourable as it acts as sharp structures that may contribute to the contact angle hysteresis of the surface and hence reduces droplet mobility and the effectiveness of self-cleaning. This trade-off between droplet mobility and stability (Bush et al., 2007) (Chapter 7) can be reduced using a hierarchical scale of surface structures.

Another way to reduce the likelihood of droplets sinking to the bottom of the surface asperities without pinning the contact line is to have structures with convex sidewalls. The droplet's energy will reach a stable equilibrium when the meniscus (at the bottom of the droplet) is in line with the thickest part of the structures. Advancing past this equilibrium point requires a decrease in contact angle (in order to maintain a constant meniscus radius or curvature) which will require external energy input. The droplet contact line is also less likely to advance towards the substrate base as the liquid-air interface at the bottom of the droplet would have to expand against the droplet surface tension (Liu and Lange, 2006).

In nature, microstructures with convex sides are found on plant surfaces such as *Liriodendron chinense* (Wagner et al., 2003) (which also has nanostructure due to wax coverings) and insect cuticles such as the *Gudanga* sp. cicada wing (Chapter 4).

2.2.3.4 APPLICABILITY OF WENZEL AND CASSIE-BAXTER MODELS

Apart from the requirement that the effects of gravity and line tension contributions need to be negligible, many reports have discussed other applications of the Wenzel and C-B equations, for example (Anantharaju et al., 2007, Gao and McCarthy, 2007b, Gao and McCarthy, 2007a, McHale, 2007, Nosonovsky, 2007b, Panchagnula and Vedantam, 2007, Extrand, 2003). Both Equations 2.2-4 and 2.2-5 are related to the Young's Equation (Equation 2.2-1) which is related to the surface energies of the three phases. Thus the surfaces that are applicable require:

- Consistent roughness throughout the surface (Extrand, 2003, Gao and McCarthy, 2007b, Gao and McCarthy, 2007a, McHale, 2007, Nosonovsky, 2007b, Panchagnula and Vedantam, 2007, Anantharaju et al., 2007) and the surfaces apart from the main substrate roughness are considered atomically flat (Barbieri et al., 2007)
- Roughness dimensions to be small compared to the drop sizes (Anantharaju et al., 2007, Nosonovsky, 2007b) or the capillary length (273 µm for water). Normally 2~3 magnitudes smaller (Brandon et al., 2003) and where the volume of liquid within the asperities can be neglected (Barbieri et al., 2007)
- Roughness has a positive sign of curvature (i.e. roughness that are protrusions and not indentations) (Anantharaju et al., 2007, Nosonovsky, 2007a, Nosonovsky and

Bhushan, 2007, Sun et al., 2005) and the side of the roughness features are not concaving (for Cassie-Baxter regime).

For surfaces that do not satisfy the requirements above, the Wenzel and C-B equations need to be re-interpreted to take local values under the droplet perimeter (Gao and McCarthy, 2007b, Gao and McCarthy, 2007a, McHale, 2007, Nosonovsky, 2007b, Panchagnula and Vedantam, 2007).

2.3 FUNCTIONAL STRUCTURED SURFACES

Functions of a surface can be created or improved by tailoring its morphology. Since Wenzel's publication on the wettability of textile fabrics and the resistance of solid surfaces to wetting by water (Wenzel, 1936), altering surface energies with surface roughness has been widely researched. Roughness induced low energy surfaces have been widely applied in micro and nano-electro-mechanical systems. As devices become smaller, their components start to encounter more problems associated with surface effects such as surface adhesion and friction leading to device malfunction and difficulty in production (Tas et al., 1996).

Together with the manipulation of surface chemistry, advances in surface lithography allow for manipulation of surface geometry on the sub-microscale and most likely beyond the nanoscale in the future. Amongst the several structure patterning techniques are photolithography (Stratakis et al.), templated electrochemical deposition (Bartlett et al., 2002), plasma treatments (Woodward et al., 2003), electron-beam lithography (Martines et al., 2005), selective growth of carbon nanotubes(Lau et al., 2003) and Atomic Force Microscopy (Watson et al., 2006b). Surfaces with remarkable capabilities are the end result and they include (Stratakis et al.) mechanical, self-cleaning, optical, adhesive, actuation, sensing, and responsive capabilities (Woodward et al., 2003). Tailoring functions to the surface of ordinary materials diversifies their potential applications in areas including biosensors, corrosion protection, semiconductor processing, biofouling, tissue engineering and biomaterials technology (Watson et al., 2006b).

2.3.1 FUNCTIONAL STRUCTURED SURFACES ON INSECTS

Insects have employed micro/nanostructures on their cuticles, especially their wings, for millennia, which serve extraordinary functions. Developed through evolution the surface asperities reduce the insect cuticle adhesiveness beyond many man-made flat surfaces and greatly enhance the insect's survival in harsh environments. It also helps them to escape from accidental contact with water or sticky surfaces (e.g., spider webs). As well as reducing surface adhesion, the surface structures, depending on their dimensions and shapes, can also aid in other functions. These include camouflage (colour patterns or anti-reflection) (Gorb et al., 2000, Tada et al., 1998, Vincent, 2009), thermal regulation (Gorb et al., 2000), communication (Tada et al., 1998, Gorb et al., 2000) and friction/wear reduction (Vincent, 2009). Surfaces with low adhesion to water droplets resulting in a self-cleaning function are common amongst many of these insect cuticles. Apart from reducing surface energies other 'technologies' from insect cuticles could potentially be incorporated onto/into a range of products including textiles for a multitude of purposes (Eadie and Ghosh, 2011, Gao and McCarthy, 2006b, Sun et al., 2006, Vincent, 2008, Vincent, 2009).

It may be possible in the near future to combine various insect cuticle structuring and create a single surface with multiple desired functions. Specific functions could also be enhanced by altering the surface structure shapes and dimensions. In this section a brief description is presented of a few of the attributes found on insect species that could extend the potential applications of man-made surfaces/devices.

2.3.2 LOW ADHESION AND SELF-CLEANIG SURFACES

To maintain sufficient mobility and high functional efficiency of their wings, many insects (particular those with a high ratio of wing surface area-to-body mass (SM)) have the ability to reduce/remove surface contamination. Altering chemistry to further reduce surface adhesion may have reached an evolutionary stage where it is more difficult than employing micro/nano scale surface roughness which reduces the contact adhesion between component surfaces.

The micro/nano-scale asperities on insect cuticles lower the surface adhesiveness by reducing contact area with foreign contacting surfaces. Solid and liquid particles will roll or fall off the low adhesive surface at slight inclinations. Water drops are restricted from entering the small spacings between the surface structures (Figure 2.2-3) and results in a higher apparent contact angle θ_c. A good approximation for this wetting behaviour is given by the C-B expression (Equation 2.2-5) where droplets in the C-B regime show a high contact angle and low CAH indicating that it has low attraction to the surface as required on self-cleaning surfaces.

The surface roughness of the wing may allow insects to shed water off their wings quickly reducing the flying weight of the insect. Moreover droplets will also pick up contaminant particles along the way hence produce a self-cleaning effect.

Thus adoption of similar chemistry and topography to micro/nano scale cuticle structuring may lead to low energy surfaces with self-cleaning properties. The micro/nano-structures are not limited to sophisticated technological devices. Applying self-cleaning structures on everyday surfaces like windows, cars and bathroom tiles may help reduce maintenance and extend material lifetimes (Barthlott and Neinhuis, 1997, Vincent, 2009).

2.3.2.1 ANTIBACTERIAL SURFACES

Recently it has been shown that structuring found on wings can be anti-bacterial and result in bacterial death within only a few minutes of contact. For example two recent studies have shown that the cicada *Psaltoda claripennis* and dragonfly *Diplacodes bipunctata* structuring can kill gram-negative bacteria (Hasan et al., 2013, Ivanova et al., 2013, Pogodin et al., 2013, Ivanova et al., 2012b). In the case of the dragonfly gram-positive bacteria are also killed (Ivanova et al., 2013). A recent study by Ivanova *et al.*(Ivanova et al., 2012b) on the bactericidal effect on the wings show the cellular components of *Pseudomonas aeruginosa* spreading down in-between the nanopillars after as little as three minutes upon contact. When an AFM cantilever tip was brought into contact with a bacterial cell without applying a loading force, the rupture of the cell movement of the cell could be monitored and cell rupture indicated by a sudden short displacement (~200 nm as monitored by piezo movement of the AFM) into the contacting wing surface. The effect remained after coating the wing surface with 10 nm of gold suggesting that the original surface chemistry is not required for the bactericidal effect.

The common approach in fabricating antimicrobial surfaces to combat infectious diseases is to functionalize or coat the surface with substances lethal to the target organisms (Hsu and Klibanov, 2010, Ivanova et al., 2011, Murata et al., 2007, Schaer et al., 2012). This alternative antibacterial method does not contribute to the antibiotic resistance emerging amongst pathogenic bacteria which is a concern in conventional antibiotic treatments (Ivanova et al., 2012b).

2.3.3 WATERPROOFING HAIRS

Setae (hairs) on many insect cuticles (lacewing (Watson et al., 2010b), termite (Watson et al., 2010a) and water strider (Watson et al., 2010)) have been shown to prevent wetting to the underlying membrane cuticle by holding drops on their tips (Figure 2.3-1). Dense hairs found on the legs of water striders can withstand high hydrodynamic pressure experienced during leg strokes while traversing across the water surface (Bush et al., 2007). Water drops with kinetic energy falling onto the wing surface of the lacewing can be repelled away with the aid of the hairs which act as a layer of microsprings and resist penetration and dispersal of drops. The drops can partially wet the membrane surface below and collect contaminants in the wetted region. These types of setae have potential applications as liquid-stain-proofing for textiles such as clothes and carpets.

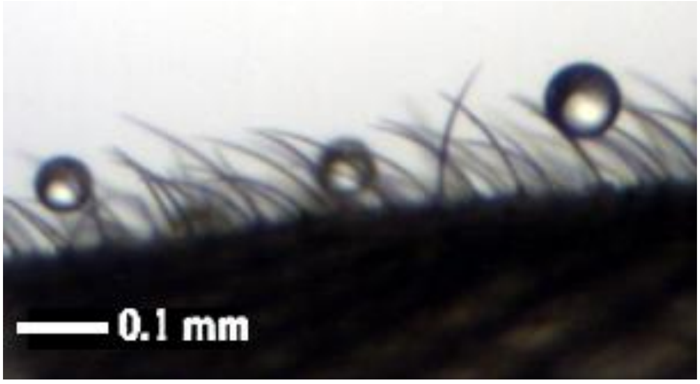

Figure 2.3-1. Optical microscope image of microdroplets of water from a mist sprayer supported by hairs on the lacewing Nymphes myrmeleonides**.**

2.3.4 INSECT OPTICAL PROPERTIES

Ordered hexagonally packed structures with a spacing and height of ca. 200 nm are found on the surfaces of moth eyes (Watson and Watson, 2004) and the transparent wing membranes of a number of cicada species (e.g., *Tamasa tristigma, Macrotristria angularis*, *Thopha saccata Psaltoda claripennis*, and *Cicadetta oldfieldi*) (Sun et al., 2009, Watson et al., 2008c, Watson and Watson, 2004, Watson et al., 2008a) (Figure 2.3-2). The surface can be thought of as a homogeneous surface with a smooth transitional increase in refractive index to improve transmittance and lower reflectance (Watson and Watson, 2004) of light and improving camouflage. Manipulative scanning with the AFM at a high loading force scrapes off the structure apex and deteriorates the optical properties depending on the amount removed (Watson et al., 2008c). These anti-reflective surfaces can be easily replicated on polymers such as PDMS (Watson et al., 2008c) and may find applications for other transparent surfaces where low contamination and high light transmission is desired such as display monitors and shop windows. A 10% increase in energy capturing of solar panels with these nanostructured materials has been reported (Parker and Townley, 2007, Vincent, 2009).

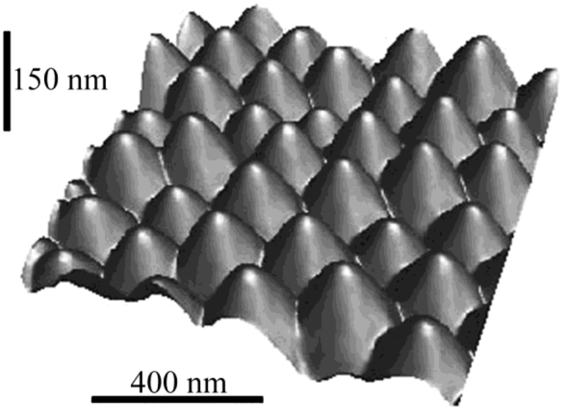

Figure 2.3-2. Atomic Force Microscope generated 3-D image of a cicada wing array.

Many butterflies and moths (Lepidoptera) possess a structuring on their wings comprised of many scales organized in a tile-like arrangement. The colour of the butterfly is enhanced due to the arrangement of the surface asperities of the scale (Vukusic et al., 2004, Vukusic and Sambles, 2003). Depending on the scale size, curvature and arrangements, these insect wings can display a range of optical functions such as iridescence and/or selective wavelength absorption/reflection which serves the purpose of camouflage, signalling, and thermoregulation (Tada et al., 1998).

Scale alignments that absorb light can be mimicked to produce a solar thermal collecting surface to be applied on winter clothes and outdoor surfaces where heat absorption and self-cleaning functions are desired. The iridescence of the butterfly may also function as a distracting camouflage to avoid predation while in flight (Tada et al., 1998). The technology could be also utilised to discourage animals such as on crop fields or airports.

Reflecting a specific range of wavelength of light using their wings as a form of communication is common amongst butterflies (Tada et al., 1998) and dragonflies (Gorb et al., 2000). This technology has potential for ultra-violet reflective glass to prevent harmful UV passing through windows of cars and buildings. Physical colouration of textiles using surface structures to scatter, diffract or create interference has been reported (Vincent, 2009, Vukusic and Sambles, 2003) and commercially produced (Eadie and Ghosh, 2011).

2.3.5 WEIGHT AND MATERIAL MINIMISATION

Some insects present surface asperities designed to minimise weight and material usage (Hu et al., 2011a, Watson et al., 2010a, Watson et al., 2010b). Insect surfaces like butterfly and moth wings show hierarchical structuring where the surfaces of the primary structure (scales) are also covered with asperities (holes and crisscrossing ridges). As well as further reducing the solid-liquid contact area, weight and material of the energetically expensive chitin (the basic material make-up of many insect cuticles) (Watson and Watson, 2004) are reduced.

In the case of some termite species *(*e.g.*, Microcerotermes sp*) the wings present microstructuring in the form of small clusters (called micrasters) (Figure 2.3-3). These structures serve as an anti-wetting protection layer and have an open form of structuring to minimise weight and material. If this form of structuring was not of an open arrangement but of a solid architecture then the wings would become five times heavier (Watson et al., 2010a) and excess weight may inhibit the ability to fly.

Figure 2.3-3. SEM images of termite wing membrane surface showing star-shaped micrasters and a hair.

Various grooves (Figure 2.3-4) on setae of many insects may possibly enhance the stiffness and promote direct wetting (Hu et al., 2011a, Andersen and Cheng, 2005). Hydrophobicity is greatly reduced when the surface grooves are eliminated (Hu et al., 2011a, Watson et al., 2010 , Watson et al., 2010a, Watson et al., 2010b, Ivanova et al., 2012a). In the case of various termite species (e.g., *Nasutitermes* sp.), the grooves on the hairs may reduce the weight of each hair by as much as 10%.

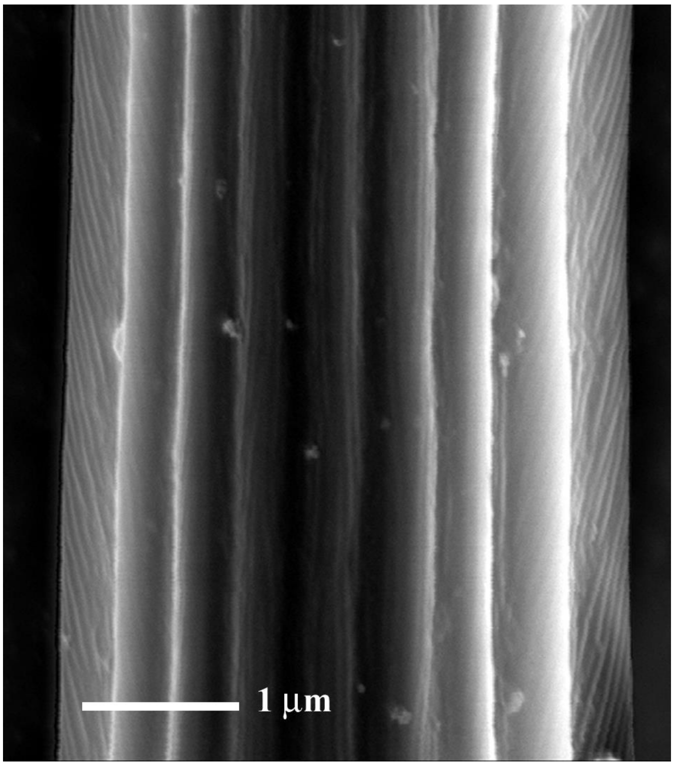

Figure 2.3-4. SEM image of the hair of lacewing showing surface grooves and ultra-fine channels at about 45° that meet at the top and bottom of the larger grooves.

Protrusions on some cicada wings due to their shape (e.g., *Gudanga* sp. (Chapter 4) have a small region of attachment at the base (Figure 2.3-5) allowing a larger air pocket and giving additional air pressure that may help to repel falling drops off the surface. The narrower base reduces the volume of each protrusion by more than 30% (Watson et al., 2011c).

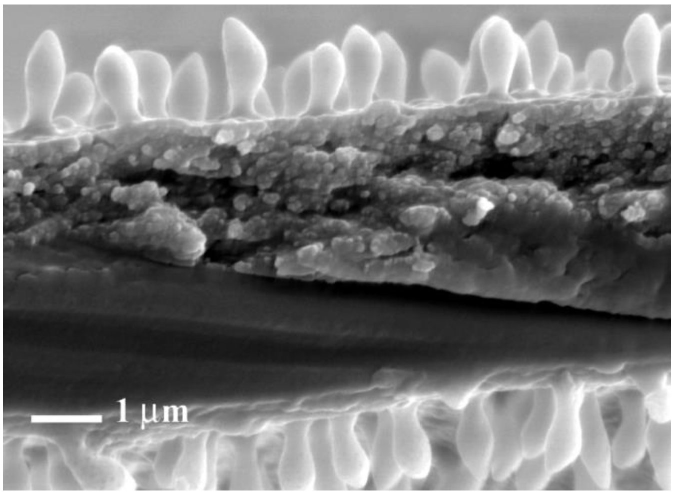

Figure 2.3-5. SEM image of the side view of the cicada wing of *Gudanga sp.* showing the thinner base of the surface structures.

2.3.6 INTRODUCING MULTIFUNCTIONALITY ONTO ONE SURFACE

Many of the 'free technologies' found on insect cuticles have intriguing functions. Functional-efficiencies of man-made surfaces are improving as surface replication, manipulation, and lithographic techniques improve. At the present time the main application of surface roughness is to reduce surface adhesion and friction. In the near future, these man-made surfaces could possibly start to be implemented with a variety and mixture of multi-functional surface structures to further improve man-made technologies/devices.

It may be possible to create surfaces with multiple micro and nano shapes as an alternative path to accommodate more functions onto one surface. Some insects incorporate varied chemistry and/or cuticle architecture for this purpose. For example desert beetles have alternating hydrophobic and hydrophilic regions on their elytron (hard protective forewing) which they use to collect drinking water from the early morning fog (Parker and Lawrence, 2001). Wing setae on many insect wings which may contribute to aerodynamic factors (Perez-Goodwyn, 2009) also have superhydrophobic structures to further reduce wetting at different length scales (Watson et al., 2010a).

The idea of combining various bulk material properties (thermal, optical, mechanical) into a hybrid material is not uncommon (Vincent, 2008, Ashby and Brechet, 2003, Eadie and Ghosh, 2011, Vincent, 2009). By understanding the relationship between the shape of surface structures and their functional mechanisms, it may become a future trend in man-made technologies to introduce new and multiple functions onto a surface. This can be achieved by adding new layers of structuring amongst pre-existing architectures. For instance combining the water collecting technology of the desert beetle with anisotropic wetting arrangements (e.g., scales on the butterflies (Zheng et al., 2007) or micro/nanogrooves (Andersen and Cheng, 2005, Hu et al., 2011a, Zhang and Low, 2007, Chung et al., 2007)) to direct the collected moisture to the desired location may result in faster water collection and reduce water loss. Implementing flat surface roughness on the hydrophilic regions increases the area of the seeding points for water adsorption and may increase the water collecting efficiency. Adopting hierarchical arrangements on the surfaces such that one structure covers another could improve functional efficiency of the surface and may reduce the functional interferences.

2.4 CHAPTER SUMMARY

Versatilely used throughout this thesis, the Atomic Force Microscope with its unique imaging method of using a probe to interact with sample surfaces allows other surface properties such as adhesive forces, frictional forces and material spring constants to be determined as well as surface manipulation. Interaction with the sample surface is probed at the free end of a cantilever. The choice of the cantilevers' shape and surface chemistry depends on the purpose and the surface being scanned and the magnitude of the interacting forces. Deflection of the cantilever due to any changes in topography height, surface adhesion and friction is monitored by the laser and PSPD before the topographical image or surface force map/curve is produced by the software.

The wetting or contact angle of the surface corresponds to the energy of the surface which can be reduced by micro/nanoscale surface structures and can be predicted by Wenzel and Cassie-Baxter equations. Many natural surfaces contain surface structures that alter the surface properties including optical and surface adhesiveness. Self-cleaning and anti-bacterial functions are common on cuticles of insects with large super-hydrophobic wings.

3 EXPERIMENTAL BACKGROUND

3.1 ATOMIC FORCE MICROSCOPY

Three AFMs were used throughout this work, the Thermo-Microscope TMX 2000 Discoverer, Explorer and the JEOL JSPM-4200. The Discoverer and Explorer were operated using software TopoMetrix SPMLab (version 3.06.06). Both the Discoverer and the Explorer have 130 X 130 • m^2 tripod air and liquid scanners with a z-range of 9.7 • m and moves the stage/sample and the tip respectively. The whole instrument is supported on a vibration isolation air cushion table. A stepper motor drives the stage of the Discoverer in the x-y direction allowing easy movement of the sample under the tip during operation. All operations under liquid environments are conducted using the Explorer.

The JEOL JSPM-4200 is operated by the software WINSPM Application (version 4.05). The tube scanner of the JEOL located beneath the stage has a maximum scan range of 85 × 85 μm^2 and a maximum of 3 μm in the z-direction. There is another piezoelectric crystal that drives the vibration of the cantilever allowing the resonant frequency to be found. The instrument also has a vibration isolation air cushion filled with compressed air.

3.1.1 INSECT SAMPLE INVESTIGATIONS USING THE ATOMIC FORCE MICROSCOPE

Fresh insect wings were surgically separated from the insect body by scalpel. The forewings were cut into smaller sections (3 X 5 mm^2) and attached by adhesive tape, or by an epoxy resin, to AFM mounted stubs.

Investigations were carried out with a ThermoMicroscope TMX-2000 Explorer/Discoverer. Scanners were calibrated on calibration grids that are 4 X 2 μm with 1 μm spacing between them. The analyses were carried out under air-ambient conditions (temperature of 23-25°C and 65-75% RH) and thus the contributing force of attraction is from capillary forces from the surfaces (Blach et al., 2004).

‘Beam-shaped’ probes (NT-MDT Ultrasharp) were used throughout the study. Typical parameters, as reported by the manufacturer, included: Normal force constant, k_N, of 0.03 to 4.5 Nm^{-1}, integrated probe and conical tip shape with cone angle < 20^o, radius of curvature of the tip < 10 nm; and tip height of 17.5 μm. The actual tip parameters such as the normal force constant was determined by using resonance methods, and the torsional force constant was calculated from the expression for a long and thin lever (Cleveland et al., 1993).

3.1.2 FORCE DISTANCE ADHESION AND FRICTION WITH CONTAMINANTS OF VARIOUS CHEMISTRIES AND SIZES

The adhesion and friction properties have been measured on the selected insect species based on the hypothesis that contamination and wettability of wings are related to insect habit and/or SM values (Figure 3.1-2). Four different sized particles (three with hydrophilic chemistries) have been used to measure adhesion on the insect wing membranes. The dimensional and chemical differences (Table 3.1-1) were chosen to mimic contact conditions of particles which could potentially contaminate the structured insect cuticle surfaces.

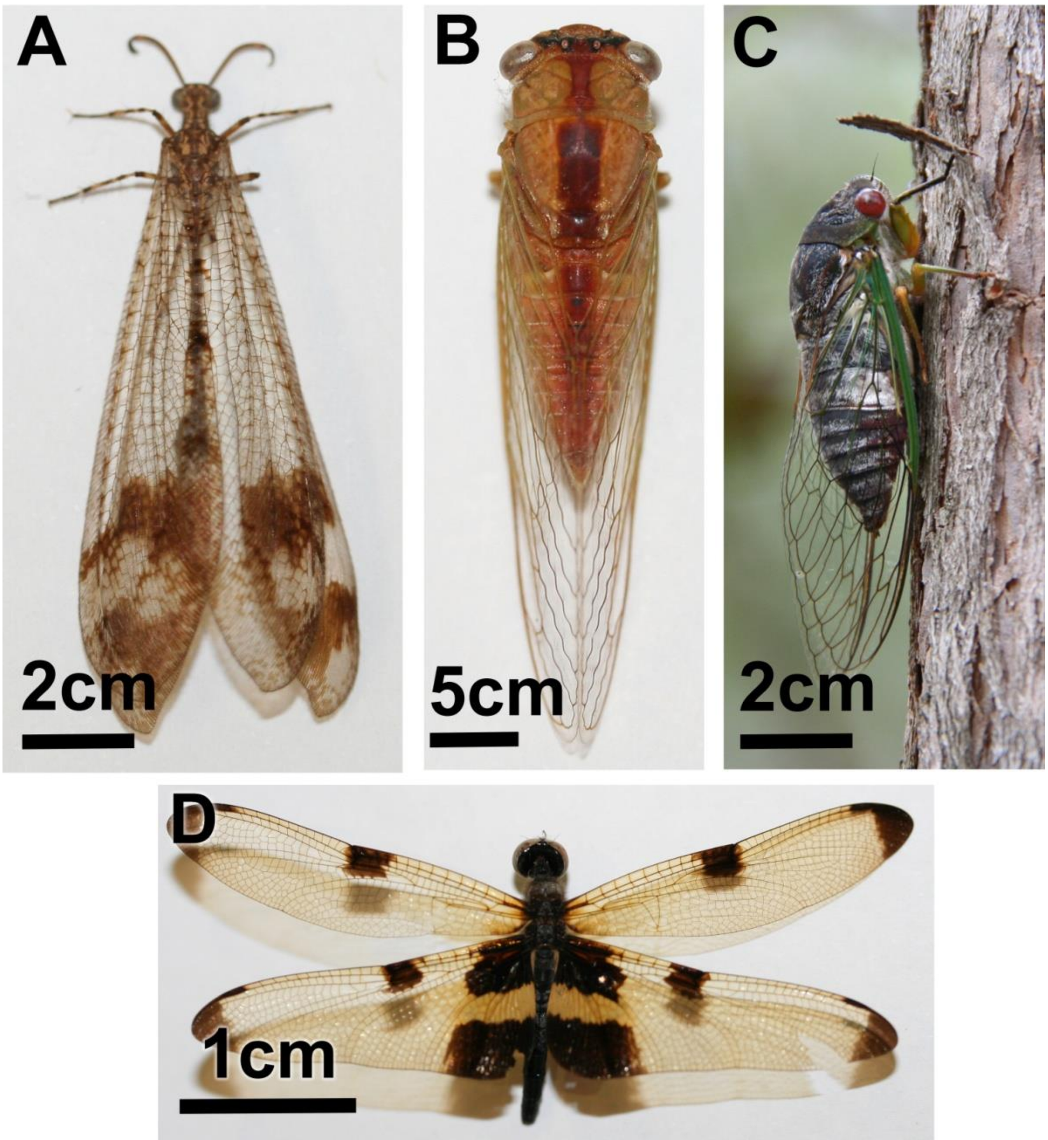

Figure 3.1-1. Insects selected for this work based on their SM and habits (A) *Glenoleon pulchellus* (B) *Cicadetta oldfieldi* (C) *Psaltoda claripennis* (D) *Rhyothemis phyllis chloe.*

Table 3.1-1. Dimensional parameters with standard errors of the artificial particles used for adhesion measurements. The values are averaged for 5 particles per particle type (35 in total).

Tip/Microsphere supplier	Chemical composition	Actual diameter (µm)	Actual surface roughness (1×1 µm^2 area) RMS (nm)
NDT	Silica	0.028 (0.006)	–
Bangs Laboratories Cat no. SS05N	Silica	4.53 (0.05)	2.3 (0.2)
Microspheres-Nanospheres Company Cat no. 147152-10	Silica	30.16 (0.17)	6.5 (0.3)
Nova-Pak® C_{18} Cat. No WAT015220	C_{18}	4.15 (0.06)	13.5 (2)

Table 3.1-2. Dimensional parameters with standard errors of the pollen particles used for adhesion measurements. The values are averaged for 5 particles per particle type (35 in total).

Pollen type	Structure height (SD) (µm)	Structure density (µm^{-2})	Structure width (SD) (µm)	Structure periodicity (µm)	Structure
Pimelea linifolia ssp	0.397 (0.128)	0.225	0.32 (0.022)	2.11	Furrows*
	0.5 (0.074)	0.047	2.4 (0.45)	4.61	Flat furrows
Grevillea ‘Red Sunset’	0.66 (0.17)	0.79	0.99 (0.28)	1.13	Furrows
	–	1	0.355 (0.117)	1	Pores**
Acacia fimbriata Golden wattle	0.67 (0.19)	0.007	10.4 (1.56)	11.8	Frame shaped furrow
	–	–	2.47 (0.25)	–	Outer frame furrow
	–	–	5.75 (1.11)	–	inner frame furrow
	–	–	0.63 (0.1)	–	Grooves
	0.18 (0.08)	1	0.55 (0.10)	1	Furrows

*Furrows – elongated/protruding structures on the pollen walls.

**Pores – holes/valleys in the pollen walls.

As well, natural particles (3 different pollens) were also interacted on the surfaces. Figure 3.1-3 shows SEM images of both the orientation of the particles used for adhesion measurements and their surface topographies (pollens and ca. 30 µm diameter silica beads). The pollens were chosen based on the 3 distinct topographies with various levels of roughness. As shown in Figure 3.1-3(A) the spherical *Pimelea linifolia ssp*. pollen will present one to several asperities with the insect cuticles upon contact. The pyramidal shaped *Grevillea* “Red Sunset” pollen (Figure 3.1-3(B)) demonstrated a homogeneous surface topography/roughness on all sides comprising of small holes and bumps. The *Acacia fimbriata* (Golden wattle) pollen (Figure 3.1-3(C)) demonstrated a patterned surface with two distinct levels of roughness.

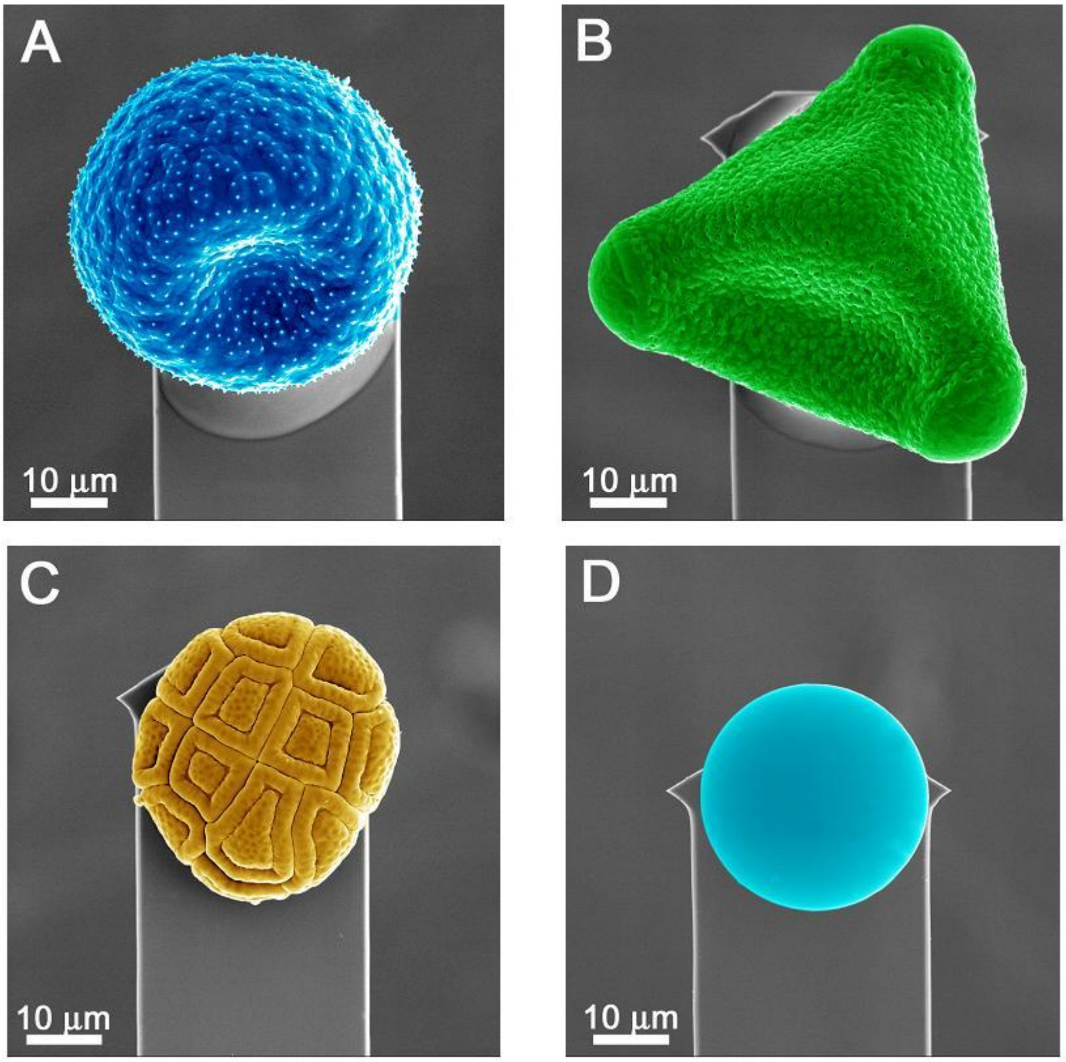

Figure 3.1-2. SEM images showing the orientation of the four types of contaminating particulates attached to AFM levers. (A) *Pimelea linifolia* ssp., (B) *Grevillea* 'Red Sunset', (C) *Acacia fimbriata*, and (D) 30 µm diameter silica bead.

The outer layer of the pollen grains comprises carboxylic acids cross-linked with saturated and unsaturated aliphatic chains with varying amounts of aromatics resulting in a hydrophobic surface (Thio et al., 2009). The dimensional parameters of the pollens are shown in Table 3.1-1. Figure 3.1-4 shows higher resolution SEM images of the three pollen surfaces used. The surface features of the artificial contaminants (Figure 3.1-3(D)) were analysed (e.g., surface roughness) using delta-like shaped projections (4 X 2 µm calibration grids with 1 µm spacing). An example is shown in Figure 3.1-5.

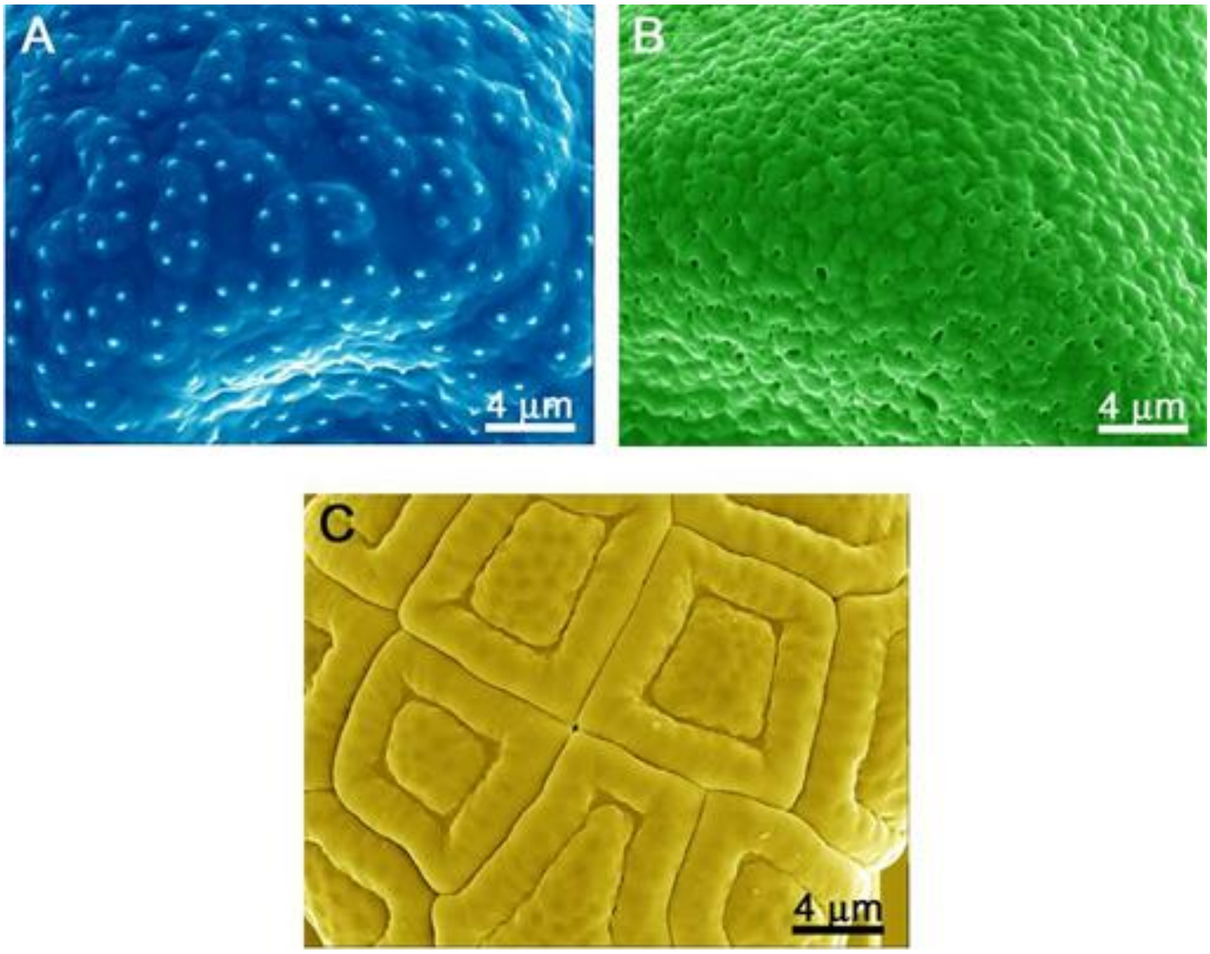

Figure 3.1-3. SEM images of the finer surface features of the three pollen surfaces used. (A) *Pimelea linifolia* ssp., (B) *Gravillea* 'Red Sunset' and (C) *Acacia fimbriata*.

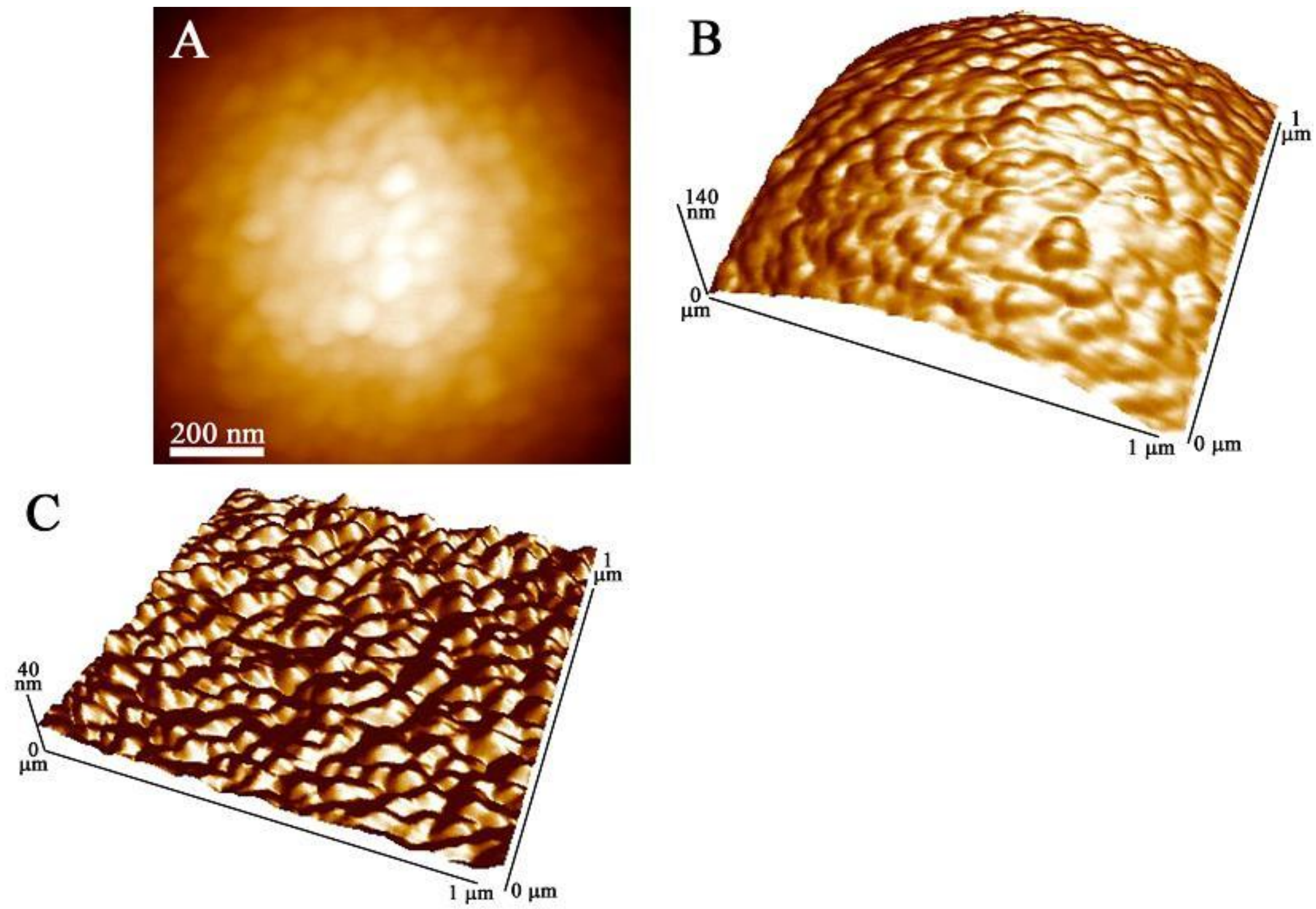

Figure 3.1-4. AFM images of a silica bead, revealing the finer surface structures. (A) A topographical image, (B) a 3-D representation, and (C) an artificially shaded and levelled 3-D image showing the fine surface features. The imaging was performed with the bead attached to a lever and scanned over a calibration grid, i.e., reverse imaging.

F-D curves were acquired at rates of translation in the z-direction in the range of 5 – 10 μms^{-1}. Each f-d curve consisted of 600 data points. The attachment procedure for particle (and hair) adhesion has been utilised in Section 3.1.3. Only particles that were attached directly underneath the cantilever (which can be seen under an optical microscope) were used for experiments. For a 350 • m long cantilever, as an effective length of only 340 • m reduces the measured force by ~9%.

Twenty five measurements per particle size (micro particle or nano tip)-substrate combination were acquired. A total of 5 particles were attached to cantilevers for each particle type (e.g., five silica beads of ~4.5 µm in diameter were used for adhesion measurements each yielding 25 measurements). Only pollen grains which exhibited the same orientation upon fixing to a lever were used for adhesion measurements. The F-D curves were analysed using the TopoMetrix analysis software package (TopoMetrix SPMLab, v4.0). The values were then entered into the software of SigmaPlot 10.0 whereby standard error values were obtained and presented as error bars.

Adhesion was measured under the conditions of the two surfaces coming into contact with no applied loading force, that is, adhesion represented the force of attraction that the particle-cuticle would experience where deformation of structures is minimised (length of line CD on Figure 2.1-8 is minimised) (Figure 3.1-6) and where the main contributing force involved is simply that of the adhesion of the particle to the surface.

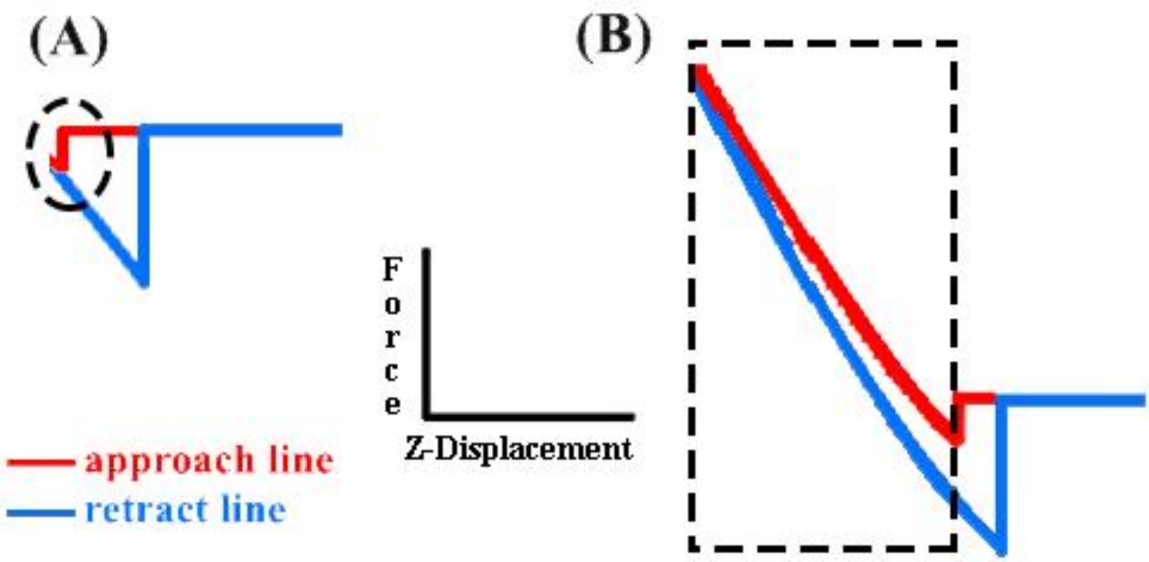

Figure 3.1-5. (A) Force distance curve representing the tip at the point of contact with the surface (highlighted with a circle) with a very low indentation force. (B) The surface indenting tip is driven into the surface with a predetermined load hence the longer line (framed in the dotted rectangle) corresponding to sections C-D and D-E of the generic F-D curve shown in Figure 2.1-8.

Two relevant parameters, namely radius of curvature and nano-scale roughness for AFM tip/microsphere, were determined quantitatively by SEM and reverse imaging on sharp spiky projections (manufactured by NT-MDT) (Section 2.1.1.1). The latter technique affords rapid and convenient topographical characterization of a microsphere attached to an AFM probe. Individual AFM tips were characterised by reverse imaging on a spiky biological array (cicada wing species *Cicadetta oldfieldi*).

Frictional forces were measured using friction loops (Section 2.1.3.1). Analysis was carried out by monitoring the torsional deformation of the lever during forward and reverse line scans 20 μm in length. The linear scan speed was 5 Hz. Friction measurements were carried out at the adhesional force loading (i.e., at a loading force which represented the adhesional force of contact between the wing membrane and the spherical particle).

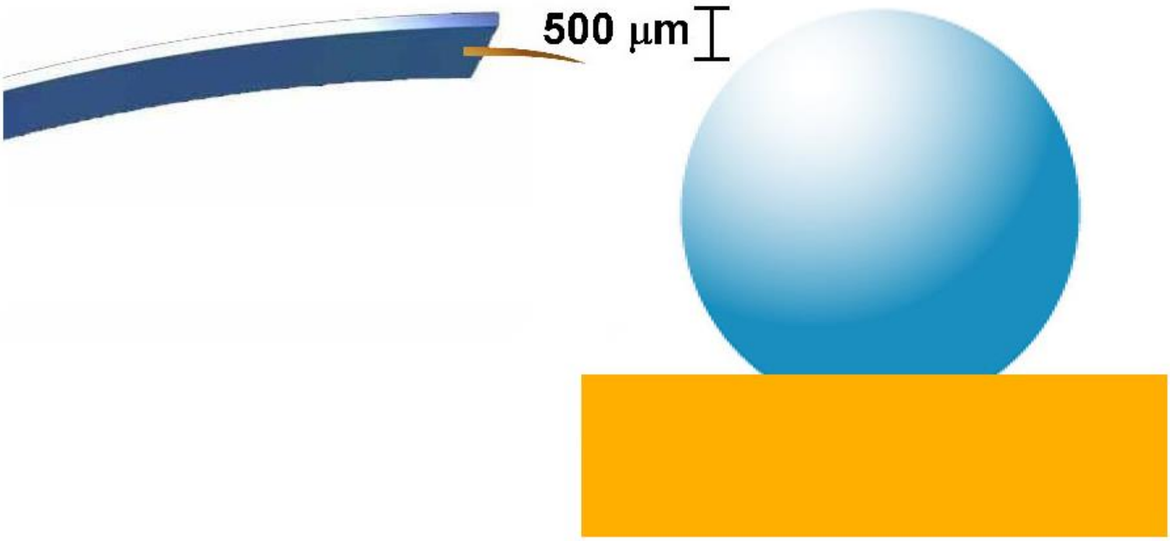

Figure 3.1-6. To avoid meniscus attraction to the hydrophilic lever, the hair was brought into contact to the Milli-Q water droplet from the side of the droplet roughly 500 · m from the top.

3.1.3 HAIR ATTACHMENT AND COATING

Craneflies (*Nephrotoma australasiae*) were captured in the Brisbane and Townsville areas of Queensland, Australia, in close proximity to waterways. The longest cranefly hairs (type 'a' hairs, Chapter 7, Figure 7.2-3) were scraped off the legs using a surgical scalpel and glued to the end of tipless levers under an optical microscope. The lever was attached to an in-house x, y and z positioning translator. This arrangement allows the small micron sized particles/bodies to be attached to the lever (Watson et al., 2004a). The free end of the lever was lowered onto the edge of a glue droplet (fast curing two-part epoxy resin) and then onto the end of the desired hair base followed by drying for 24 hours. Force measurements of the hairs spring constant required the hair base to remain fixed by its attachment to AFM non-compliant chips.

Polymer coating was conducted under an optical microscope. A droplet of a mixture of 10:1 base to curing agent of polydimethylsiloxane (PDMS) (Dow Corning, Sylgard-184) was deposited onto a concave microscope slide allowing it to spread for ca. 1min. A thin PDMS coating was achieved by positioning the lever with a cranefly leg hair attached at the free end at the edge of the PDMS droplet and gently lowering it ensuring full coverage of the hair, but not the lever itself. The hair was then slowly retracted and allowed to cure for a minimum of 48 hours under ambient conditions prior to any further experimentation. This resulted in a thin coating of the hair (thickness ranges from 50 to 150 nm) whereby only the nanometre sized structures were coated, leaving the main channels intact (Figure 7.2-5(A)). A thick PDMS coating was achieved by initially curing of the deposited PDMS mixture on the slide at 60°C for 3min before cooling back to room temperature prior to the dipping of the hair. This resulted in a slightly thicker consistency of the PDMS, ensuring a full coverage of the hair shaft channels as seen in Figure 7.2-5(B). The free end of the hair was then gently lowered to the edge of the PDMS droplet (five times in succession for a thick coat) with the fully covered hair then cured for ca. 48 hours under ambient conditions prior to experimentation.

Force measurements for hair mechanical properties and adhesion data were obtained by a TopoMetrix (Veeco Instruments) Explorer TMX-2000 SPM with a 130×130 μm^2 tripod scanner that has a *z*-range of 9.7 μm. Operated under air-ambient conditions (temperature of 22-23°C and 60-75% RH) and using the Force versus distance (F-D) mode, F-D curves consisting of 600 data points were acquired at rates of translation in the range of 2 – 5 $\mu m \cdot s^{-1}$ in the z-direction. Calibration along the z-direction was carried out according to previous studies (Watson et al., 2002, Watson et al., 2004b).

Five 'Beam-shaped' tipless levers (NT-MDT Ultrasharp) with stiffness constants (k_N) determined by accepted methods (Cleveland et al., 1993) were used on 10 individual uncoated cranefly hairs. Twenty F-D curves were obtained for both the force constant and the adhesion measurements before hairs were thin and thick coated with PDMS and new values also obtained after each coating had dried (24 hours). Stiffness of the hairs were obtained using methods described in (Gibson et al., 1996). Adhesion data between a hair attached to the lever and a 10 μL droplet of Milli-Q water was obtained with the droplet deposited on a slide previously coated with PDMS to ensure a hydrophobic substrate. The hair was brought into contact roughly 500 μm below the top of the droplet (Figure 3.1-7) in order to avoid the meniscus attraction between the hydrophilic lever and the Milli-Q water.

3.2 SCANNING ELECTRON MICROSCOPY (SEM)

SEM utilizes an electron beam with wavelength in the picometre range which allows imaging beyond the optical diffraction limit of optical microscopes. The beam is focused into a spot ~10 nm in diameter by electromagnetic lenses and rastered across the surface of the sample. Biological samples require a layer of electric conducting coating that can interact with the beam and backscatter them to be picked up by the detector before being converted to an image via software.

A JEOL 6300 field emission SEM was utilized throughout these studies. Samples were sputter coated with a 7-10 nm layer of platinum before being mounted on an aluminium pin-type stub with carbon-impregnated double-sided adhesive.

For chapter 4, a square of dried wing tissue was excised (approx. 3×5 mm^2) and imaged with a JEOL 6300 field emission SEM at 8 kV. Insect and particle features such as periodicity, height, width and spacing values for the nanostructuring were determined from SEM imaging of the top view and cross-sectional profiles of the wing cuticle. The 7-10 nm Pt coating layer was taken into account when determining the width and density of the surface structures.

In Chapter 7 individual hairs were attached to the AFM probes and wing/leg tissues (wing-approx. 3 × 3 mm, leg-approx. 1 mm).

3.3 PHOTOGRAPHY

Eight megapixel resolution photographs were obtained using a Canon Digital 350D SLR and a Canon Ultrasonic EF-S 60mm macro lens. Cropping, adjustment of brightness and contrast and scale bars were applied using Photoshop 7.0.

3.4 OPTICAL MICROSCOPY

An AIS – Optical Microscope VG8 attached with a Panasonic colour CCTV camera WV-CP410/G as well as a XSP Series Compound Microscope (York Instruments) were used. These were placed in a vertical, horizontal or inverted position to obtain top, side and bottom views, respectively. Magnifications of up to 40X were used.

3.5 POLYDIMETHYLSILOXANE (PDMS)-A POLYMER FOR INSECT STUDIES

Widely used in the biochemistry/biomedical field the highly biocompatible and low cost PDMS has great potential application in anti-fouling coatings (Kim et al., 1999, Hillborg and Gedde, 1999, Pike et al., 1996). Transparency, surface hydrophobicity, constant and high ductility over a wide range of temperatures, low toxicity, high electrical resistance, long-term stability and flexibility (Olah et al., 2005) are amongst its many useful physical, mechanical and chemical properties that outmatch traditional materials such as glass, quartz and silicon. Its low density makes it less difficult to create these small structures especially the case where it is used as substrate for creating micro/nano structures, e.g., microfluidic devices (Ranjit Prakash et al., 2006, Ren et al., 2001). Also the PDMS polymer exhibits intimate contact with the master or the harder substrate that supports it (Luo et al., 2006) and its high elasticity means it will not deform when peeled off and no residues are left behind (Ren et al., 2001). PDMS is used in Chapters 4, 5 and 6 to replicate insect cuticle structures. Comparing the contact angles of the replicas from various insect isolates the relative importance of topographical and chemical effects. In Chapter 7 the topographical features of cranefly hairs are coated with PDMS to gain an understanding of the importance of the features on wettability.

3.6 CONTACT ANGLE MEASUREMENTS

A horizontal microscope (AIS-OPTICAL, model: AIS-V8G, magnification: 40X) with digital capturing (Panasonic Colour CCTV Camera, model: WV-CP410/G) of the images was used for precise measurements of static CA. Ten measurements per droplet were taken on images captured at ambient conditions of 21°C and RH of 65-75%. Left and right angles between the sample surface and the tangent line to the droplet were considered as one measurement. For droplets on the insect wing surfaces the apparent static contact angles were measured. Five droplets of 10 μL Milli-Q water were applied to each of the wing membranes, where possible, near the dorsal cell region. For example cicada contact angles were taken in the wing region M (Figure 3.6-1).

This region was used in order to accommodate the droplet footprint without the effects/influence of the vein structure. Smaller sized droplets were difficult to place on the superhydrophobic insect cuticle surfaces due to the adhesion between the water droplet and the syringe needle being stronger than the force of gravity and adhesion of the cuticle surface. To remove the effects of the fine hairs levitating the water droplet above the lacewing cuticle membrane, smaller sized droplets were placed by spraying a fine water mist onto the membrane.

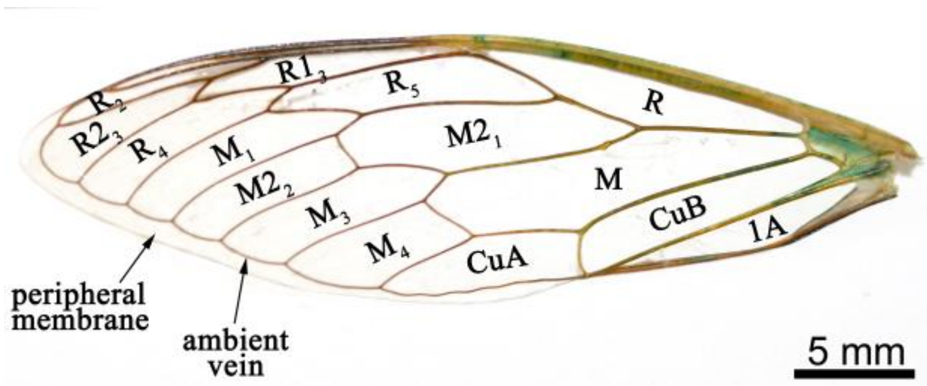

Figure 3.6-1. Venation and regions on an insect wing (example cicada (*Psaltoda* sp.)).

3.7 CHAPTER SUMMARY

Insects were selected for this thesis based on their association with water and SM values. Most of the experiments were conducted on the dorsal cell region of their wing. Preparing the samples of this region for AFM and SEM require careful scalpelling and mounting on stubs. Attachment of contaminant particles to tipless cantilevers and coating of the hairs before interacting them with water were conducted under an optical microscope. The names of the tools, instruments and materials and scientific names of the samples and pollens used in this thesis and their procedures involved were also included in this chapter.

4 FOULING OF NANOSTRUCTURED INSECT CUTICLE: SURFACE STRUCTURING OF CUTICLE

4.1 INTRODUCTION

The atmospheric environment surrounding insects contains a multitude of biological and anthropogenic particulate matter which can potentially contaminate the wing cuticle; for example silica dust and plant material. Pollen grains are the most abundant component amongst the floating particles in the air (aeroplankton) surrounding most terrestrial organisms including human beings (Linskens and Cresti, 2000). It has been known for some time that pollens and mould spores, or at least components of them, can trigger symptoms of allergic respiratory diseases such as asthma and hay fever (Linskens and Cresti, 2000, Ylipanula and Rantiolehtimaki, 1995, D'Amato, 2002, Carinanos et al., 2004, Burney et al., 2008). A rise in respiratory allergic symptoms has also been attributed to pollen fragments which can adhere to other pollutant surfaces (e.g., diesel exhaust particles). Thus the interaction of pollen grains with various surfaces is of great interest in terms of distribution, transport and capture of these pollinic allergens. Interestingly, recent studies have also shown that pollen of genetically engineered and modified plants have the potential to kill certain insects (Losey et al., 1999).

Other potential airborne contaminants originate from soils. Naturally occurring silicate particles composed principally of silicon dioxide (SiO_2) such as quartz, can comprise as much as 90–95% of the sand and silt fraction of soil (Smith and Lee, 2003), and present the highest health risks (Smith and Lee, 2003, Ormstad et al., 1997). Respirable quartz is commonly found in soil dust, although weathering and chemical reactions may make it less fibrogenic than the freshly fractured quartz found in occupational dust from quarrying and sandblasting (Ormstad et al., 1997). Exposure to, and inhalation of, a combination of various air-borne particulates have been found to contribute to various diseases including lung cancer (Knaapen et al., 2004). Silica dust has not only been linked to lung disease, but also as a contributor to lung cancer, silicosis, pulmonary tuberculosis, emphysema and immunologic reaction (Ding et al., 2002, Hnizdo and Vallyathan, 2003). Thus, like pollen, enhanced mechanisms for shedding silica particles are of great interest. The capture and isolation of these particles (silica, pollen, etc.) is advantageous in some circumstances (e.g., air-conditioning filters, cleaning systems), but in most human habitats adhesion is highly undesirable (furniture, flooring, fixtures, clothing).

As well as the health concerns associated with silica and pollen, these bodies also represent a ubiquitous source of hydrophobic and hydrophilic particles which come into contact with insects and can potentially foul the surface. Fouling in the marine and terrestrial environments (especially where water can accumulate) is a significant economic and environmental problem (Schultz et al., 2011, Yebra et al., 2004). Until recently, biofouling control has focused on biocidal antifouling coatings, but there is now an urgency to develop effective non-biocidal antifouling alternatives. Increasingly, non-biocidal solutions to biofouling are being sought from nature (e.g., de Nys and Steinberg (de Nys and Steinberg, 2002); Scardino and de Nys (Scardino and de Nys, 2011)). New surface-based technologies in particular are being inspired from biomimetics (e.g., the Lotus leaf) as physical surface effects, or surface bound chemical signals, have the advantage of eliminating effects on non-target organisms(Genzer and Efimenko, 2006, Ralston and Swain, 2011, Scardino and de Nys, 2011). While these superhydrophobic surfaces may provide useful templates for biofouling prevention, other structuring such as hydrophilic micro-nano patterned surfaces where contact with water is preferred over biological interactions may also guide the development of new antifouling coating (Marmur, 2006).

A range of cuticle nanostructures are examined in this chapter on a number of insect species and their corresponding cuticle wetting properties were investigated in Chapter 5. In Chapter 6 micro/nano adhesion of contaminating particles (silica, C_{18} and a variety of pollen grains) on these insect species were measured and the results were correlate to their cuticle structures and wetting properties. Insect species with large wings and/or a high SM value and/or a close association with water in their life history are our general focus. Insect species were also chosen based on the differing topographical landscape of their wing cuticle.

4.2 TOPOGRAPHICAL CHARACTERISATION OF INSECT WING CUTICLE

The surfaces of the insect species studied showed a wide range of wing membrane structuring. The structures range from periodically aligned structures through to an inhomogeneous arrangement as demonstrated in Figure 4.2-1. The structures also demonstrate (super)hydrophobicity and hydrophilicity. This diversity in surface structuring, as well as insect behaviour, provided the impetus of the selection of species in this study. The micro-nano structuring is characterised in Table 4.2-1 listing the relevant geometrical parameters such as shape, spacing, depth and width of the structures.

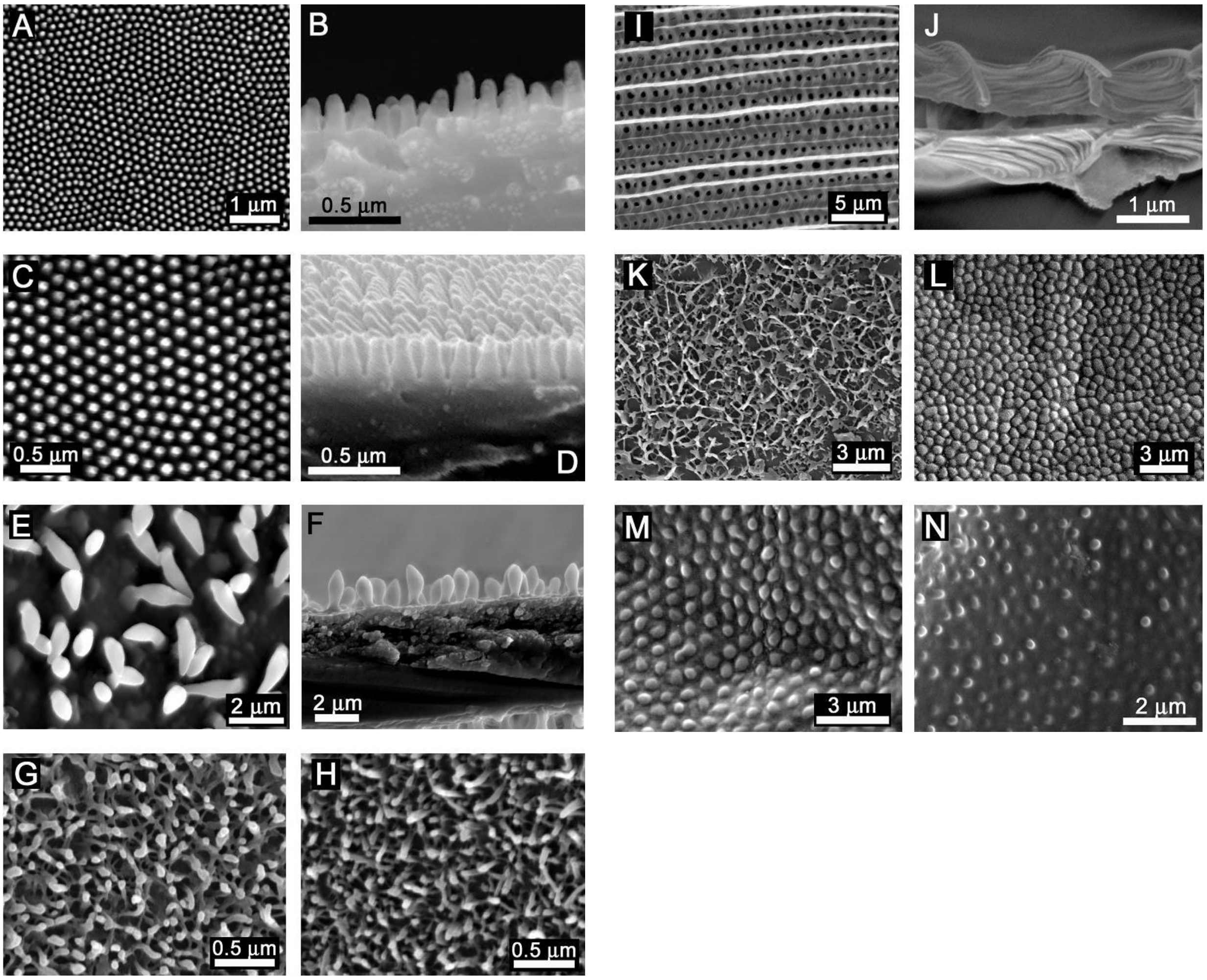

Figure 4.2-1. Topographical SEM images: (A) & (B) *Psaltoda claripennis* (top and cross-section, respectively). (C) & (D) *Cicadetta oldfieldi* (top and cross-section, respectively). (E) & (F) black region of *Gudanga* sp. *nr adamsi* (Black cicada) wing membrane (top and cross-section, respectively). (G) & (H) comparable structures found on the dragonfly (*Rhyothemis phyllis chloe*) and planthopper (*Desudaba psittacus*) wing membranes, respectively. (I) micron, and (J) sub-micron structures found on a moth wing (*Prasinocyma albicosta*). (K) Lacewing *(Glenoleon pulchellus*). (L) flower wasp (*Scolia soror*) nanostructures. (M) Broad bump structuring of the superhydrophilic termite *Schedorhinotermes* sp.. (N) bladder cicada (*Cystosoma schemltzi*).

Table 4.2-1. Geometrical parameters of cuticles from insect species investigated in this study.

TYPE/SPECIES	HEIGHT (nm)	STRUCTURE DENSITY (/μm^2)	STRUCTURE WIDTH (Maximum) (nm)	STRUCTURE SPACING/ PERIODICITY (nm)	SHAPE
SUPER HYDROPHOBIC CUTICLE					
Cicada 1 *Psaltoda claripennis*	200 (30)	37	90 (20)	170	Spherically capped, conical
Cicada 2 *Cicadetta oldfieldi*	200 (28)	42	80 (15)	200	Spherically capped, conical
Black cicada *Gudanga* sp. nr *adamsi*	Forewing – 15000 (1900)	0.24	680 (70)	2100	Diamond-like shape
Dragonfly *Rhyothemis phyllis chloe*	350 (35)	43	80 (10)	150	Rods
Planthopper *Desudaba psittacus*	400 (79)	52	60 (10)	150	Rods
Moth *Prasinocyma albicosta*	Valley/peak dist. 500 (100)	-	120 (15)	Longitudinal ridge spacing - 1500 Ridge width: Thin – 120; thick – 390	Scales, longitudinal ridges, lateral crossbeams
Lacewing *Glenoleon pulchellus*	950 (100)	-	80 (50)	-	Interconnected netting composed of ridges
HYDROPHILIC CUTICLE					
Flower wasp *Scolia soror*	187 (18)	2	630 (90)	400	Curved projections
Bladder cicada *Cystosoma schmeltzi*	117 (34)	2 (0.6)	321 (80)	800	Curved projections
Termite *Schedorhinotermes* sp.	150 (-)	0.01	300 (-)	850 (-)	Curved projections

4.2.1 SUPER HYDROPHOBIC CUTICLES

The transparent cicada wing membranes of *Psaltoda claripennis* are covered with a periodic topography. The structures are shown in the topographical SEM images in Figure 4.2-1((A) and (B) show top views and the membrane cross-sections). The arrays consist of hexagonally packed spherically capped conical protuberances with a spacing and height of ~ 200nm and radius of curvature of ~25-45 nm at the apex. Similar features have been found on the wings of a number of other cicada species including *Aleeta curvicosta*, *Tamasa tristigma, Macrotristria angularis, Cicadetta oldfieldi* (Figure 4.2-1 (C) & (D)) and *Thopha saccata* ((Watson et al., 2008c)). The features are present on all areas of the dorsal and ventral wing membrane. A previous study has demonstrated the functional effectiveness of similar structures as an antireflective surface which presumably helps to camouflage the insect from predators (Watson et al., 2008c). The surfaces also demonstrated low adhesion with hydrophilic particles (Watson et al., 2008c). The multi-functional nature of the structures appears to be a common feature of the cuticle found in many insect species.

The other superhydrophobic cicada species examined ((Black cicada - *Gudanga sp. nr adamsi*) had coloured as well as non-transparent wing regions as opposed to the species discussed above which all have transparent fore and hind wings. The transparent regions on the black cicada wing membrane (hind wing) showed the same well-ordered structure size, shape and periodicity as found on other cicada with completely transparent wings. Interestingly, the non-transparent coloured regions of the forewing (black in colour) showed dramatically different structuring. It was composed of a less ordered surface with individual diamond-shaped structures almost one order of magnitude larger in height and width (width at widest point, Figure 4.2-1 (E) & (F)). This provides strong evidence for specific dimensional structure size/shape for specific functionality on selected regions of the wings. Regions of the wing where the antireflection property is required have the necessary structure dimensions (less than the wavelength of light (Watson et al., 2008c)) while other coloured regions are not restricted by this wavelength condition.

The dragonfly (*Rhyothemis phyllis chloe*) and planthopper (*Desudaba psittacus*) (Figure 4.2-1(G) & (H) respectively) exhibited comparable surface topography with rod-like structures forming a layer of structured matting. These structures are similar to those found on damselflies (Cong et al., 2004). Cong *et al.* (Cong et al., 2004) suggested a number of possible functions for the wax-like covering including intra/inter-specific communication based on ultraviolet light reflection of the layer. The covering was also suggested to protect the insect against water when in contact.

The moth (*Prasinocyma albicosta*) topography showed scales with a typical overlaying tile type arrangement as found on many butterfly/moth species (Carinanos et al., 2004). These scales exhibited micron (SEM image in Figure 4.2-1(I)) and submicron structuring in the form of longitudinal and lateral ridges as seen in the cross-sectional SEM image of a single scale in Figure 4.2-1(J). A number of functional properties have been attributed to scales on butterflies including camouflage display, signalling and possibly thermo-regulation control (Cong et al., 2004, Gorb et al., 2000, Vukusic et al., 2004). Moth and butterfly scales are typically super/hydrophobic and can detach as an aid for protection against highly adhesive surfaces (e.g., spider webs).

The surface of the lacewing (*Glenoleon pulchellus*) showed interconnected ridges forming a dense netting on the cuticle surface (Figure 4.2-1(K)) and (Chapter 8). The vein regions were characterised with an array of macrotrichia (fine hairs). Macrotrichia have been found to add a secondary layer of protection against surfaces with which the insect may come into contact(Watson et al., 2010b). The lacewing surface of the species *Chrysoperla carnea* has been previously studied whereby the wing was exposed to a fine dust of silica particles under fogging conditions and was shown to exhibit a high degree of non-contaminability(Wagner et al., 1996).

4.2.2 HYDROPHILIC CUTICLES

The flower wasp (*Scolia soror*) (Figure 4.2-1(L)) and bladder cicada (*Cystosoma schmeltzi*) (Figure 4.2-1(N)) both exhibited surfaces with similar features represented by relatively large sized curved projections (bumps), flat (low in height) and spaced many hundreds of nanometres apart (centre-centre distance). A similar type of insect topography (broad bumps) to these two species have been reported in a previous study of micro/nano structuring on the termite (*Schedorhinotermes* sp.) wing membrane (Figure 4.2-1(M))

(Watson and Watson, 2004). The study suggested that the wing membrane topography (array of bumps) may improve flight efficiency by acting as a series of stabilizing elements designed to handle loading forces.

4.3 CHAPTER SUMMARY

Table 4.2-1 summarises the geometrical parameters of cuticles from insect species investigated in this study. These measurements were taken from SEM images of the cuticles and the generally tall, narrow and dense structures on the superhydrophobic insects can be distinguished from the generally broad and sparse structures on the hydrophilic insects. The variation in the shapes and sizes of the structures is due to the need for different functionalities on the cuticle and the most interesting structure is seen between the different colour regions of the Black cicada wing.

5 WETTABILITY OF NANOSTRUCTURED CUTICLES

5.1 CONTACT ANGLES AND INTERACTION WITH WATER

Separating the contributing effects of topographical structuring and chemistry is not always a trivial exercise. Wettability however incorporates both the chemical and topographical components of the surface and is a useful parameter to relate to other measureable properties such as adhesion and friction. The result of these two contributing components (structure and chemistry) will thus influence the interfacial properties and functional efficiency of insect wing membranes.

Many insects (especially superhydrophobic species) already have chemistries which result in contact angles that have reached the near upper limit for what can be achieved on flat surfaces (Holdgate, 1955). Thus topographical architectures resulting in increased roughness is one way to improve hydrophobicity on an already low energy surface. The non-wetting surfaces offer survival value to insects as they afford resistance to wetting by rain and other water surfaces they may encounter.

The wettability (apparent contact angles (θ_C and θ_W)) of the insect wing cuticles in this study are shown in Figure 5.1-1(A). Many of the membranes represent superhydrophobic surfaces with CA close to or above 150°. A typical example is shown in Figure 5.1-1(B) (cicada with structure height and periodicity ~200 nm) where it is evident from the image that the water droplet gains negligible energy through absorption to compensate for any enlargement of its surface area. For comparison, Figure 5.1-1(C) shows the interaction of water with a flat (non-structured) polydimethylsiloxane (PDMS) sample. This polymer demonstrates a hydrophobic surface with a measured θ_0 of ca. 101-105° (in good agreement with values reported in the literature (Sun et al., 2006)) and highlights the hydrophobic character of the wing membranes.

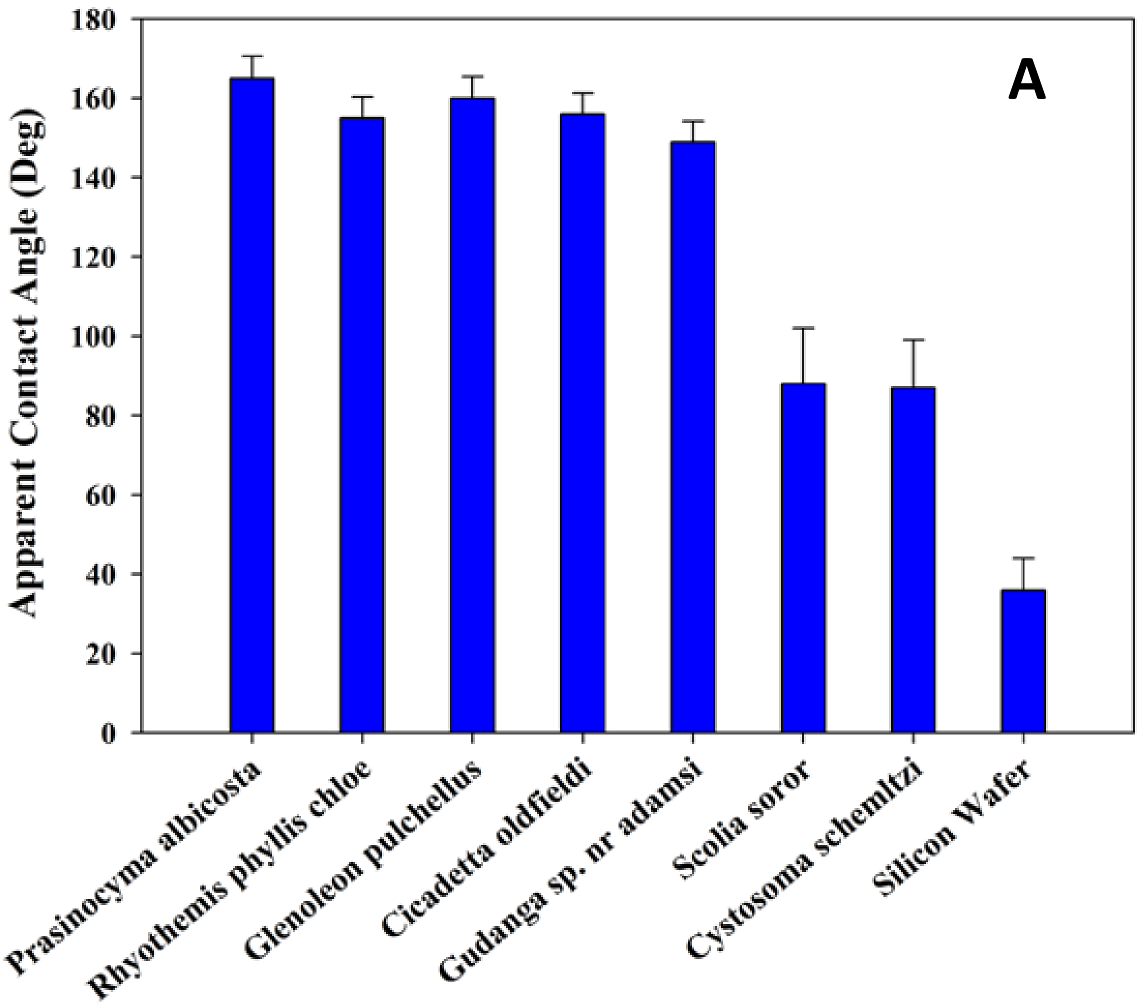

Figure 5.1-1. (A) Graph displaying the species type as a function of contact angle.

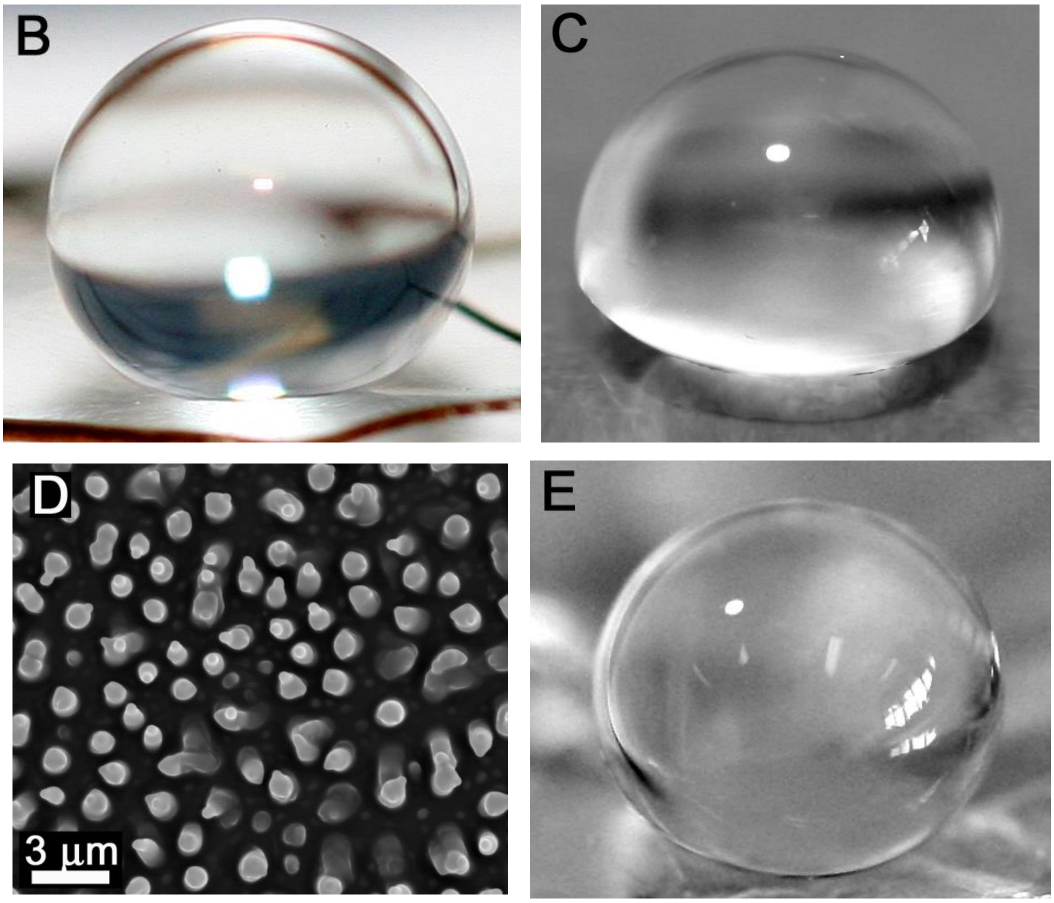

Figure 5.1-1. A 10 μL droplet deposited on (B) a cicada wing membrane, and (C) hydrophobic PDMS surface. (D) & (E) shows the PDMS replica of the cicada *Tosena sybilla* and the interaction of a water droplet with a polymer (PDMS) replica of the cicada *Gaeana cheni* respectively.

There exists a spectrum of contact angles due to inhomogeneous chemistries and roughness of membrane surfaces. For example infrared microspectroscopy (with a highly focused infrared probe beam in dimensions of approximately 8 μm in diameter) shows that the heterogeneous distribution of the cuticular waxes across the wing of *Psaltoda claripennis* is a result of aggregation of the long chain hydrocarbons (Tobin et al., 2013). Similarly the ester functional groups showed spatial variability on the wings of the damselfly *Ischnura heterosticata* (Hasan et al., 2012). The intensity of the amide peaks (1590-1490 cm^{-1} and 1700-1600cm^{-1}) is similar across the cicada wing. On the damselfly the heterogeneity is lower than the ester function groups implying a more even distribution of chitin and other proteins across wings of both insects(Tobin et al., Hasan et al.). Variable distribution and shape of the structural tips also contributes to the variety of contact angles displayed.

There are a number of theories to express the superhydrophobic condition all of which have certain assumptions and limitations(Cassie and Baxter, 1944, Gao and McCarthy, 2007a, Herminghaus, 2000, Shirtcliffe et al., 2010, Wenzel, 1936). Cassie-Baxter(Cassie and Baxter, 1944) expresses the superhydrophobic state in terms of a number of interfaces; a liquid-air interface with the ambient environment surrounding the droplet and a surface under the droplet involving solid-air, solid-liquid and liquid-air interfaces (Equation 2.2-4 and 2.2-5) and necessitates the surface to have the required roughness to allow air in topographically favoured regions such as troughs and surface depressions. Thus topographies which increase the air-water interface and minimise the solid-liquid contact area will lead to higher contact angles.

The C-B model can also be applied to determine the contact angle of an array of hemispherical-top protrusions (a close approximation to the structures shown in Figure 4.2-1 (C) and (D) for the cicada *Cicadetta oldfieldi* and also the transparent regions of the black cicada) using

$$\theta_C = \cos^{-1}\left[-1+\phi_B\left(\cos\theta_0+1\right)^2\right]$$

Equation 5.1-1

where ϕ_B is the ratio of the basal area of the protrusion over the total area and θ_0 is the ideal contact angle of water on a smooth surface of identical chemistry (θ_0 ~ 105° in the present case (Watson et al., 2008c)). The predicted apparent contact angle for the cicada membrane is ~ 150°. This value correlates well with the experimentally determined values shown in Figure 5.1-1(A). The cicada species with transparent wing membranes likely compromise the geometrical structure parameters due to the antireflection constraint as mentioned above. Even so, the membrane still manages to achieve superhydrophobic contact angles. A recent study of fabricated superhydrophobic nanostructures with comparative spacing and height to the cicada arrays reported measured contact angle values similar to our results (Martines et al., 2005).

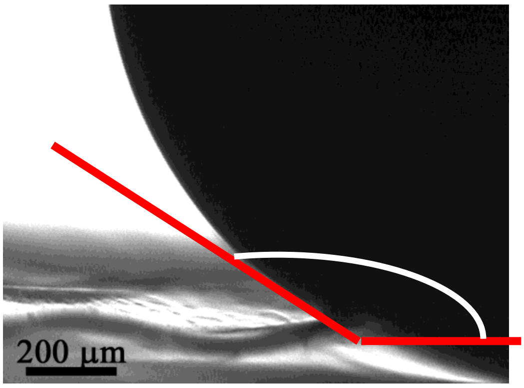

Figure 5.1-2. An optical microscope image of a water droplet resting on the wing membrane of a cicada revealing an apparent contact angle (CA) of ca. 150° with the surface.

Many of the other insect species in this study demonstrated specialised topographies for minimising the solid-liquid contact area and maximising the liquid-air contact resulting in high contact angles. The non-transparent cicada wing cuticles of *Gudanga* sp. for example, present structures which satisfy a number of the above contact conditions. The diamond-like shape demonstrates 'model' features for lowering the solid-liquid contact area and allowing a larger pocket/volume of air to occupy the volume beneath the water droplet. As well the shape minimises the amount of material required and hence reduces the wing and thus insect weight. The largest spacing between individual structures as seen in Figure 4.2-1 (E) and (F) is less than 5 μm and this may suggest that this might be near a critical distance for structures of these heights (several μm) interacting with water. Indeed a study on fabricated surfaces shows that larger spacings may be more susceptible to complete wetting (Bhushan and Jung, 2008). It may be advantageous for the cicada membrane to resist water under a variety of conditions so as not to invade or make contact with the underlying surface between asperities increasing the solid-liquid contact or promoting a transition to the fully wetted state.

It has been suggested that cicada microstructures on the wings could act as 'natural templates' to transfer wetting properties onto materials such as polymers (Watson and Watson, 2004). Watson *et al.* (Watson et al., 2008c) have previously tailored a polymer (PDMS) using this templating procedure on the wing membrane of the cicada *Aleeta curvicosta* (Watson et al., 2008c). Attempts to duplicate the black cicada membrane with a polymer replica (PDMS) proved difficult due to the unusual structure shape. The replica features only formed to a height of several hundred nanometres (Figure 5.1-3(A) and (B)). Interestingly these sized features (height and spacing) did not result in the polymer exhibiting superhydrophobic behaviour. However, structures of similar dimensions (height and spacing) to *Gudanga* sp. can be found on other wings of coloured cicada species (e.g., *Tosena sybilla* and *Gaeana cheni* in Figure 5.1-3(C) and (D) respectively). Figure 5.1-3(C) shows a PDMS replica of the cicada *Tosena sybilla* (structure height ~2 μm, spacing ~2 μm). Droplets on these features showed superhydrophobic contact angles. Even PDMS replicated structure heights approximately half the height of *Gudanga* sp. (produced from *Gaeana cheni* ~750 nm) produced superhydrophobic interactions (Figure 5.1-3(D)).

The images in Figure 5.1-3 illustrate the increased hydrophobicity when roughness is introduced to the polymer surface at these dimensions. The diamond structuring and colouring found on the black cicada may also be multi-functional providing similar attributes to some butterflies e.g., camouflage display, signalling, and thermo-regulation control.

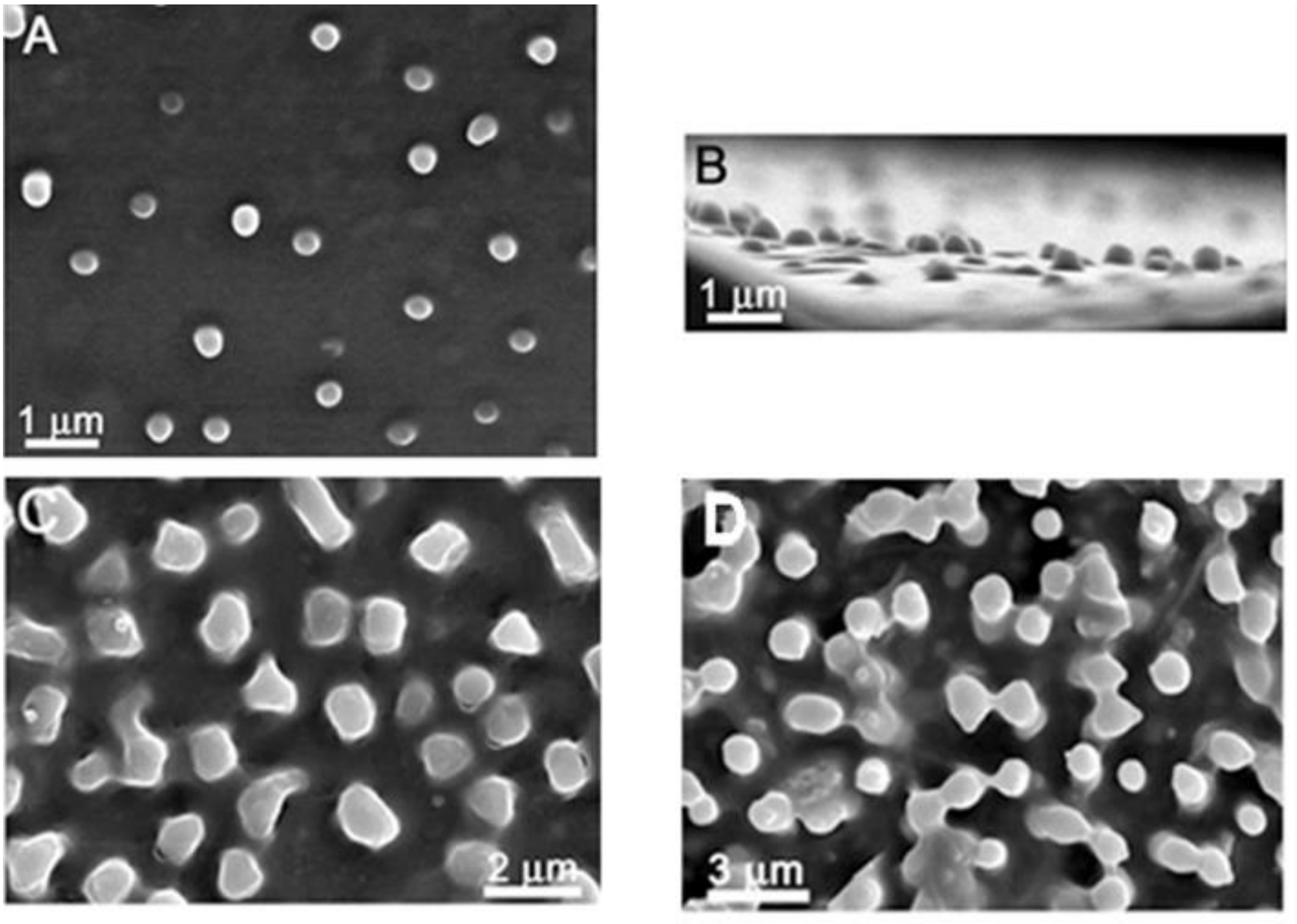

Figure 5.1-3. SEM images of a PDMS replica of the top (A) and side (B) view of the black cicada (*Gudanga* sp.) and the top view of the coloured regions found on the cicada wings of *Gaeana cheni* (C) and *Tosena sybilla* (D).

The dragonfly (*Rhyothemis phyllis chloe*) and planthopper (*Desudaba psittacus*) demonstrated superhydrophobic contact angles. Even though the asperity density is high, the small width of the asperities (Figure 4.2-1(G), (H)) will increase the air pocket volume by the 3-dimensional 'undergrowth' of surface matting on the membrane. The moth also demonstrated a superhydrophobic contact with water. The topography has an anisotropic hierarchy of roughness with the scales and ridges of different length scales allowing minimisation of contact with water bodies.

The bladder cicada and flower wasp exhibited surfaces which are more easily wetted than the other insect species examined, with contact angles below 90°. The hydrophilic nature of these surfaces is in stark contrast to the superhydrophobic topographies examined. The habit of the bladder cicada is sedentary in nature with limited flying (Moulds, 1990). The large green wings are said to serve as a camouflaging blanket for the insect in dense foliage (Moulds, 1990). This cicada has intense green wings similar in shape to leaves. The camouflage is so effective that it can take a few minutes to locate a 'singing' specimen less than 0.5 m away (Moulds, 1990). Interestingly, their camouflaging green colour is lost to a significant degree when dehydrated (Moulds, 1990) (Figure 5.1-4(A) and (B)). Thus our observation of a hydrophilic wing cuticle is in agreement with these factors and possibly functions to retain condensed moisture and thus camouflage.

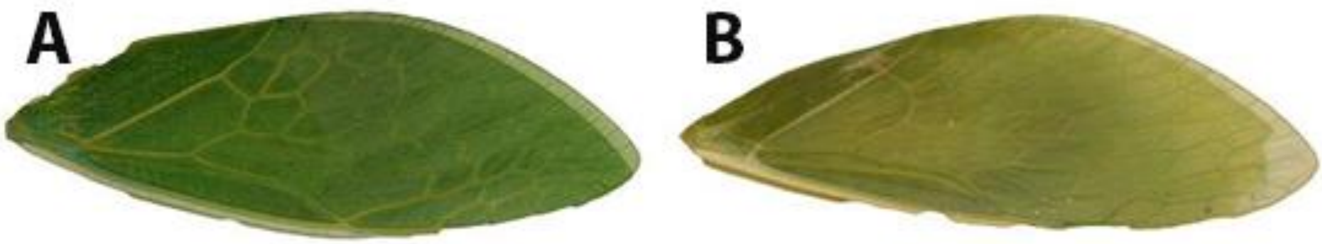

Figure 5.1-4. A 'fresh' (A) and dehydrated (B) forewing of the bladder cicada, *Cystosoma schmeltzi*.

The hydrophilic black flower wasp has a similar cuticle structuring to the bladder cicada. The hydrophilicity of the flower wasp wing is highlighted by the interaction with moving droplets as experienced under conditions of precipitation in the supplementary movies S1 and S2 (found on Taylor & Francis (Hu et al., 2011b)). In contrast, interaction of similar sized droplets with the superhydrophobic species results in water droplets bouncing off the surface. These insects are generally solitary and do not make communal nests. In mid to late summer, they often form small swarms flying low over areas such as turf, shrubs and compost heaps and are commonly seen taking nectar from flowers. A common feature of this insect is that it is an extremely strong flyer. This wasp species were observed in light rain conditions where the mobility of the insect seemed unhindered. Thus the insect appears to have sufficient strength and/or wing flapping frequency to remove water droplets quickly upon contact and thus maintain flight even though the wing membrane is hydrophilic.

Interestingly a recent study has examined the wetting properties of the termite *Schedorhinotermes* sp**.** which has a topography very similar to the flower wasp (Watson et al., 2011a). These particular termites typically fly after rain periods (typically at night) and thus do not come into contact with mobile droplets during flight. The insect displays a hydrophilic structuring on their wings with a small scale roughness which is not dimensionally sufficient to introduce an increase in hydrophobicity. The lack of hydrophobicity allows the termite to be hydrophilically captured at locations (for example on wetted rocks (Figure 5.1-5(A) and leaves (Figure 5.1-5(B)) where water may be present in large quantities and sufficient for the initial colonization period.

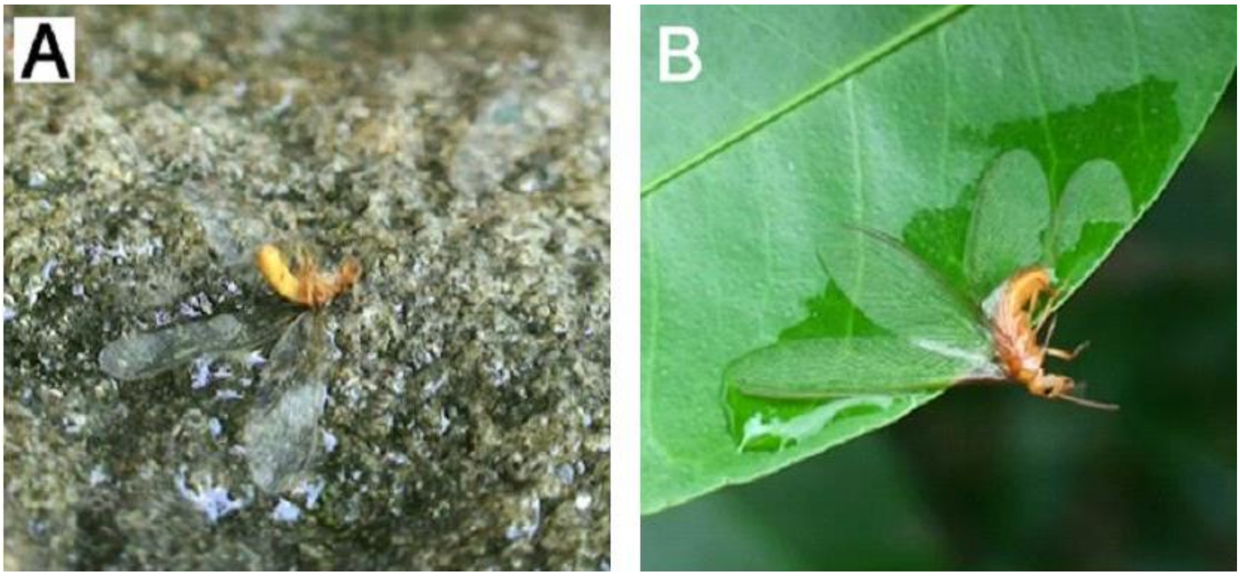

Figure 5.1-5. (A) and (B) Hydrophilic *Schedorhinotermes sp.* termite stuck to a wet rock and leaf surface rendering the insect immobilised.

5.2 CHAPTER SUMMARY

Successfully replicating the superhydrophobic cuticle structures onto PDMS (θ_0 of ca. 101-105°) creates a superhydrophobic polymer surface thus showing the significance of the topographical feature in anti-wetting. The dense surface structures which are spaced typically less than 5 μm resist wetting the troughs and thus reduce solid-liquid contact. The composite wetting regime is responsible for the apparent contact angle which can be expressed by the Cassie-Baxter equation.

6 ADHESION OF NATURAL AND ARTIFICIAL CONTAMINANTS

6.1 ADHESION FORCE MEASUREMENTS

The adhesion between the various particles (*Pimelea linifolia* ssp., *Grevillea* “Red Sunset” and *Acacia fimbriata* (Golden wattle) pollen, and Si and C_{18} spherical particles described in Section 3.1.2) and a flat hydrophilic silicon sample with a native oxide layer was used for comparison as it highlights the adhesional differences between the various surfaces. For the case where the silica sphere comes into contact with the silicon dioxide surface, meniscus forces at the point of contact between the tip/particle and the surface accounted for the high adhesive forces. The meniscus force (*F*) between a sphere and a flat surface can be expressed as a function of intrinsic contact angle (θ_0) and other parameters (Bhushan, 2002).

$$F = 2\pi R\gamma(1+\cos\theta_0)$$

Equation 6.1-1

where *R* is the radius of the tip/particle and γ is the surface energy (0.0728 Jm^{-2} for water) of the liquid film. The predicted force of adhesion for the hydrophilic AFM tip interacting with the hydrophilic silica surface is 8-20 nN which is in reasonable agreement with the measured value of ca. 18 nN seen in Figure 6.1-1. The value calculated from Equation 6.1-1 above for the 30 μm spheres yielded a much larger adhesive force (1 μN) than that was experimentally determined (ca. 380 nN). The discrepancy can be explained due to the particles having surface roughness on the nano-scale, as observed by AFM imaging (Figure 3.1-5), contact with the flat surface is made via a number of contact points, i.e., in a multi-asperity regime, each contact point with radii of curvature in the nano-range.

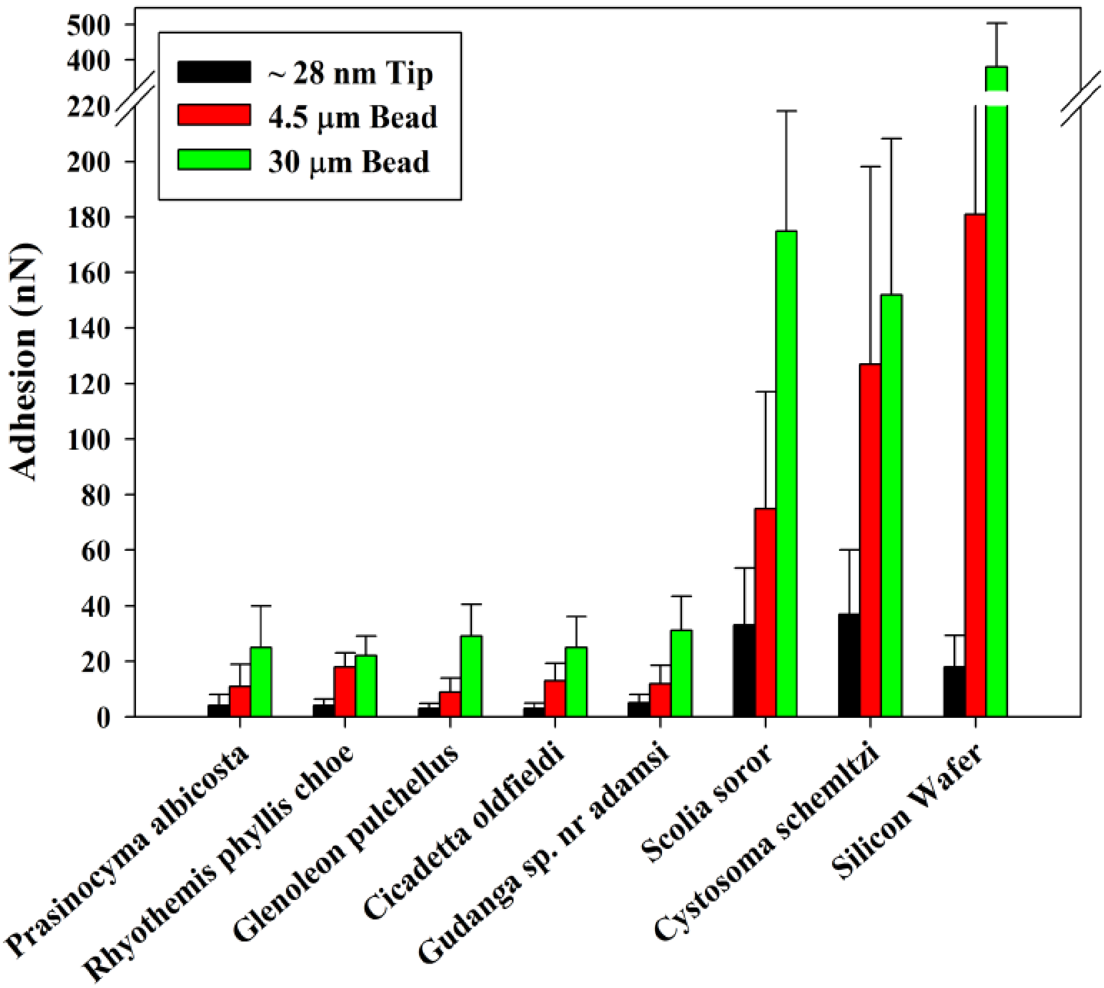

Figure 6.1-1. Graph displaying the adhesion with the silica particles on the hydrophilic and super/hydrophobic insect wing surfaces. Error bars represent standard errors.

The adhesion between the silica tip/microsphere and the insect cuticles represents a high surface energy contaminant particle coming into contact with low energy hydrophobic and higher energy hydrophilic micro/nano-structures/arrays. This is highlighted in Figure 6.1-1 showing the differences in adhesion and wetting between the two groups of insect structuring. Particle adhesion on the (super) hydrophobic insect cuticles was much lower in comparison with that on the flat hydrophilic Si surface and hydrophilic insect species. The higher adhesion values measured between the contacting surfaces of the hydrophilic insect membranes and the hydrophilic contaminants reflects the menisci formation from liquid present on the surfaces. As well, the relatively flattened and broadened structures of the hydrophilic insect cuticles do not minimise the contact area to the degree of the hydrophobic species.

The larger the particle contacts (e.g., compare Silica AFM tip (ca. 28 nm) with 4.5 µm and 30 µm in diameter sphere Figure 6.1-1) the higher adhesion is. This reflects the increase in radius of curvature and increased contact points. Thus the real contact area increases along with the meniscus contributions.

Adhesion was also measured for the 30 µm silica sphere in diameter on a poly (tetrafluoroethylene (PTFE) surface (contact angle 108°) with a measured value of ~50 nN. Thus the adhesion values for the super/hydrophobic insect cuticle membranes (Figure 6.1-1) represent lower surface energy materials than the flat PTFE for interaction of particles at this length scale. Based on the Young's equation, the surface energy of the cicada membrane is ~12 $mJ\cdot m^{-2}$. For comparison, the work of adhesion for water on a silica (glass) surface is ~120 mJm^{-2}(Sklodowska et al., 1999). It is evident that the topography of the hydrophobic wing membranes results in minimal actual contact area between the touching surfaces. The highly intricate hydrophobic patterning decreases the contact area, number of menisci, van de Waals attraction and thus the total adhesive force.

AFM manipulation of the cicada wing membrane (by contact imaging with an AFM probe with a tip with a large radius of curvature (>150 nm)) resulted in partial crushing of the array structures. The crushed array presented a flatter surface and thus a greater contact area for adhering particles in comparison with the intact array, thus leading to greater adhesion. For example the 30 µm sphere showed an adhesion almost twice that of the intact membrane (~45 nN – similar adhesional value to that of the PTFE surface). An AFM silica tip with a radius of curvature of ~14 nm was also used to measure adhesion on the crushed membrane. This showed the same adhesion (±0.3 nN) as the intact cicada membrane. This shows that for particles with radius of the curvatures smaller than that of the membrane surface protrusions the contacting areas between particles, whether with intact or flattened membranes, are similar. Thus the size of the particle (silica tip) determines the adhesion and the chemistry of the crushed regions do not significantly alter from intact membranes (significant chemical changes would most likely manifest in greater differences in adhesion).

Adhesion of the C_{18} particles with the insect cuticles was generally lower than the comparably sized silica particles (Figure 6.1-2 (A)). This represents the difference in adhesion of a hydrophobic and hydrophilic particle coming into contact with the insect wing membranes. As well the differences in roughness may also contribute to this effect (Figure 6.1-2 (B)).

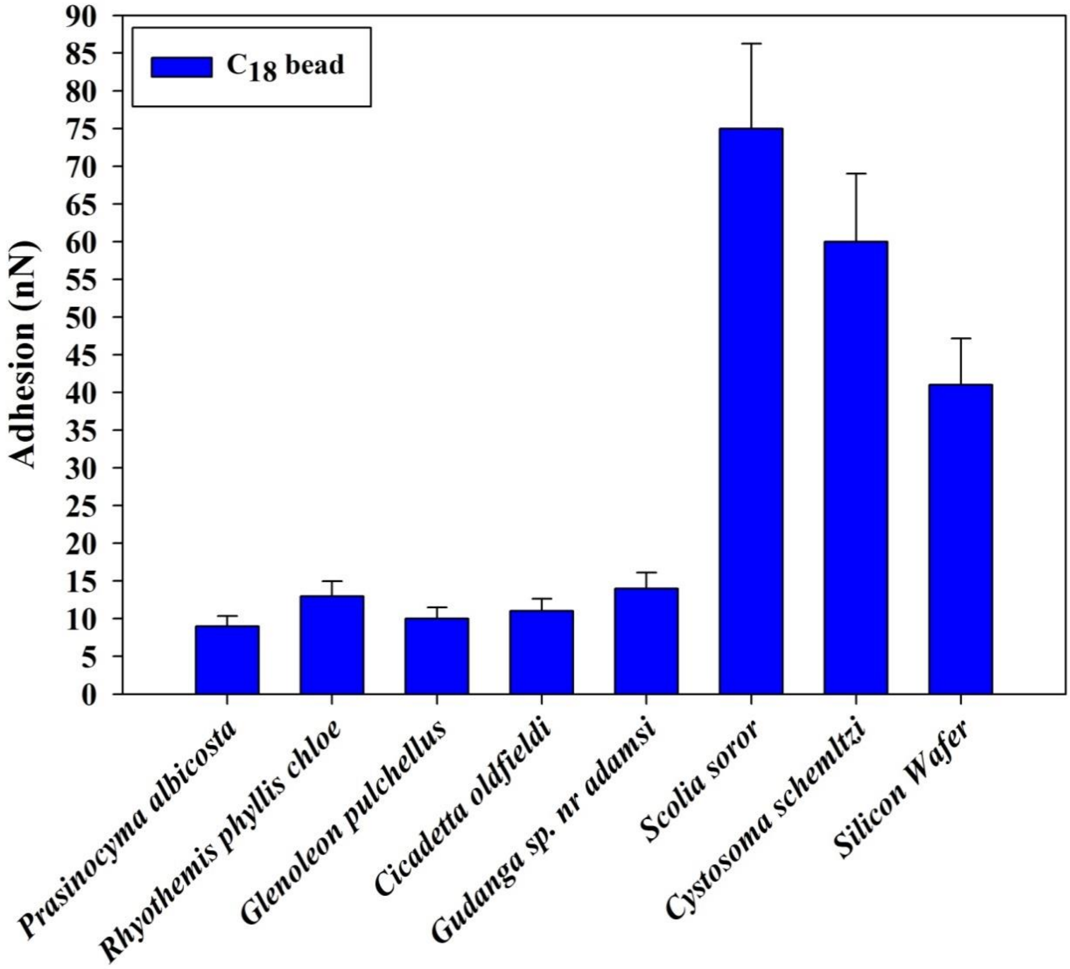

Figure 6.1-2 (A). Graph displaying the adhesion with the C18 particles on the hydrophilic and super/hydrophobic insect wing surfaces. Error bars represent standard errors.

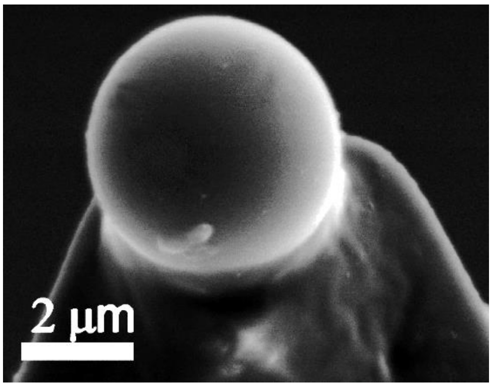

Figure 6.1-3 (B). SEM image of a C18 bead attached to a cantilever. The section closest to the cantilever tip is contaminated with epoxy and does not interact with the sample.

The contact of contaminant particles with the wing membrane surface of *Cicadetta oldfieldi* shows ultra-low adhesion forces as small as 3 nN for AFM tip sized spherical bodies (ca. 28 nm diameter) and less than 30 nN for 30 μm sized silica particles.

The adhesion values measured on the dragonfly (*Rhyothemis phyllis chloe*) cuticle for the 30 μm sized silica particle was the lowest of all the insects (Figure 6.1-1). The open structure framework of the membrane minimises the contact points and thus the adhesion. F-D curves on the moth surface interacting with larger particle sizes often showed multiple releases during the retract section of the force curve (e.g., Figure 6.1-3). This type of F-D curve, showing multiple release (and thus adhesion) points, is in stark contrast to the other insect surfaces where adhesion was generally characterised by a single release mechanism (with the exception of *Pimelea linifolia* ssp. where the release from multiple contacts from the pollen sometimes occurred). Release of the particles from the rough scale surface may be the result of the detachment of the varying pollen protuberance contact points with the scale roughness making multiple adhesional points between the two surfaces.

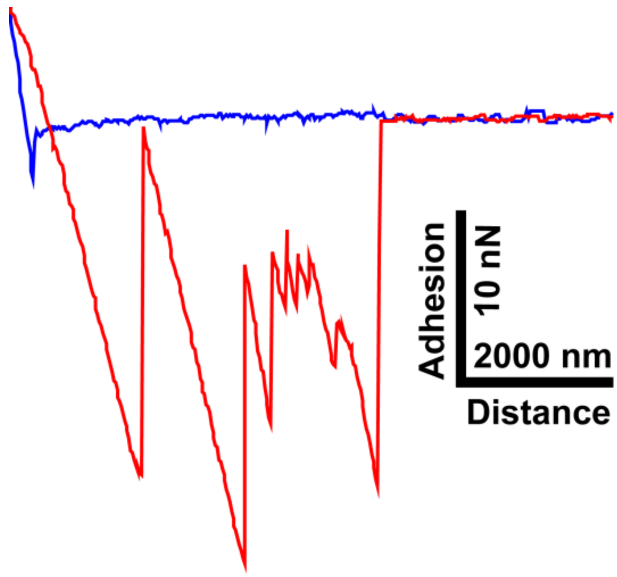

Figure 6.1-4. A single representative F-D curve showing multiple 'jumps' on the retract curve (red) obtained on the moth wing (*Prasinocyma albicosta*). The approach curve (blue) shows a distinct snap-on feature (and a general downward trend) where the Si bead is presumably statically attracted to the surface of the moth scales (since the bead is the object being brought into contact with the surface).

However, butterfly and moth scales are known to fully detach from the wing. This attribute can serve as a defence mechanism upon contact with other surfaces (e.g., spider web). The multiple release steps, as indicated by the F-D curves, may also suggest a number of possible mechanisms of detachment between the particle and scale:

1) The overlapping scale morphology (Figure 6.1-4) provides a ratchet-type release in sequential steps.

2) The pedicel attached to the scale releases in steps from the socket.

3) The scale is compressed upon contact and follows the particle upon retraction.

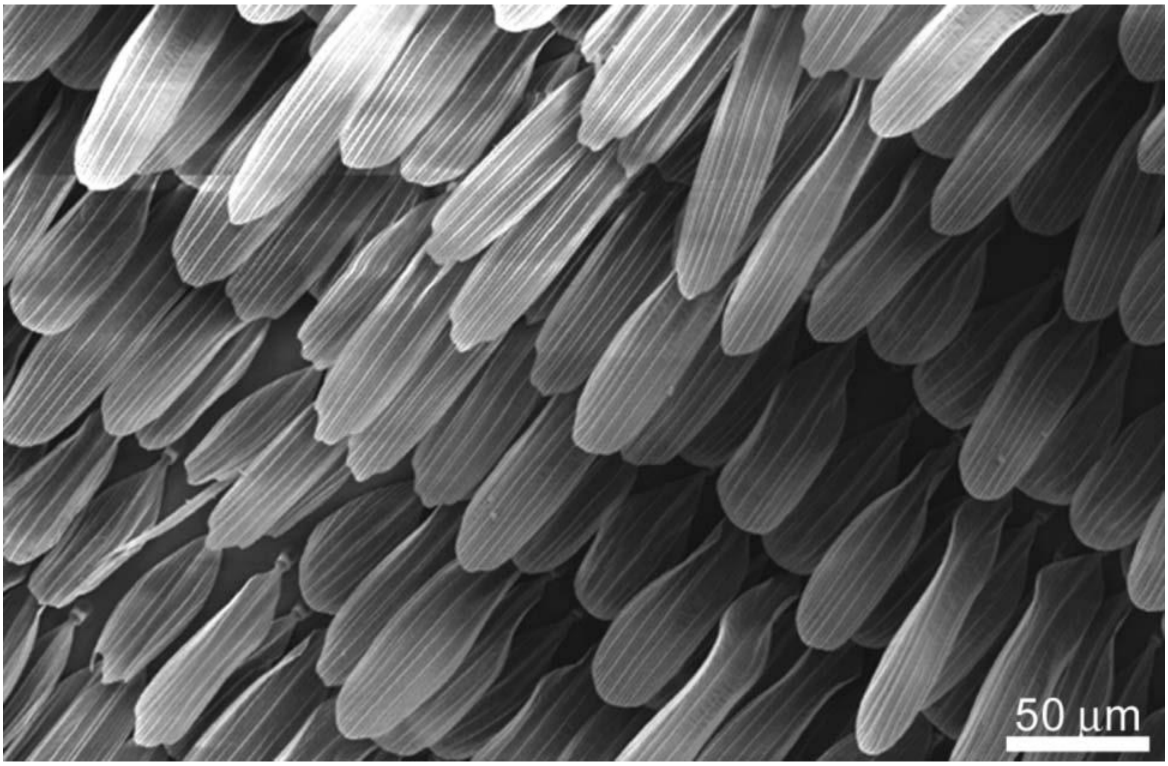

Figure 6.1-5. The overlapping scale arrangement of the *Prasinocyma albicosta* moth wing.

The sequential release mechanism of the scales may also indicate a unique way upon which these type of insects contend with small contact adhesion without full detachment of the scale occurring.

The pollen grains are of a similar scale to the 30 µm silicon beads. However due to the rougher morphology and more hydrophobic nature of the long chain polymers that pollen sporopollenin (outer layer) compose of, the adhesion between the pollens and the insect cuticles is lower (Figure 6.1-5). Figure 6.1-5 shows that the spherical shaped profile with small asperities of the *Pimelea linifolia* ssp. pollen exhibited the lowest adhesion. Thus the reduced contacting area resulted in lower adhesion. The *Acacia fimbriata* pollen demonstrated similar adhesion values to the pyramidal shaped *Grevillea* pollen.

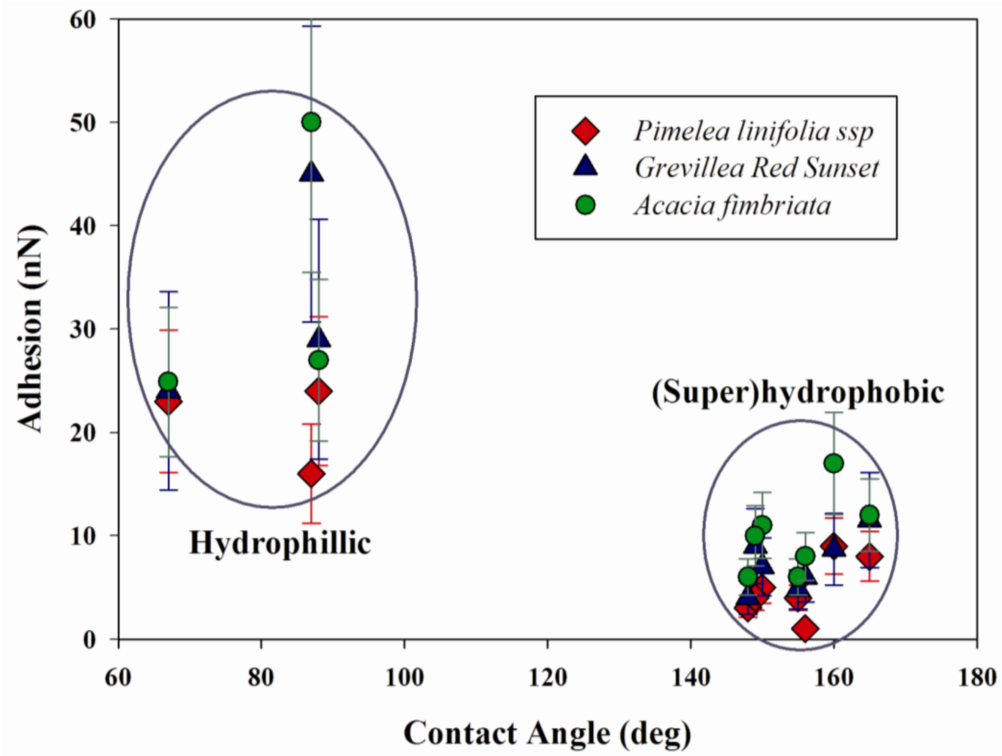

Figure 6.1-6. Graph displaying the contact angle and adhesion with the three different pollen particles - *Pimelea linifolia* ssp., *Grevillea* 'Red Sunset' and *Acacia fimbriata* 'Golden wattle'. Error bars represent standard errors.

The measured highest adhesion between hydrophilic insect membranes and the pollens was 50 nN. These high values were also reflected in the frequency of contaminate particles as viewed from freshly caught specimens using optical and SEM imaging (Figure 6.1-6). Pollen grains were also interacted with an Australian stingless native bee (*Trigona carbonaria*) pollen basket located on the hind leg. Adhesion values of pollens on this region were up to 70 nN. This value is of a similar order to adhesion measurements of pollens to stigma cells (in the order of 10^{-7} N)(Zinkl et al., 1999).

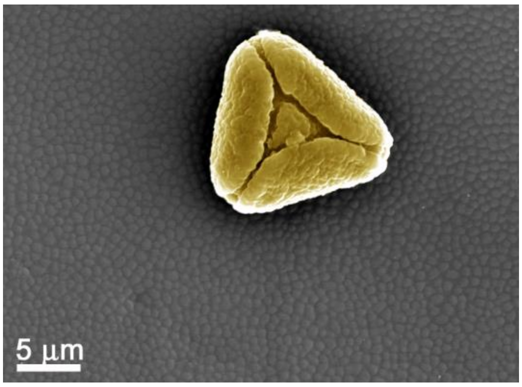

Figure 6.1-7. A pollen grain found on the wing membrane of the hydrophilic flower wasp, *Scolia soror*.

Frictional forces were also measured on three insect species (*Cicadetta oldfieldi*, *Scolia soror* and *Cystosoma schemltzi*) with a silica tip at loading forces represented by the adhesional force. The frictional force obtained on the insect cuticle of the cicada was 5.5 $\pm$ 2.5 nN. This value demonstrates that only very low frictional forces are required to remove contaminants of this size from the cicada membrane. In contrast to the frictional force on the cicada, the flower wasp and bladder cicada yielded values of 47 $\pm$ 15 nN and 65 $\pm$ 15 nN, respectively. This demonstrates the higher forces required to remove particles which are more strongly attached to the membrane.

6.2 CHAPTER SUMMARY

The tribological properties on insect cuticles were measured by the interaction of single spherical surfaces (of different size and chemistry that mimics natural contaminants) and also natural contaminants such as pollens. Adhesion is contributed by the chemical and topographical components of the surfaces. Adhesion values experienced on insect cuticles by the pollens used in this thesis are typically in the magnitude of tens of nanonewtons. Low adhesive surfaces also display low friction and low wettability.

7 NON-WETTING WINGS AND LEGS OF THE CRANEFLY AIDED BY FINE STRUCTURES OF THE CUTICLE

7.1 INTRODUCTION

One of the more interesting insect groups is terrestrial and aquatic species whose surfaces are very rough or covered with hair piles. They have very high advancing and receding CAs; often over 150°. These adaptations are more often than not structural rather than chemical since many insects already have chemistry which is at the near upper limit for smooth surfaces. Hair piles on terrestrial insects may aid to contend with the risks associated with living in an environment which offers little protection against wetting by rain and other water surfaces the insect may encounter (Watson et al., 2010a, Watson et al., 2010b). As with other insect cuticular structures, hairs may serve multi-functional purposes such as aiding in flight (contributing to aerodynamic factors) (Perez-Goodwyn, 2009).

One of the many insects which demonstrate a hierarchy of surface roughness is the cranefly: one of the most abundant species of all the Diptera. As the craneflies are notable lovers of moisture, they inhabit a diverse range of habitats where water is available and are typically found resting on foliage, overhanging water sources in damp shady locations. The larvae mainly emerge from water or semi-liquid matter (e.g., mud) to become adults, and most species cease to feed after this stage. The adults exhibit a slender body and extremely long legs with their wings spanning from 8 to 75 mm and characterized by having two anal veins reaching the margin. The adults fly slowly and irregularly close to moist grounds with legs making regular contact with the substrate.

As the cranefly has exceptionally long legs and is often found in damp environments the insect will be susceptible to detrimental adhesional contacts, as well as breakage in the worst case scenario. The insect can potentially become a victim of permanent immobilization on water or wetted surfaces with a reduced capacity to evade or fight off predators. This chapter deals with how the fine structure of cranefly (*Nephrotoma* *australasiae*) hairs on the legs enhances the ability to repel water, with smaller hairs found on the wings aiding the insect under rain/droplet conditions.

7.2 RESULTS AND DISCUSSION

A photograph of the cranefly (*Nephrotoma australasiae*) studied here is shown in Figure 7.2-1(A) and (B). The cranefly at rest demonstrates an apparent large contact area with the underlying substrate (e.g., leaves, wetted soils) due to the extremely long legs.

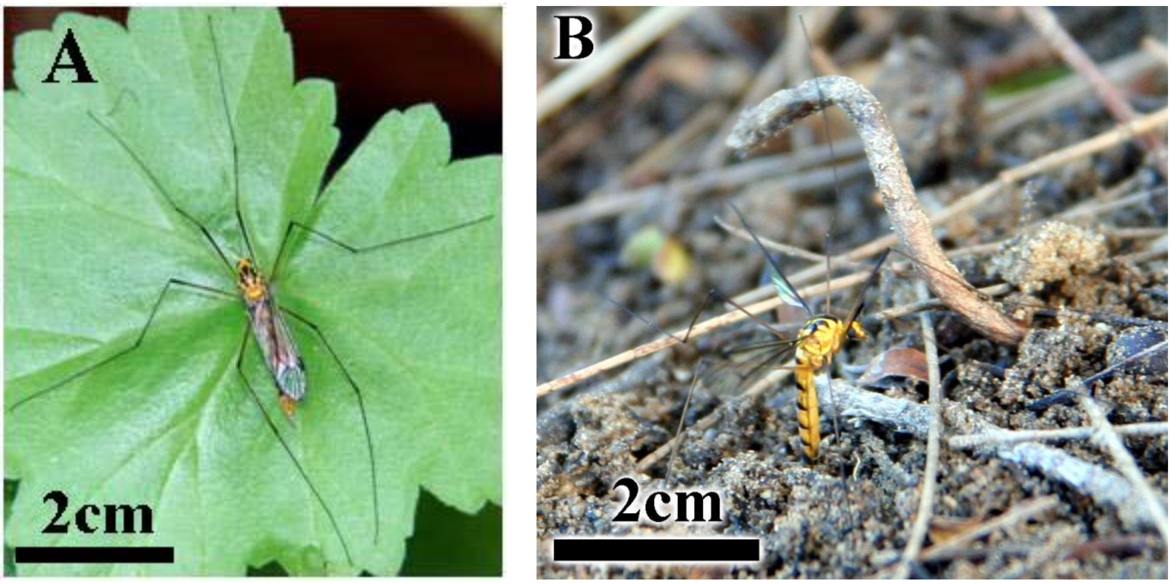

Figure 7.2-1. (A) Resting cranefly (*Nephrotoma australasiae*) with a large apparent contact area with the underlying leaf due to the extremely long legs. (B) An ovipositing cranefly at the bottom of the up-down flying pattern on moist/muddy soil showing legs and the tip of the abdomen in contact with the underlying substrate pointing.

Some of the specimens used in study were collected along the edges of a freshwater river. Observation of the flying habits of these insects (12 insects in total) showed a bouncing motion across the substrate (leaf litter and moist muddy soil). This bouncing comprised of a near vertical accent of 3 to 8 cm and then a downward motion where the insect legs came into contact with the ground. The duration of the up-down cycle is typically around 0.3 seconds (3.3 Hz). The observed flying behaviour is demonstrated by ovipositing craneflies where the tip of their abdomens frequently contact the substrate (White, 1951) as demonstrated in Figure 7.2-1(B). The impacting force with the ground of the legs appeared relatively large, which could be the result of the long legs used as springs to control the impact with the ground and/or possibly help propel the insect on the vertical ascent part of the cycle. As the flying motion necessitates leg contact with moist ground, it would seem advantageous for the leg to feature structural patterning to aid in repelling water and contaminants.

Interaction of the cranefly leg and wing with water of various length scales is shown in Figure 7.2-2. The hair piles in all circumstances result in an initial contact where the droplets attain a near spherical shape. The water droplet exhibits a CA of over 170° with the wing as shown in Figure 7.2-2(A). The apparent CA of a water droplet supported by a syringe tip and placed on the cranefly leg is also extremely high in Figure 7.2-2(B). Micro droplets from a mist spray exhibit similar CAs on both wing and leg surfaces. in Figure 7.2-2(C), (D), (E) show droplets being held up by hairs on the wing vein, wing membrane and leg, respectively. The images demonstrate the apparent superhydrophobic nature of the cuticles causing water droplets to spontaneously roll off the cuticle surfaces.

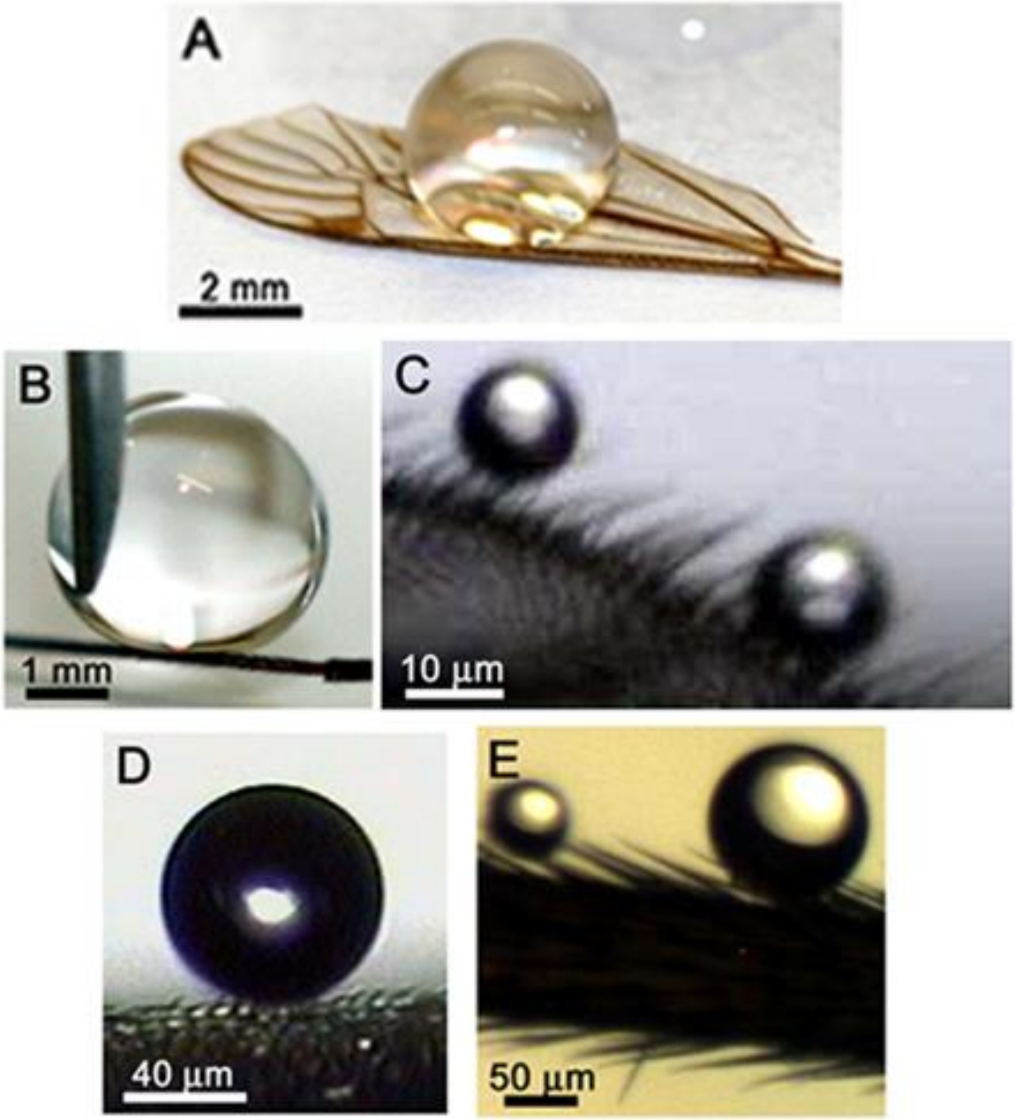

Figure 7.2-2. Optical images showing a 10 μL water droplet displaying superhydrophobic contact on a cranefly (A) wing and (B) leg with the water droplet supported by a syringe to avoid roll off. Micro-sized water droplets from mist sprayer supported by hairs and air underneath and showing superhydrophobicity on the microscale on cranefly (C) wing veins, (D) wing membrane and (E) leg.

A Scanning Electron Microscope (SEM) image of a small region along the cranefly leg is shown in Figure 7.2-3(A) where four types of hair exist (types a, b, c and d). Hair type 'a', the most protruding hair is 90 ± 15 μm in length and angled at 25 ± 5° from the inner leg shaft surface. Their tilt arrangement is similar to the hairs observed on water striders leg which need to maintain function above the surface of the water (Watson et al., 2010). However the length and width of type ‘a’ hairs on the cranefly leg are typically three times larger than those reported on striders (Watson et al., 2010).

A low magnification SEM image (in Figure 7.2-3(B) shows the majority of the wing is covered with a uniform array of small hairs (type ‘f’) where the average length and spacing of the hairs on the membrane are 12 ± 1.5μm and 14 ± 2 μm, respectively (in Figure 7.2-3(C)). The larger hairs (type ‘e’) found on the wing veins are comparable to the longest hair type ‘a’ on the legs.

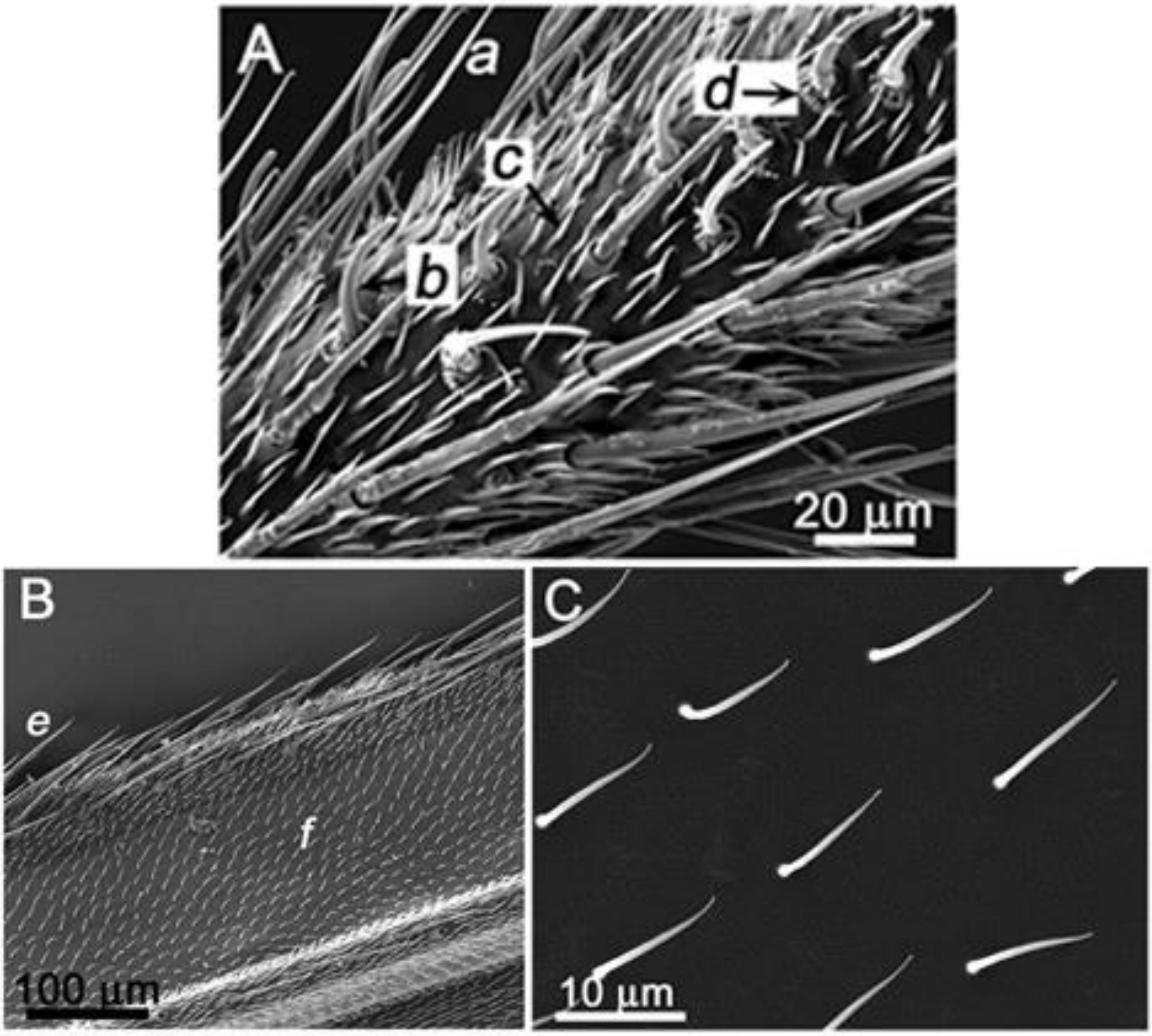

Figure 7.2-3. (A) SEM image of a cranefly leg with four different types of hair (types a, b, c, d) with nanogrooves visible on hair types a, b and c. (B) SEM image of different size hairs (types e and f) on a cranefly wing (with longer hairs ‘e’ on the wing edge and the veins). (C) SEM image of cranefly wing showing type ‘f’ hairs in high magnification.

The finer structures of cranefly hairs are shown in Figure 7.2-4(A) and (B). Small type 'e' hairs on the wing (Figure 7.2-4(A)) have arrow-like grooves that are similar in appearance to the hairs found on water strider legs (Watson et al., 2010). Type 'a' hairs on the legs (Figure 7.2-4(B)) have a micro/nano architecture consisting of a number of ridges (around 500 nm deep) running along the hair shaft while ultra-fine channels run diagonally and meet at the apex and base of the large grooves.

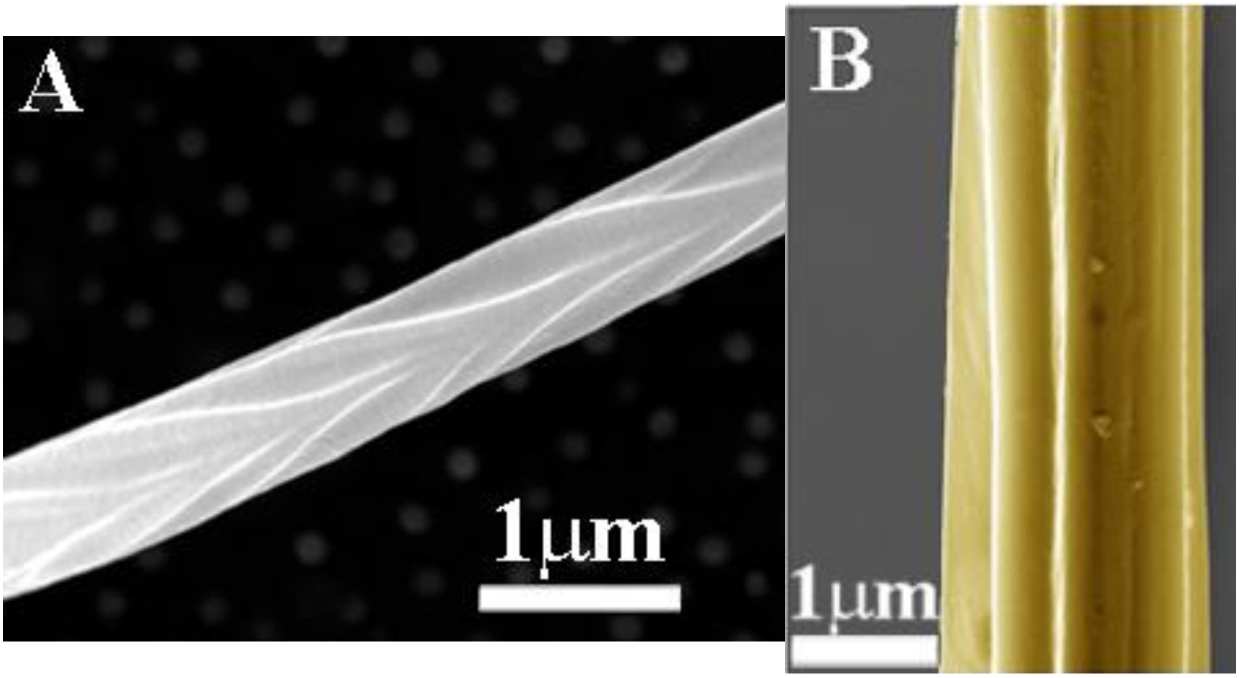

Figure 7.2-4. SEM image of (A) the fine surface structure found on a small wing hair and (B) leg hair of the cranefly, which show grooves with ultra-fine channels at about 45° which meet at the top and bottom of the larger grooves.

To investigate whether the architecture (i.e., the grooves) aided in a hair's ability to resist water penetration, individual type 'a' hair were coated with PDMS to maintain the chemical contribution to the process Figure 7.2-5.

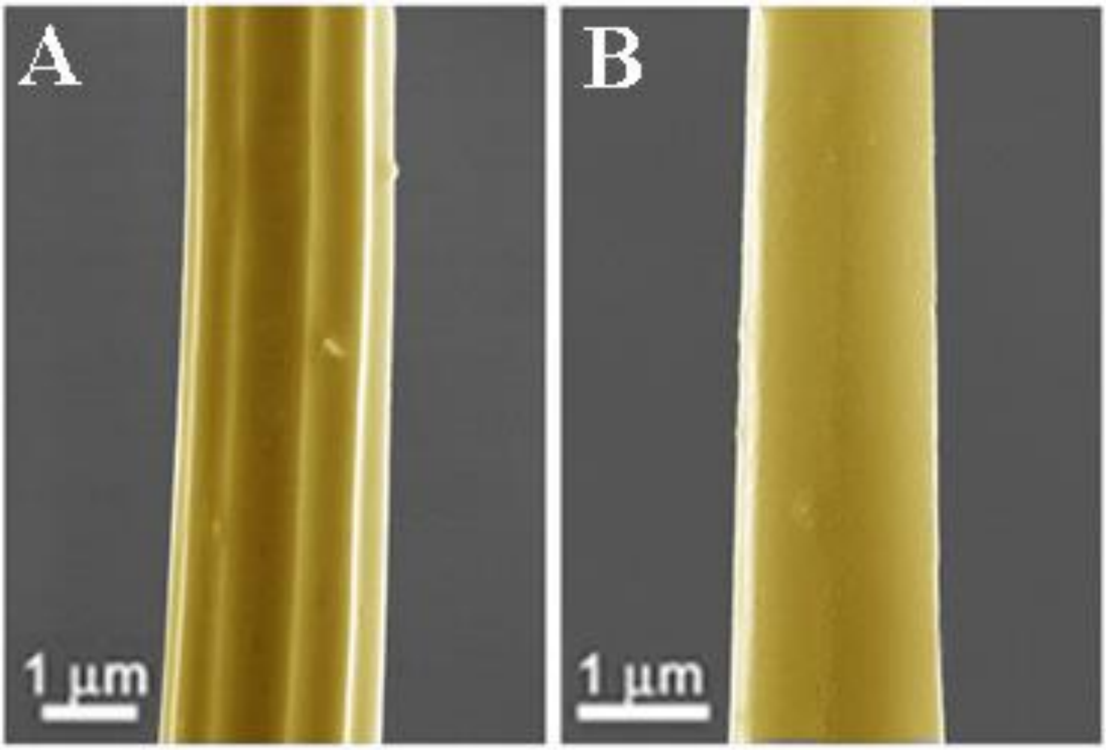

Figure 7.2-5. The hairs which were covered with (A) a thin coating of PDMS still retained a significant amount of the topographical structure (grooves) and (B) a thick coating completely removing the grooves.

The interaction of individual hairs (uncoated and coated) with water droplets is shown in Figure 7.2-6(A) – (D). Figure 7.2-6(A) shows a cranefly leg floating on water with the hairs on the side of the leg dimpling the surface (highlighted by the arrows). Uncoated hairs attached to AFM cantilevers were brought into contact with a water droplet with loading forces of up to 1.26 µN and was unable to penetrate the surface (Figure 3.1-7). Figure 7.2-6(B) shows the dimple on the droplet surface between points *i* and *ii* created by the contacting uncoated hair. However the water surface became penetrable when effects from both types of groove structures were removed by a thick PDMS coating (Figure 7.2-6(D)). A thinner coat of PDMS completely covering the hair surface but without filling the deeper grooves was also unable to penetrate the water surface (Figure 7.2-6(C)).

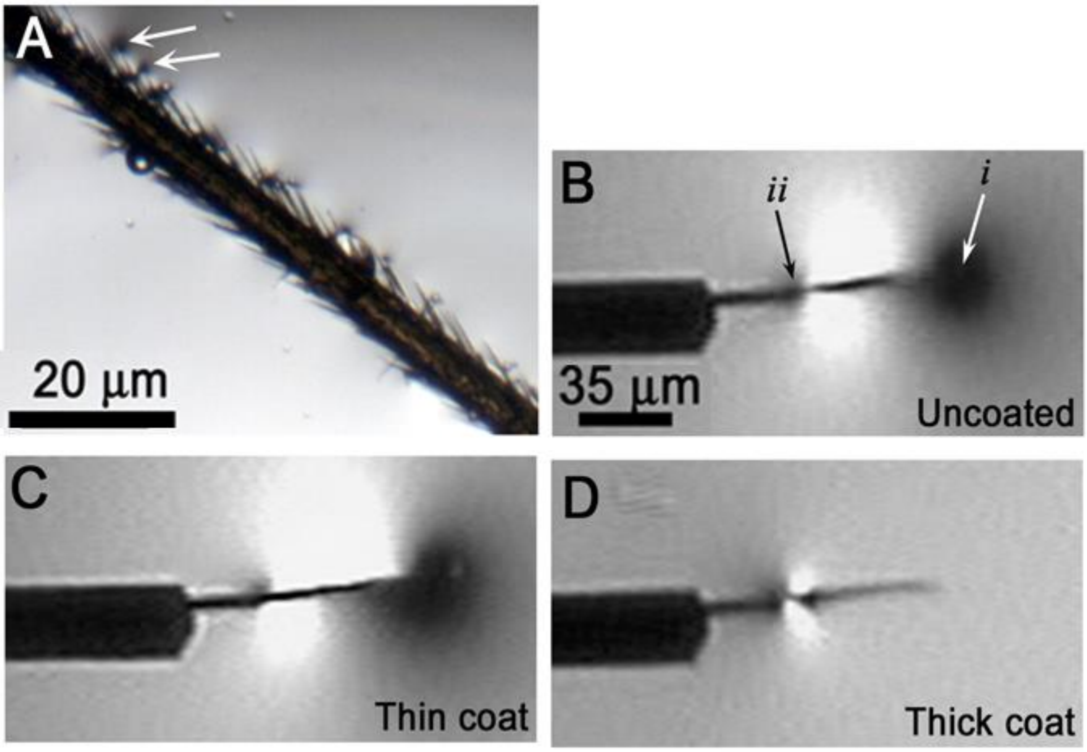

Figure 7.2-6. Optical images showing (A) cranefly hairs on the side of the leg dimpling the water surface (highlighted by arrows). Interaction of individual cranefly hair (type 'a') with water. (B) An uncoated hair not penetrating the water surface as observed by the formation of a dimple on the droplet surface from points *i* to *ii*. (C) A thinly coated hair also dimpling the water surface. (D) A thick coated hair penetrated the droplet surface.

AFM adhesion measurements were carried out on uncoated and coated hairs interacting with water. The results showed that uncoated and thin-coated hairs yielded similar adhesion values (17.9 ± 4.3, 35.6 ± 6.2 nN, respectively) suggesting that the deeper grooves were still prominent with a thin coating (Figure 7.2-5(B)). The adhesion of the thick coated hair (the width of which was still similar to the uncoated hair) with water became more than ten times larger than that without the surface structures (in excess of 500 nN) this highlights the significant role of the hairs' nanoroughness in both reducing adhesion and resisting water penetration.

The results from interacting individually coated and uncoated hairs with droplets shed light on the importance of the micro/nano structuring in repelling water from the wing surface. The hairs which were covered with a thin coating of PDMS still retained a significant amount of the topographical structure (grooves) as seen in the SEM images in (Figure 7.2-5(A)).

These 'thin coated' hairs, like the uncoated hairs, did not penetrate the water surface under load. 'Thick' coated hairs where the topographical structure components were reduced or completely removed (Figure 7.2-6(C)) resulting in a much smoother coating did however penetrate the water surface. Moreover, the spring constants of the coated hairs did not alter enough to account for hair penetration (see Section 2.1.1.2 for method of determining spring constant). This indicates that the micro/nano roughness consisting of the open architecture of ridges with grooves is responsible for this effect as the chemistry is maintained (for thin and thick coats) and only the topographical component was being altered. The much finer grooves did not appear to significantly contribute to the resistance of water penetration as these were removed by a thin coating. The higher adhesion values measured on thick coated hairs in comparison to thinly coated samples also support findings that the larger groove structure is the important feature in minimizing contact with the water body.

An ideal architecturally enhanced non-wetting surface has the maximum ability to withstand water intrusion while allowing the liquid to have maximum mobility on the surface (with high CA and low CA hysteresis). However a trade-off exists between enhancing the two properties when using only one layer of architecture (Bush et al., 2007, Extrand, 2006).

In order to maintain high hydrophobicity and buoyancy, air needs to remain within the asperities underneath the liquid body. Dense asperities are less likely to be protruded by water and are found on the legs of the fast swimmers like the water strider (Bush et al., 2007). The legs have a high f_1 that pins the solid-liquid-air contact line requiring high pressure to drive out the air.

Unlike the water striders (Wei et al., 2009), the craneflies do not experience high hydrodynamic pressure from its leg strokes and thus may not require a dense type 'a' hair layer (Figure 7.2-3 (A)) (Lafuma and Quere, 2003). It may be desirable for the most protruding hair layer (type 'a') of the cranefly legs to be less dense (up to 10 times more sparse) than the water strider to increase droplet mobility. More rigid hairs (spring constant twice as high) are also more desirable in order to resist surface tension drawing the long hairs (~ 3 times longer) together (Perez-Goodwyn, 2009).

Despite being longer and thicker, the adhesion of the hairs of the cranefly legs are similar to the water strider (Watson et al., 2010); both being greatly reduced by their surface grooves. The micro-grooves not only contain more air to increase buoyancy and hydrophobicity, they also reduce the adhesion to water and to other undesirable surfaces as well as providing structural rigidity without the additional weight and material.

The four types of hairs (Figure 7.2-3 (A)) with different structure and dimensions may play different roles for the insect functioning. Many insects have multiple layers of features on their cuticles that combine to prevent wetting by water bodies of different length scales (Andersen and Cheng, 2005, Watson et al., 2010a, Watson et al., 2008c). As shown in Figure 7.2-3 it is the long hairs (type 'a') on the legs which will first come into contact with water bodies as they extend beyond the smaller hair piles. Loading pressure from a large water body causes the taller hairs to collapse towards the shorter hair layers until the loading force is balanced by the combined stiffness from all the contacting hairs. The thick shorter hairs have a curvature that aligns the top half of the hair with the free surface forming a more efficient air-trap (Cheng, 1973). The multi-layer hair is a feature in other semi-aquatic insects where an air plastron for submergence is required (Perez-Goodwyn, 2009). Type 'c' and 'd' hairs may also contribute to functions other than anti-wetting due to the small hair lengths (e.g., sensory (Perez-Goodwyn, 2009)).

Small water droplets that fall between the long hairs (type 'a' and 'b') can be prevented in contacting the underlying membrane by the shorter hairs beneath (type 'c' and 'd'). The mobility of droplets (mist or other smaller droplets) generally increases as they coalesce with a corresponding increase in mass. Some smaller droplets may also become absorbed by larger droplets from above which will then roll off (Watson et al., 2010a, Watson et al., 2010b).

The hairs on the legs of the cranefly and water strider have a very similar tilted arrangement and the alignment of the hair grooves. Anisotropic wetting is reported on the water strider leg as the water contact line has higher mobility when advancing toward the tip of the leg (Andersen and Cheng, 2005). A similar wetting action may be possible on the cranefly with the finer diagonal grooves further enhancing anisotropic mobility. Also, the similarity between the fine structure of the cranefly, smaller wing hairs and water strider leg hairs

(Watson et al., 2010) suggests that droplets may roll off more easily along the direction of the patterning.

7.3 CHAPTER SUMMARY

Enhanced by various hair arrangements and their grooves, the low adhesive and wetting properties of the cranefly cuticle allow the insect to interact with a variety of environmental surfaces and conditions where the insect can be immobilized. These findings may contribute to the next generation of bio-inspired materials and devices for the control of interactions at solid–liquid interfaces on macro- and micro-/nano-scales (e.g., the next generation of bio-inspired materials, the design of future robotic insects where weight constraints and surface feature durability are important considerations). Our results support an earlier hypothesis that suggested structures on this length scale (micro-/nano-grooves) found on water striders can resist water adhesion.

8 SURFACE MICRO-STRUCTURE FLEXIBILITY: ADVANTAGEOUS FOR LACEWING CUTICLES REQUIRING WATERING REPELLING MECHANISMS

8.1 INTRODUCTION

Understanding the relationship between the structure dimensions and the corresponding functional mechanisms at the micro/nanoscale range is essential for creating the next generation of functional surfaces. In a variety of industrial applications and future technologies, controlling the adhesion between solid-solid and solid-liquid contacts for example is important. As mentioned previously in Chapter 1, insects with large wing surface areas are the most vulnerable to contamination where water and/or solids may potentially impede flight or immobilise the organism. Many of these insects have adopted hydrophobic structuring on their wings also resulting in ultra-low adhesive surfaces. For example, on cuticles of the primitive mayfly and stonefly subimagoes are small hairs which help them to emerge from water. Interestingly, these mayfly hairs are not present on their subimagoes that emerge from land (Vukusic and Sambles, 2003, Watson et al., 2008a)

Living in an environment with little protection against rain and other wetted surfaces the lacewings with a large SM are good candidates for suffering detrimental effects from contacts with contaminant particles or water. Adult lacewings have superhydrophobic wings arising from a combination of low surface energy chemistry and a number of structural features that reduce surface area contact. The dense netting (Figure 4.2-1(K)) and wax crystals cover the membrane and the combined surface roughness minimise the solid-liquid contact area by allowing air in topographically favoured regions such as troughs and surface depressions leading to a superhydrophobic CA. The nanostructures are also on the hairs which significantly lower their adhesiveness and wettability (Watson et al., 2010b).

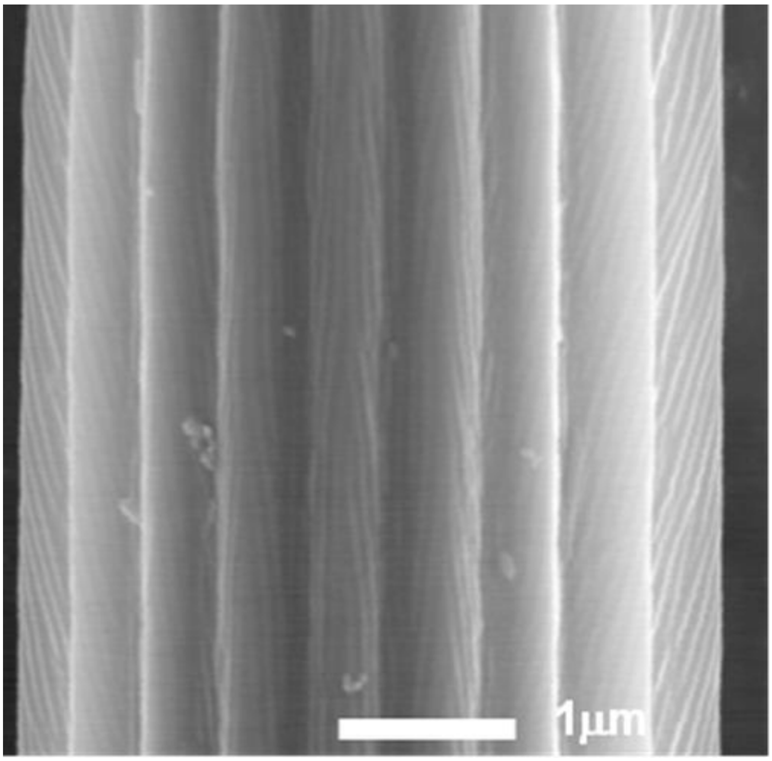

Figure 8.1-1. SEM image of the fine surface structure found on a hair with grooves and ultra-fine channels at about 45° which meet at the top and bottom of the larger grooves.

Similar to cranefly hairs, the hairs on the lacewing wings are the first line of defence against contact with undesirable (solid or liquid (Bormashenko, 2008)) surfaces. This is true for surfaces of all bodies that are larger than the hair lengths and spacings (i.e., the hairs reduce contact against surfaces from bulk bodies to particles in the millimetre scale) and could hinder the insect's mobility. The hairs may also serve to protect the underlying hydrophobic wing membrane structuring.

Hairs on insect surfaces have been reported to also serve aerodynamic functions (Watson et al., 2010b). The downside is they also provide more surfaces for the attachment of sub millimetre particles that they are not designed to contend against. In small amounts these smaller solid or liquid contaminants that are able to contact the wing membrane in between the hair spacings are not likely to significantly weigh down and hinder the insect's mobility. Moreover, they are likely to be dislodged by the mechanical forces during insect flight.

8.2 RESULTS AND DISCUSSIONS

The wing surface of the adult *Nymphes myrmeleonides* when viewed with a compound microscope (Figure 8.2-1) shows the venation on the lacewing that divides the membrane into cells which become more elongated towards the tip. Along the veins, the hair spacings range from 0.12 to 0.05 mm while the width of the cells (the hair spacing across the cell) range from 0.05 to 12 mm. In the tip region of the wings, the hairs are more tightly spaced along the veins (around three times) and the cells are more elongated with a higher ratio of perimeter to surface area. The hair lengths are consistently ca. 150 μm throughout the whole wing. Their incline angles generally range from 30° to 60° away from the plane of the wing and up to 90° away from the veins (viewing from the top). The tilt arrangement is similar to the hairs observed on the craneflies (Chapter 7) and water striders which are needed to maintain function above the surface of the water (Watson et al., 2010) and provide the wing surface's directional wetting property. The hairs on the lacewing have been described in a recent paper (Watson et al., 2010b) and like the hairs on the cranefly they have a nano-structuring (grooves) along the shaft (Figure 8.1-1).

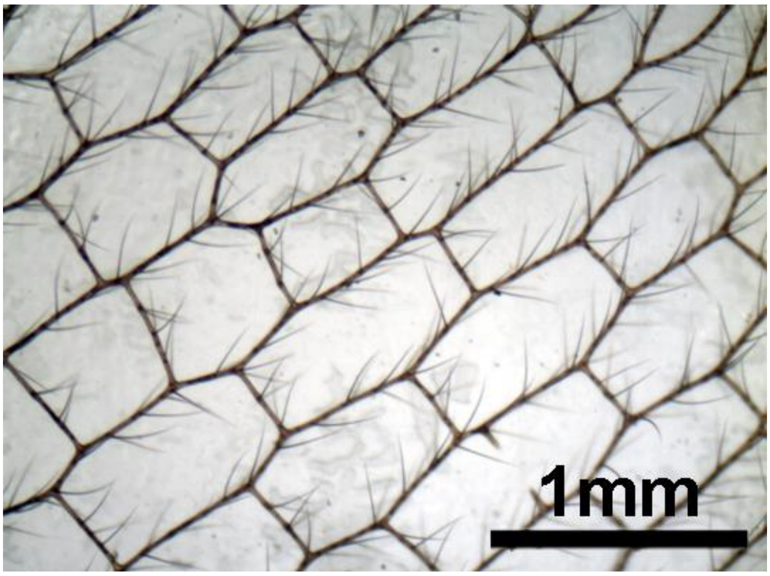

Figure 8.2-1. Cells at the tip region which are more elongated and showing higher hair density than the base region (see Figure 8.2-2 for comparison). Hairs generally inclining towards the tip of the wing (right hand side of the image).

Water drops on the cuticle surface generally fall under two types. The first type were those with low mobility (referred to as 'Wdrops' in the text) which include most mist drops and other larger drops that have high solid-liquid contacts with the wing. The second type (referred to as 'Cdrops' in the text) are drops with high mobility that are difficult to place with a pipette on a wing sample laid flat. Cdrops are generally much larger and are supported on the tip of the hairs making little or no contact with the underlying membrane underneath.

In order to investigate the efficiency of contaminant removal of the wing, the surface was exposed to two different types of water droplets (large droplets and mist) when the surface was seeded with two types of contaminant particles (Figure 8.2-2). Silica beads (KOBO MSS-500/20N) ranging from 8 to 64 μm (average 20.84 μm) in diameter were dispersed using a polyethylene pipette (Livingstone PTP03) onto the wing with a density between 40-170/mm^2 (Figure 8.2-2(A)). Poly[methyl methacrylate] (PMMA) beads (Bangs Laboratories, Inc. BB03N/5436) were dispersed similarly with a density between 6~90/mm^2 (Figure 8.2-2(B)). The PMMA beads were ~83 $\pm$7 μm in diameter to mimic larger contaminants. Both Si and PMMA beads are hydrophilic and will adhere to water due to the strong capillary force once they come into contact.

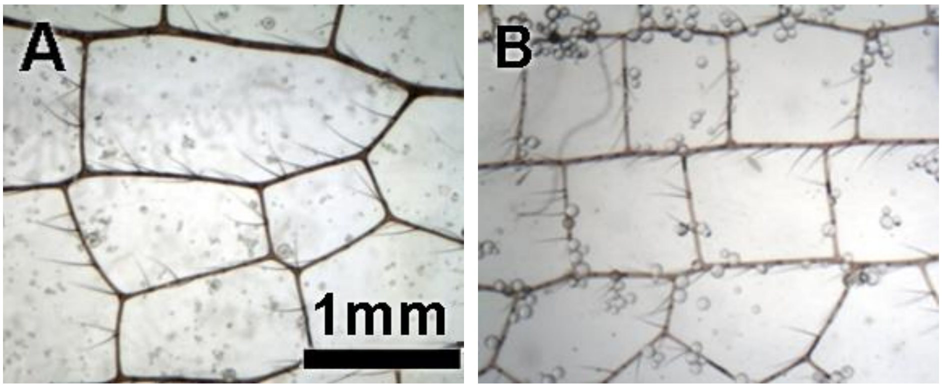

Figure 8.2-2. (A) Base region of the lacewing wing observed under an optical microscope showing light Si bead density and bead size range. (B) Typical density of PMMA beads dispersed on the lacewing.

Large droplets (ca. 33.5 mm^3, spherical radius 2 ± 1.3 mm; more than three times the width of a largest cell on the wing membrane) of double distilled water (ddH_2O) from a polyethylene pipette (Livingstone PTP03) with surface area of ~50 mm^2 were applied onto the base of the wing with the nozzle of the pipette approximately 0.3 cm away from the sample. With the wing base orientated at the top allowing the droplet to roll down along with the inclination of the hairs and off at the tip of the wing. When these large drops are deposited from a pipette onto the wing surface they roll off and the wings remain completely dry. The wettability of the membrane by these large Cdrops is indicated by the removal of the deposited Si beads which decreases with the increase in hair density of each region (Figure 8.2-3). The removal efficiency was calculated as a percentage after contact with 15 large drops.

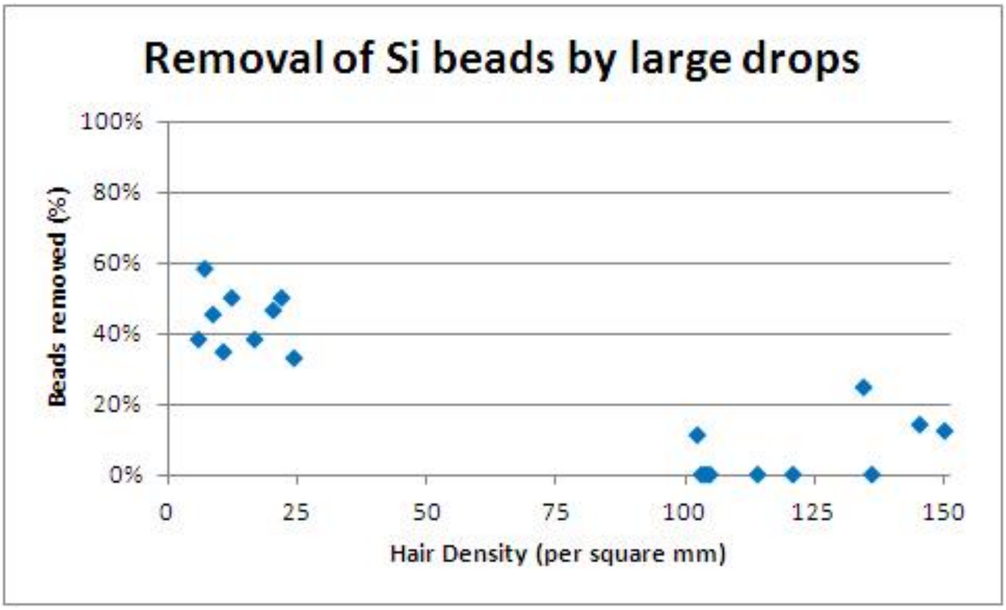

Figure 8.2-3. Comparing the effect of hair density on bead removal by Cdrops. The graph shows a higher removal at regions with lower hair densities.

Smaller droplets (Wdrops) consisted of ddH_2O mists (ca. 0.22 μL, spherical radius 37.55 ± 20 μm; three times less than the width of a small cell on the membrane) with surface area of~0.018 mm^2 were sprayed from a trigger sprayer 50 cm away from the sample setup in the same orientation as that used for larger droplets. From this distance, the hydro-force from the trigger sprayer is assumed to have negligible effects on the experimental results. The remaining Si beads after each experiment were counted. To compare the effectiveness of cleaning by the two methods of wetting, beads removed from 15 sprays were compared to that from 15 large drops. The surface area of one large water drop wetting a contaminated wing sample was similar to the combined surface area of all the mist droplets landing on the wing surface (~2800 from one spray (2800 X 0.018mm^2~ 50mm^2)).

Mist drops can be trapped within the hair layer and some remain on the wing after spraying. Some mist Wdrops were observed to be stuck to a highly wettable region and unable to remove contaminants.

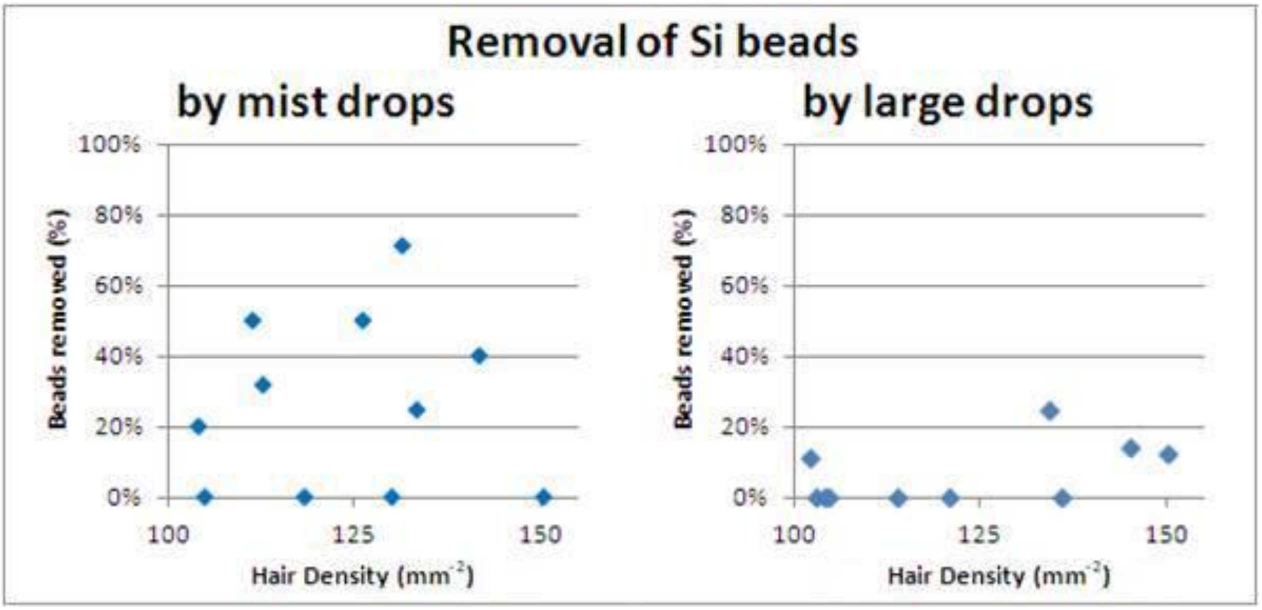

Figure 8.2-4. Comparing the effect of bead removal by the two wetting methods. The difference in the effects is more obvious at high hair density regions where the large drops removes less beads (Figure 8.2-3).

The effectiveness of hairs against wetting by Cdrops is shown in Figure 8.2-3 where at low hair density regions (<25 mm^{-2}) more beads were removed which indicated higher wetting. The hairs reduce wetting to the membrane by Cdrops especially at the wing tips where the hairs are more abundant (>100 mm^{-2}) resulting in a lower efficiency in beads removal. Interestingly, Figure 8.2-4 shows that the smaller mist drops which are less mobile remove more beads than the large drops (discussed later).

Due to the low energy surface and surface structuring of the adult lacewing cuticles, it is unlikely that during their short adulthood in their environments their wings will be deposited with a high density of small contaminants similar to that shown in Figure 8.2-2.

Individually, the weight of these small contaminants (<0.36 μg which is less than 1% of the mass of one wing) are unlikely to affect their flying abilities. Resistance against larger masses or adhesive surfaces that could hinder the insect's mobility (e.g., bulk water surfaces) is more vital.

The hairs support the weight of large Cdrops and reduce the drops' contact with the wing membrane. Together with the hairs' flexibility the droplets are highly mobile on the wing surface. Near the base region of the wing where the distance between neighbouring hairs are further, drops in this region are likely to have more contact with the underlying membrane. Although this will result in a larger cleaned area, the surface in this region is also more vulnerable to pin a Cdrop which can potentially transform into a Wdrop. The drop may be pinned if the combined restoring force of all contacting hairs is not large enough to support the drop to roll past the area. The drop thus loses its mobility and remains stuck to its location.

Unlike smaller contaminant particles, a much heavier water drop (~0.03 g) could potentially hinder the lacewing's flying ability especially wetting to the tip of the wing. The likelihood of complete wetting to the tip region is greatly reduced by the smaller gaps between the hairs ((Figure 8.2-3). As the tip of the wing is located at the extremity of the insect it is more likely to contact other surfaces when flying (e.g., water wetted surfaces). The tip region requires and has higher resistance to water invasion also in the case of contact with bulk adhesive water surfaces (water catchments such as ponds, lakes etc.).

Applying drops from a distance above the membrane surface imposes a kinetic energy which will induce hairs bending towards the membrane. A large area on the membrane can thus be wetted (a higher bead removal) as a result before the drop is pushed away by the restoring forces of the hairs. Bhushan *et al.* (Bhushan et al., 2009) applied artificial rain drops on an artificial superhydrophobic surface and observed that small contaminant particles trapped within the cavities of the surface microstructures were not able to be collected without sufficient impact pressure from the rain drops. The flexibility of the hairs cushioning the drop impact allowing them to bounce off (repel) without dispersing even when dispensed more than 10 cm from above the wing sample. This occurs even when the wing is supported/fixed to a rigid substrate (a glass slide) (normally the flexibility of the wing would also contribute to soften the impact). Hence superhydrophobic surface structures that are flexible could be an advantageous feature on an anti-wetting surface.

The hair surface grooves and channels (Figure 8.1-1) may possibly improve the hair stiffness without adding to the mass and volume of the hairs. They also help reduce contact adhesion and increase the hydrophobicity of the hair surfaces (Hu et al., 2011a, Watson et al., 2010b). Groove structures have been shown to redirect local air-flow resulting in drag reduction (Howard and Goodman, 1985, Bushnell and Moore, 1991, Howlett, 1995).

The smaller Wdrops were seen to adhere to the side of the hairs as shown in Figure 8.2-5. The presence of the hairs helps reduce wetting to the membrane by catching mist droplets including the ones that are smaller than the hair spacings. It is clear from Figure 8.2-5 that many of the droplets are adhered some distance from the hair base. These mist Wdrops and other adhesive small particles will be more accessible for removal by large Cdrops rolling past the area (discussed later).

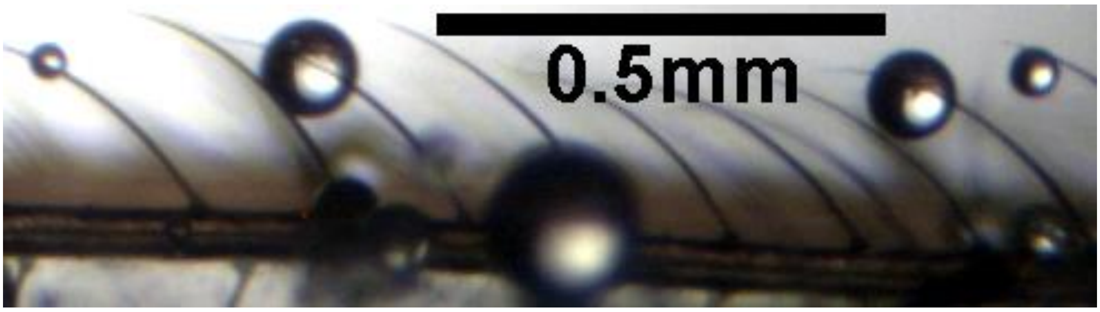

Figure 8.2-5. Hairs prevent wetting of the membrane by water drops landing on the wing. These round drops show low adhesion to the hair can be easily be cleared away by a larger drop rolling past on top of the hair layer.

Despite both the hair and membrane surfaces having structurally enhanced hydrophobicity, mist drops landing on the wings exhibit low mobility. The design of the wing's hydrophobicity (in view of the hair spacing) appears to contend against water bodies larger than 2 mm (larger than the width of a larger cell). Whether the mist droplets initially land on a hair or the membrane, it was observed that as coalescing continues upon further spraying, the mist droplets are likely to end up pinned at the hair bases. Despite the lack of mobility, results show that the mist droplets have higher ability to remove more contaminants which suggest that not all the drops remain permanently trapped within the hair layer.

Figure 8.2-6 are screenshots taken from a video at various time intervals showing the mist drops on the wing tilted at 45° can coalesce and make the transition off the membrane to the top of the hair layer (i.e. Wdrops becoming Cdrops). Transiting from Wdrop to Cdrop seems to be a path requiring less energy than rolling through the hair layer.

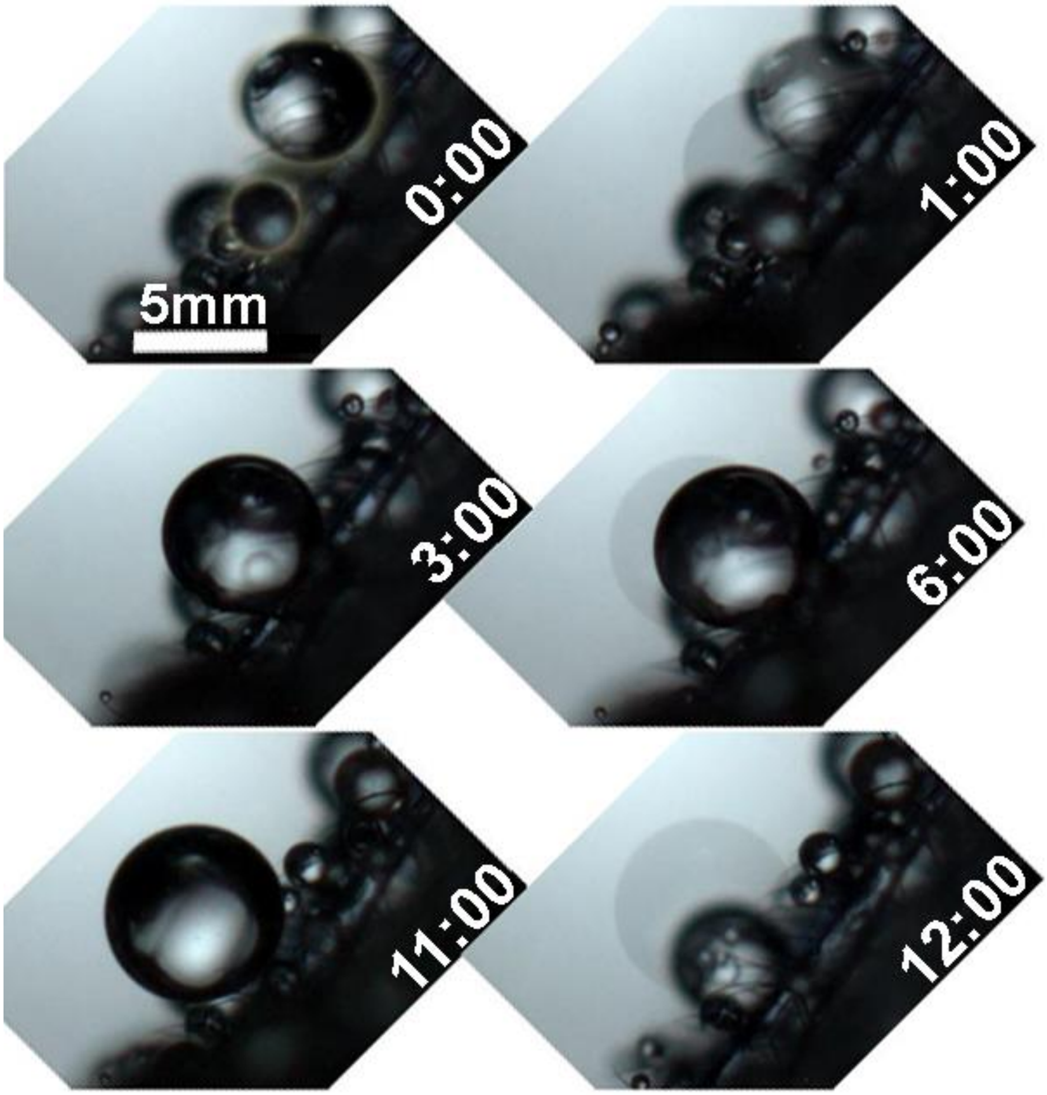

Figure 8.2-6. Series of video images showing at [0:00] two droplets (highlighted) on a sample tilted at 45° and coalescing together to the centre of the frame at [2:00] (shadow in [1:00]). At [11:00] has transited to the tip of the hair (shadow in [6:00]) before rolling off at [12:00] after further mist application.

Regions around the hair bases are least accessible by Cdrops(Figure 8.2-7) but are gathering areas for smaller mist droplets. Despite all parts of the wing being hydrophobic, the mechanism of cleaning around the hair bases is quite different due to the hairs hindering the mobility of the Wdrops. Rather than being collected by Cdrops rolling on the surface, the contaminants are picked up by the growing Wdrops as their solid-liquid contact area spread. Similar to the self-cleaning mechanism on a superhydrophilic surface the Wdrop can run off the surface if it spreads past the edge of the wing. Otherwise the drops would coalesce to a larger size and will move off the wing by firstly transiting to Cdrops.

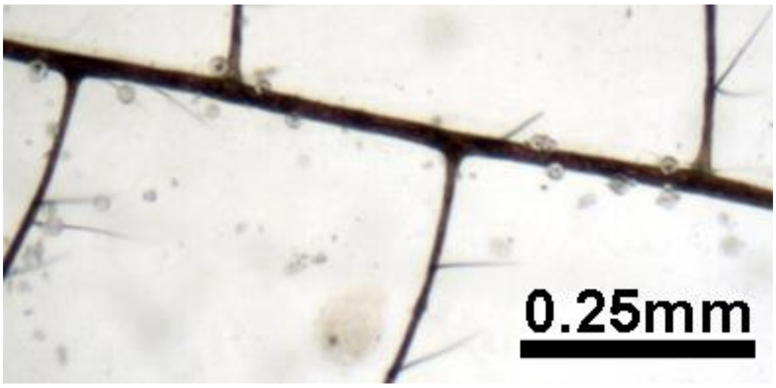

Figure 8.2-7. Wing cleaned by Cdrops. Beads remain are mostly those near the veins.

A possible mechanism of removing sticky Wdrops from the wing surface may be explained by the nanostructure of the hairs. The lacewing hairs have similar surface groove alignments as the hairs on the water strider legs (Watson et al., 2010) and craneflies (Hu et al., 2011a) (Chapter 7) which direct wetting along the length of the hair. As the drop at the base of the hair grows larger, its centre of mass shifts away from the membrane. On a tilted sample the Wdrop would eventually reach a size causing the supporting hair to bend significantly allowing the drop to shift towards the tip of the hair and detach from the membrane (Figure 8.2-8). The Wdrop has transited to a Cdrop and it rolls off the wing on the tip of the hairs.

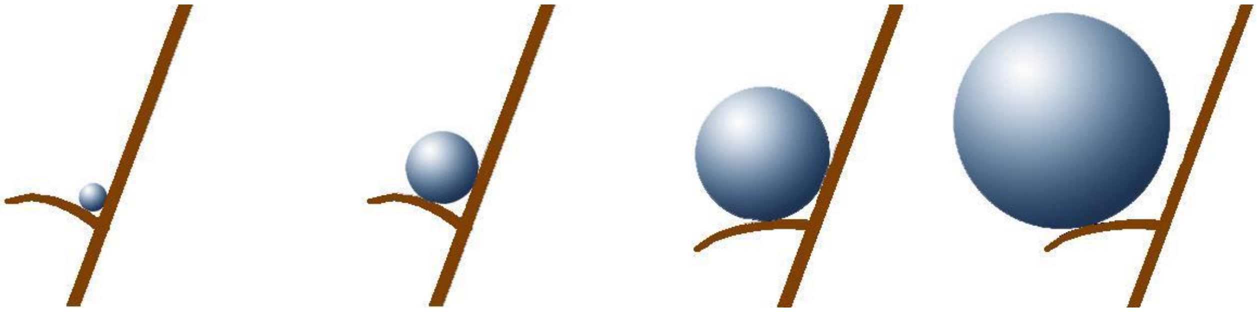

Figure 8.2-8. A schematic diagram presenting a Wdrop adhered to the base of the hair on a tilted sample grows in size and detaches from the membrane.

There are other examples in nature where small water drops on hydrophobic surfaces are required to grow to a large enough size before they become useful for the surface removal mechanisms. The beetle *Stenorca* that inhabits the Namib desert have hydrophilic spots on their hydrophobic wings that are gathering areas to help them collect drinking water from moisture in the air (Parker and Lawrence, 2001). The mechanism involve the fog drops deposited on the wings to coalesce on the spots until they reach a size allowing them to be blown by the wind towards the beetle's mouth (Bush et al., 2007).

Figure 8.2-9(A) shows that even without the aid of gravity, a large Wdrop in contact with multiple hairs on a sample laid flat is able to make the vertical transition to above the hair layer. Schematically represented in Figure 8.2-9(B) the Wdrop experiences a squeezing pressure from the contacting hairs and will grow to a point when it becomes less favourable to remain constricted within/between the hair layer. The transition is normally triggered when the drop combines with another in close proximity. The resulting excess kinetic energy from the coalescence and change in surface energy (which is up to ten times the energy barrier for Wenzel to Cassie-Baxter transition (Boreyko and Chen, 2009)) could also help the vertical transition. Once coalesced and transitioned (repelled) out of the hair layer where the solid-liquid contact is reduced, the highly mobile Cdrop carrying contaminants can easily roll off Figure 8.2-9(C).

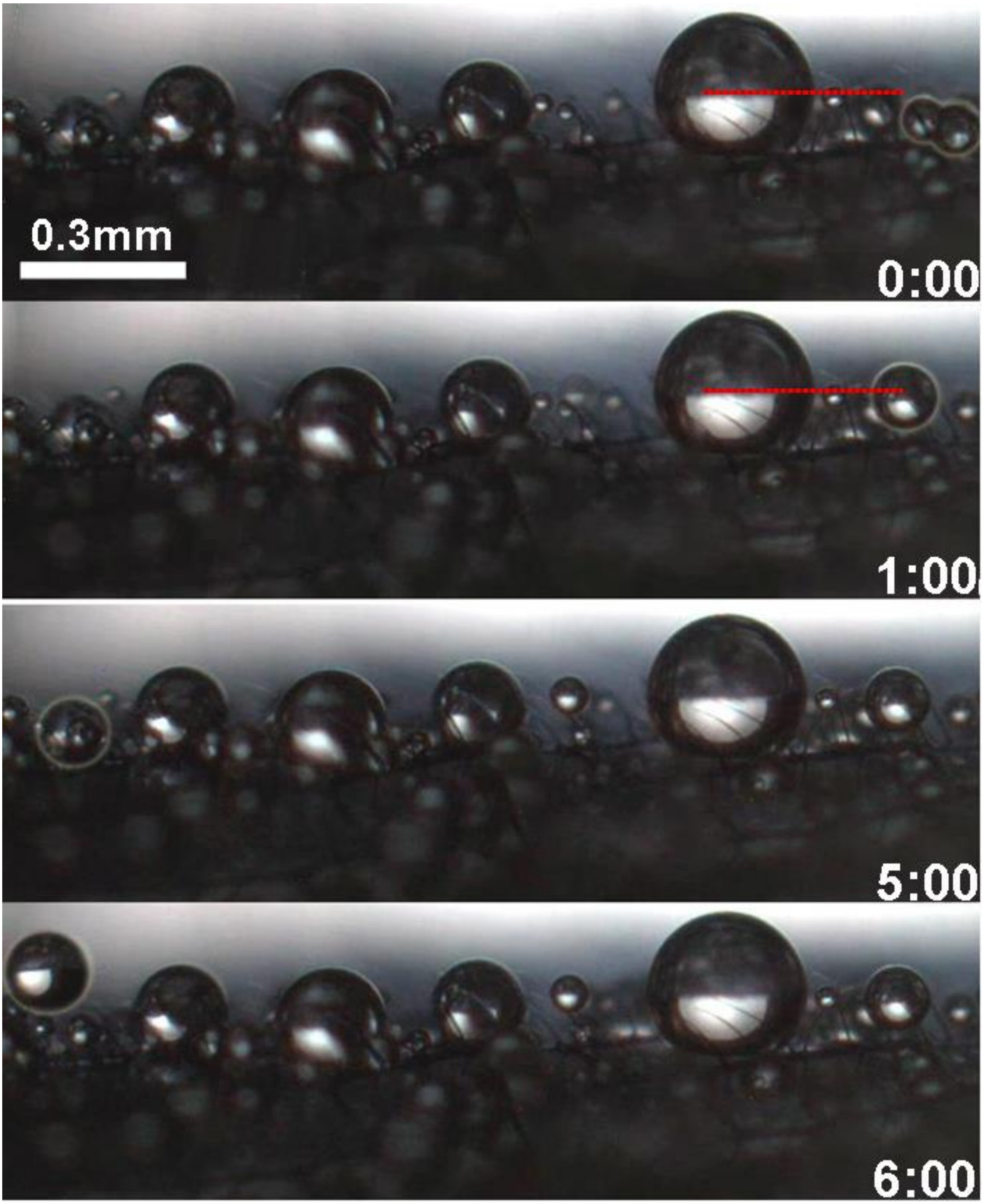

Figure 8.2-9. (A) Highlighted drops at [0:00] coalesces and becomes a Cdrop in [1:00] (red line added to show movement). Another Wdrop-Cdrop transition on the left at [6:00] where the highlighted drop in [5:00] combines with a drop behind it.

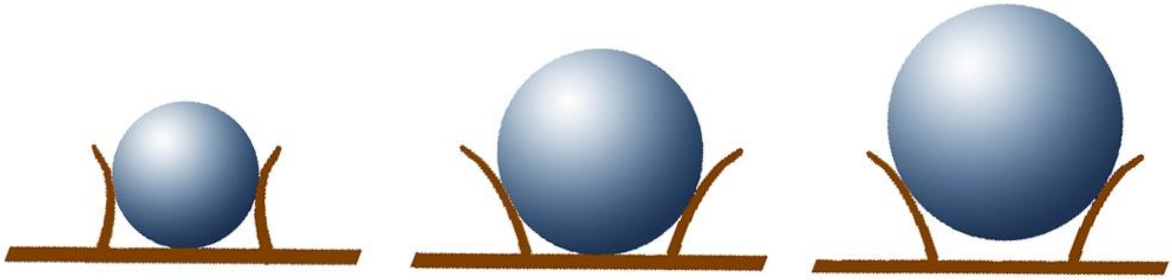

Figure 8.2-9. (B) A schematic diagram presenting a Wdrop to Cdrop transition on a sample laid flat. The Wdrop is squeezed by the contacting hairs as it grows in size.

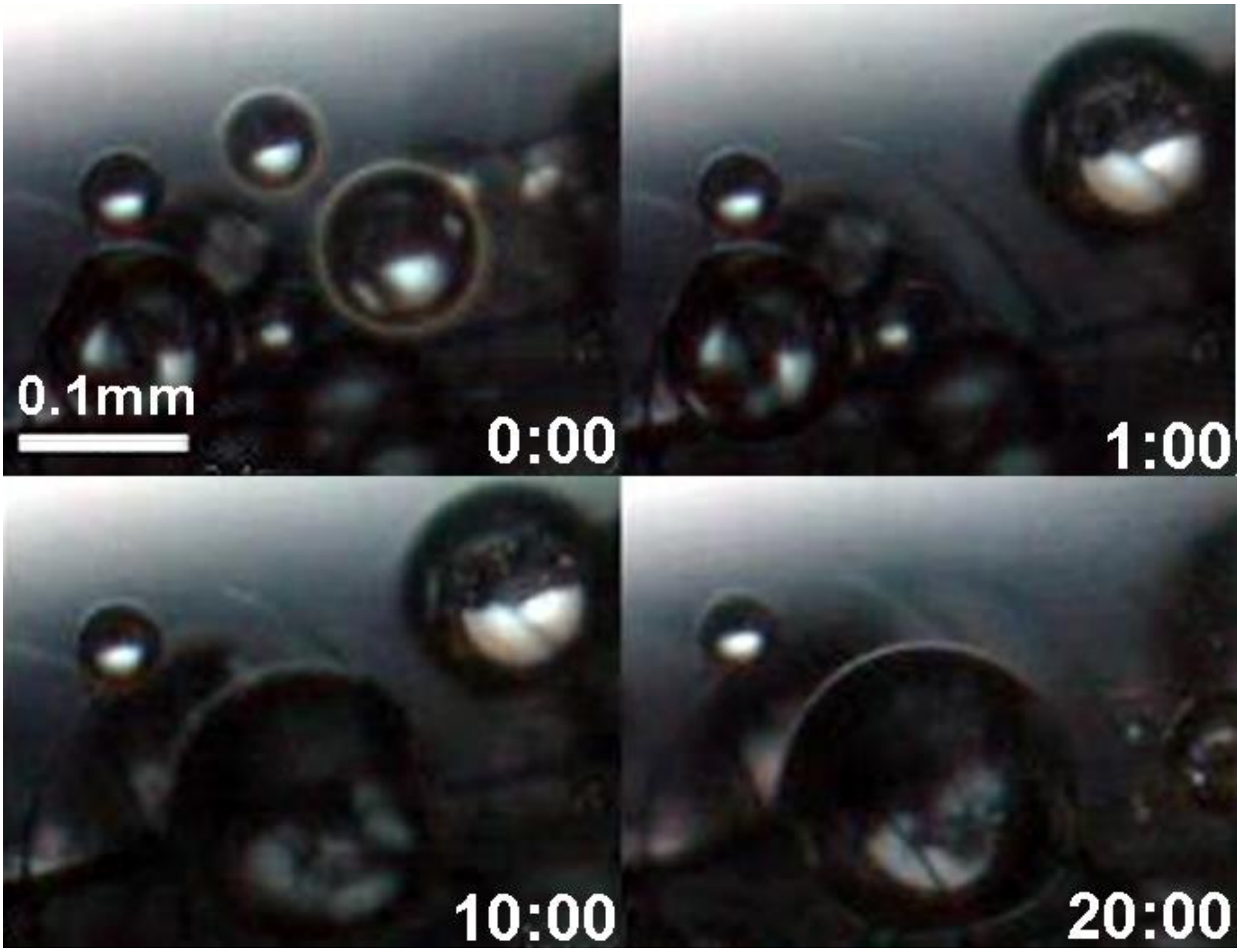

Figure 8.2-9.(C) The larger highlighted drops at [0:00] coalesces with a drop behind. Picks up the other highlighted drop as it moved to the top right corner of the frame in [1:00] and [10:00]. Detaches and rolls off at [20:00] after further mist application.

Another experiment was conducted with the tip end of the contaminated wing (orientated at the bottom) covered (but not touching the hair layer) from 15 sprays of mists. Although the covered region remained dry, there was a significant amount of beads removed (mainly in areas away from hair bases) suggesting Cdrops (and not Wdrops) had rolled past over the region.

Before rolling off the wing, these transited Cdrops are also able to pick up other contaminants on the wing, especially large contaminants and particles adhered higher up from the base of hairs. PMMA beads were used to mimic larger contaminant particles and Figure 8.2-10 show that their removal by Cdrops is much higher due to higher accessibility. Wdrops adhered to the wing surface can also be removed by washing with Cdrops (for instance from a pipette) (also reported on other insects (Watson et al., 2010a)); an interesting method of drying a wet sample surface with water.

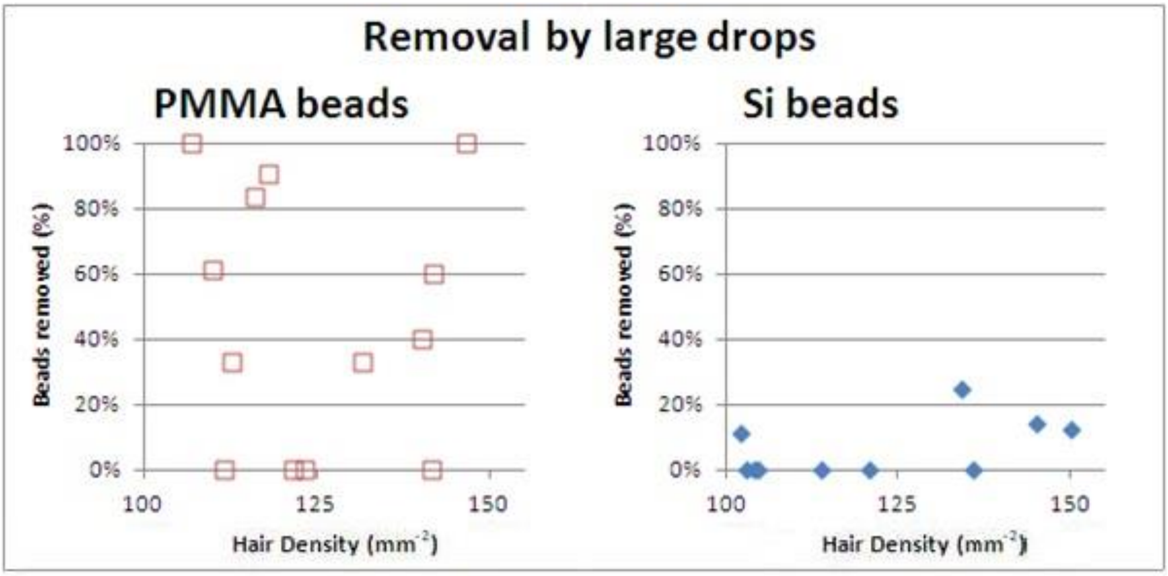

Figure 8.2-10. Compares the effect of bead size on removal by Cdrops. At high hair density the difference is more prominent.

The water repelling mechanism (Wdrop transiting to Cdrops) is more likely to occur at regions with dense hairs where the droplets have less space to grow and hence less mass requiring less energy to transit against gravity to detach from the membrane.

The nanoscale features on the membrane surface reduces contact and adhesion of the beads on the wing and many of these beads can be shaken off by gently flapping the wing sample by hand. Mechanical distortions from flapping of the wings by the lacewing during flight should allow the contaminants to easily become dislodged off the surface especially at the tip region which experiences the largest amplitude during flight.

For mist droplets and other contaminants of similar sizes, the existence of the hairs provides more surface area available for adhesion. The increase in wing surface area however enhances the insect's aerodynamic performance by re-directing local turbulent near the wing surface (Dudley, 2000). Vortices that are similar to those generated around the bases of tall buildings (Baskaran and Kashef, 1996, Chang and Meroney, 2003, Greenland, 1989, Meroney et al., 1999) in the urban areas might also be formed on the microscale around the hair bases where drops and contaminants gather. Turbulent generated around these locations during flight might possibly help dislodge the foreign particles.

Due to the larger dimensions of the hair features on the wing surface they are not effective against the tiny mist drops. In small quantities the mist drops are unlikely to affect the insect's mobility significantly until they are large enough to weigh down the insect or impede wing movement. The contacting hairs may also apply a (squeezing) force to increase the potential for the drop to be dislodged when the insect moves it wings.

Water repelling and self-cleaning are two surface properties that often coexist. Evolution may also intend for this water repelling mechanism to be a method of self-cleaning for difficult areas (i.e. hair bases). Utilizing water drops of various sizes, this self-cleaning mechanism involves gathering the small mist drops to the base of the hairs where they are required and eventually transit to the top of the hair layer, where they become highly mobile to remove other contaminants and Wdrops. The same experiment conducted on a cicada wing show the contaminants and mists tend to pile at the corners of the cells (where the veins cross) exposing a larger cleaned area where anti-reflection is maintained. The mists gather at the corners until they are large enough to roll over the veins and off the wing.

Cdrop mobility and stability are two conflicting properties where one can be increased but at the cost of the other. The drop mobility can be increased by reducing the solid-liquid contact however by doing so reduces the stability of the water drop in the anti-wetting regime. Liquid invasion by a Cdrop can be triggered by tiny droplets deposited in between spacings of the surface structures (Mockenhaupt et al., 2008). These small droplets can set off the Cassie-Wenzel transition if in abundance. Even the lotus leaves being exposed to condensation or long lasting rainfall can become adhesive to large drops (Cheng and Rodak, 2005, Cheng et al., 2005, Jung and Bhushan, 2008, Mockenhaupt et al., 2008, Narhe and Beysens, 2007, Wier and McCarthy, 2006).

It would be ideal to have both mobility and stability as highly efficient as possible however while many have suggested ways of increasing superhydrophobicity without sacrificing the anti-wetting stability (e.g., using multiple scale structures), very few (if any) have looked at ways of self-restoring the superhydrophobicity of a drop corrupted from heterogeneous (Cdrop) to homogeneous (Wdrop) regime. A restoring mechanism of removing a drop saturating the wing surface (and the resultant Cdrop rolling off can leave behind a dry path) has been observed on the wing of *Nymphes myrmeleonides*.

During its short adulthood, the lacewing is unlikely to encounter contaminants or mists in a detrimental amount similar to what was exposed to the samples in this work. The efficiencies of the water repelling and self-cleaning mechanisms introduced in this work are limited by surface features constrained to serve other more dominant functions most importantly the protection against large water surfaces. As it may be one of the less vital functions for the insects' survival, the mechanism may require some fine tuning to increase its efficiency, possibly a secondary hair layer consisting of smaller hairs as reported on the membrane of the brown lacewing (*Micromus tasmaniae*) (Watson et al., 2011b) to contend with the finer mist droplets (Figure 8.2-11).

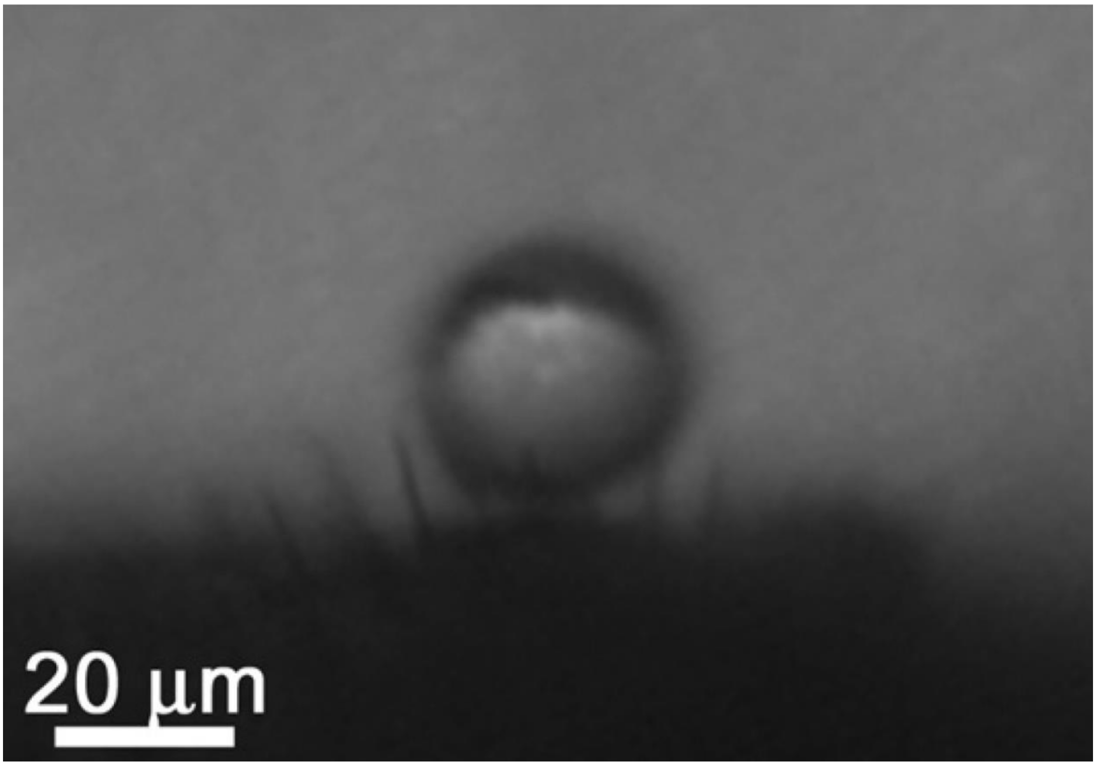

Figure 8.2-11. Side view of optical microscope images showing microdroplets on a *Micromus tasmaniae* wing. The droplets maintain their spherical shape and occupy regions between the macrotrichia arrays, that is, on top of the microtrichia array.

Like many other insect cuticles that display multiple properties and functionalities, lacewing cuticle is a surface displaying anti-wetting, self-cleaning and Wdrop repelling properties and other aerodynamic functions. The idea of combining various bulk material properties (thermal, optical, mechanical etc.) into a hybrid material is not uncommon (Vincent, 2008, Ashby and Brechet, 2003, Eadie and Ghosh, 2011, Vincent, 2009). By understanding the relationship between the shape of surface structures and their functional mechanisms, it may become a future trend in man-made technology to introduce new functions and multiple functions onto surfaces of synthetic hybrid materials.

8.3 CHAPTER SUMMARY

The wings of the *Nymphes myrmeleonides* like many other insects are multifunctional surfaces. Mechanisms for anti-contaminating, water resisting and removal and self-cleaning all require low energy surfaces and the efficiency of these mechanisms depend on the importance of the function to the lacewing's survival. Removal of small beads by water bodies larger than ~2 mm is prevented by the hairs which serve the more vital purpose of reducing contact with foreign bodies that are large enough to immobilise the insect. However the restoring forces from the hairs surrounding smaller water bodies on the wing are responsible for repelling them away from the cuticle surface. Greater understanding of this water repelling mechanism which involves flexible surface structures may lead to the development of surfaces that can efficiently restore corrupted Cassie-Baxter droplets to maintain superhydrophobicity and other functions on a tailored multifunctional surface.

9 CONCLUSION

This thesis addressed a number of scientific problems focused on the control of adhesional properties between surfaces (solid-solid and solid-liquid interactions). Adhesion, wetting and frictional control between surfaces at a wide range of length scales is important in a variety of industrial applications and future technologies including creating the next generation of multifunctional, super adhesive and solid and liquid contamination resistant surfaces.

Focusing on the correlated wetting and adhesional properties on a range of insect wing membranes, Chapters 4, 5 and 6 utilised the AFM and the SEM to visualise and analyse the nanostructures and properties of surfaces. The contact forces of contaminating bodies of different length scales (and chemistry) were evaluated by measuring the strength of interaction between particles with selected insect cuticle micro/nanostructuring. An open framed intricate structuring characteristic of hydrophobic insect species showed minimal adhesion with water and particles of all sizes and chemistry. Indeed many of the insect species demonstrated a superhydrophobic interaction with water. As the growth of most micro-organisms is provided by permanent or temporary water availability which can lead to the formation of biofilms this superhydrophobic property may well protect the insects from pathogens such as fungi and bacteria by limiting water availability. Some of these insects may also encounter periods without rainfall and fogging conditions for self-cleaning of wing surfaces. Low adhesion and friction may aid in these circumstances to minimise contamination from foreign bodies and facilitate removal.

In contrast to the hydrophobic species examined, hydrophilic cuticles showed lower contact angles and higher adhesion with particles. The different size-ranges were used to ascertain the contact conditions of particles which would normally come into contact with the cuticle surfaces. The unique topographical micro and nano structures found on the insect surfaces demonstrate design characteristics and features for surfaces with low/high wettability, adhesion and friction.

The diversity of the structure topographies demonstrates a range of architectures suitable for optimising surface properties and replication for man-made structures/applications. Indeed a range of new materials (for example self-cleaning, antifouling, anti-reflective surfaces) may well be utilised in environments where the surfaces are intermittently submerged. Thus functionality must be maintained in both terrestrial and aquatic environments. These new materials may constitute a marriage of structural and chemical components/properties gleaned from both aquatic and terrestrial organisms. The insect structures provide a set of well characterised 'technologies' which incorporate a range of properties primarily focused on reducing adhesion with solid and water bodies. Many of these insects displaying unique structural architecture also represent good candidates for investigations in aqueous environments.

The second half of the thesis focused on the interaction of water droplets with hairs on the cranefly (*Nephrotoma australasiae*) followed by the lacewing (*Nymphes myrmeleonides*).

Enhanced by various hair arrangements and their grooves, the low adhesive and wetting properties of the cranefly and lacewing cuticles allow the insects to interact with a variety of environmental surfaces and conditions that could immobilize the insect. The results supported the hypothesis of Watson *et al.* (Watson et al., 2010) which suggested micro/nanoscale structures found on water striders can resist water adhesion.

While many researches focus on preventing the corruption of composite drops on superhydrophobic surfaces, a true water repelling mechanism that restores corrupted drops was reported in Chapter 8. The mechanism was observed on lacewing cuticles when their interactions with mist droplets were video recorded in real-time. The flexibility of the hairs plays a role in the removal of little droplets once they coalesce to a size that can be contended with.

Potential applications for these hair structures extend beyond the electromechanical field. The surface area increased by the hairs could be used for moisture collection similar to the wings of the Namib Desert beetle. Water repelling functions could also be imitated onto our garments. The increasingly popular compression garments worn by athletes to improve performance level require moisture removal technology (from rain, humidity or sweat) to minimise discomfort, absorbed weight and changes to the mechanical property (hence the functional efficiency) of the textile (Gupta, 2011, Kang et al., 2007, Troynikov et al., 2001).

Relative to many other nanotechnology field and material science, the research in this thesis is still in its infancy and will surely greatly benefit from more newly developed instruments and methodologies. Further work will no doubt lead to the discoveries of many more potentially useful mechanisms. Better knowledge of these surface properties and mechanisms will lead to more efficient fine-tuned surface functions and smarter multi-functional materials.

10 REFERENCES

ABDELSALAM, M. E., BARTLETT, P. N., KELF, T. & BAUMBERG, J. 2005. Wetting of regularly structured gold surfaces. Langmuir, 21, 1753-1757.

ANANTHARAJU, N., PANCHAGNULA, M. V., VEDANTAM, S., NETI, S. & TATIC-LUCIC, S. 2007. Effect of three-phase contact line topology on dynamic contact angles on heterogeneous surfaces. Langmuir, 23, 11673-11676.

ANDERSEN, N. M. & CHENG, L. 2005. The marine insect *Halobates* (Heteroptera : Gerridae): Biology, adaptations, distribution, and phylogeny. Oceanography and Marine Biology: An Annual Review, Vol 42. Boca Raton: (Crc Press-)Taylor & Francis (Group).

ANDO, Y. & INO, J. 1998. Friction and pull-off forces on submicron-size asperities. Wear, 216, 115-122.

ASHBY, M. F. & BRECHET, Y. J. M. 2003. Designing hybrid materials. Acta Materialia, 51, 5801-5821.

BARBIERI, L., WAGNER, E. & HOFFMANN, P. 2007. Water wetting transition parameters of perfluorinated substrates with periodically distributed flat-top microscale obstacles. Langmuir, 23, 1723-1734.

BARTHLOTT, W. & NEINHUIS, C. 1997. Purity of the sacred lotus, or escape from contamination in biological surfaces. Planta, 202, 1-8.

BARTLETT, P. N., BAUMBERG, J. J., BIRKIN, P. R., GHANEM, M. A. & NETTI, M. C. 2002. Highly ordered macroporous gold and platinum films formed by electrochemical deposition through templates assembled from submicron diameter monodisperse polystyrene spheres. Chemistry of Materials, 14, 2199-2208.

BASKARAN, A. & KASHEF, A. 1996. Investigation of air flow around buildings using computational fluid dynamics techniques. Engineering Structures, 18, 861-875.

BHUSHAN, B. 2002. Introduction to tribology, New York, John Wiley.

BHUSHAN, B. & JUNG, Y. C. 2008. Wetting, adhesion and friction of superhydrophobic and hydrophilic leaves and fabricated micro/nanopatterned surfaces. Journal of Physics: Condensed Matter 20, 225010-225033.

BHUSHAN, B., JUNG, Y. C. & KOCH, K. 2009. Self-cleaning efficiency of artificial superhydrophobic surfaces. Langmuir, 25, 3240-3248.

BLACH, J. A., WATSON, G. S., BROWN, C. L., PHAM, D. K., WRIGHT, J., NICOLAU, D. V. & MYHRA, S. 2004. A mechanistic approach to tip-induced nano-lithography of polymer surfaces. Thin Solid Films, 459, 95-99.

BLOSSEY, R. 2003. Self-cleaning surfaces - virtual realities. Nature Materials, 2, 301-306.

BOREYKO, J. B. & CHEN, C.-H. 2009. Self-propelled dropwise condensate on superhydrophobic surfaces. Physical Review Letters, 103, 184501.

BORMASHENKO, E. 2008. Why does the Cassie-Baxter equation apply? Colloids and Surfaces a-Physicochemical and Engineering Aspects, 324, 47-50.

BRANDON, S., HAIMOVICH, N., YEGER, E. & MARMUR, A. 2003. Partial wetting of chemically patterned surfaces: the effect of drop size. Journal of Colloid and Interface Science, 263, 237-243.

BURNEY, P. G. J., NEWSON, R. B., BURROWS, M. S. & WHEELER, D. M. 2008. The effects of allergens in outdoor air on both atopic and nonatopic subjects with airway disease. Allergy, 63, 542-546.

BURTON, Z. & BHUSHAN, B. 2005. Hydrophobicity, adhesion, and friction properties of nanopatterned polymers and scale dependence for micro- and nanoelectromechanical systems. Nano Letters, 5, 1607-1613.

BUSH, J. W. M., HU, D. L. & PRAKASH, M. 2007. The integument of water-walking arthropods: form and function. Advances in Insect Physiology: Insect Mechanics and Control. San Diego: Elsevier Academic Press Inc.

BUSHNELL, D. M. & MOORE, K. J. 1991. Drag reduction in nature. Annual Review of Fluid Mechanics, 23, 65-79.

BUTT, H. J., CAPPELLA, B. & KAPPL, M. 2005. Force measurements with the atomic force microscope: technique, interpretation and applications. Surface Science Reports, 59, 1-152.

CARINANOS, P., ALCAZAR, P., GALAN, C., NAVARRO, R. & DOMINGUEZ, E. 2004. Aerobiology as a tool to help in episodes of occupational allergy in work places. Journal of Investigational Allergology and Clinical Immunology, 14, 300-308.

CASSIE, A. B. D. & BAXTER, S. 1944. Wettability of porous surfaces. Journal of the Chemical Society, Faraday Transactions, 40, 546-551.

CHANG, C. H. & MERONEY, R. N. 2003. Concentration and flow distributions in urban street canyons: wind tunnel and computational data. Journal of Wind Engineering and Industrial Aerodynamics, 91, 1141-1154.

CHENG, L. 1973. Marine and freshwater skaters: differences in surface fine structures. Nature, 242, 132-133.

CHENG, Y. T. & RODAK, D. E. 2005. Is the lotus leaf superhydrophobic? Applied Physics Letters, 86, 144101.

CHENG, Y. T., RODAK, D. E., ANGELOPOULOS, A. & GACEK, T. 2005. Microscopic observations of condensation of water on lotus leaves. Applied Physics Letters, 87. 194112

CHUNG, J. Y., YOUNGBLOOD, J. P. & STAFFORD, C. M. 2007. Anisotropic wetting on tunable micro-wrinkled surfaces. Soft Matter, 3, 1163-1169.

CLEVELAND, J. P., MANNE, S., BOCEK, D. & HANSMA, P. K. 1993. A nondestructive method for determining the spring constant of cantilevers for scanning force microscopy. Review of Scientific Instruments, 64, 403-405.

CONG, Q., CHEN, G. H., FANG, Y. & REN, L. Q. 2004. Study on the super-hydrophobic characteristic of butterfly wing surface. Journal of Bionics Engineering, 1, 249.

D'AMATO, G. 2002. Environmental urban factors (air pollution and allergens) and the rising trends in allergic respiratory diseases. Allergy, 57, 30-33.

DE NYS, R. & STEINBERG, P. D. 2002. Linking marine biology and biotechnology. Current Opinion in Biotechnology, 13, 244-248.

DING, M., CHEN, F., SHI, X. L., YUCESOY, B., MOSSMAN, B. & VALLYATHAN, V. 2002. Diseases caused by silica: mechanisms of injury and disease development. International Immunopharmacology, 2, 173-182.

DUCKER, W. A., SENDEN, T. J. & PASHLEY, R. M. 1991. Direct measurement of colloidal forces using an atomic force microscope. Nature, 353, 239-241.

DUDLEY, R. 2000. The biomechanics of insect flight: form, function, evolution, Princeton University Press {a} , 41 William Street, Princeton, NJ, 08540, USA.

EADIE, L. & GHOSH, T. K. 2011. Biomimicry in textiles: past, present and potential. An overview. Journal of the Royal Society Interface, 8, 761-775.

EXTRAND, C. W. 2003. Contact angles and hysteresis on surfaces with chemically heterogeneous islands. Langmuir, 19, 3793-3796.

EXTRAND, C. W. 2006. Designing for optimum liquid repellency. Langmuir, 22, 1711-1714.

FANG, Y., SUN, G., WANG, T., CONG, Q. & REN, L. 2007. Hydrophobicity mechanism of non-smooth pattern on surface of butterfly wing. Chinese Science Bulletin, 52, 711-716.

FRISBIE, C. D., ROZSNYAI, L. F., NOY, A., WRIGHTON, M. S. & LIEBER, C. M. 1994. Funtional-group imaging by chemical force microscopy. Science, 265, 2071-2074.

GAO, L. & MCCARTHY, T. J. 2006a. Contact angle hysteresis explained. Langmuir, 22, 6234-6237.

GAO, L. C. & MCCARTHY, T. J. 2006b. "Artificial lotus leaf" prepared using a 1945 patent and a commercial textile. Langmuir, 22, 5998-6000.

GAO, L. C. & MCCARTHY, T. J. 2007a. How Wenzel and Cassie were wrong. Langmuir, 23, 3762-3765.

GAO, L. C. & MCCARTHY, T. J. 2007b. Reply to "Comment on How Wenzel and Cassie Were Wrong by Gao and McCarthy". Langmuir, 23, 13243-13243.

GENZER, J. & EFIMENKO, K. 2006. Recent developments in superhydrophobic surfaces and their relevance to marine fouling: a review. Biofouling, 22, 339-360.

GIBSON, C. T., WATSON, G. S. & MYHRA, S. 1996. Determination of the spring constants of probes for force microscopy/spectroscopy. Nanotechnology, 7, 259-262.

GIBSON, C. T., WATSON, G. S. & MYHRA, S. 1997. Scanning force microscopy - calibrative procedures for 'best practice'. Scanning, 19, 564-581.

GORB, S. N., KESEL, A. & BERGER, J. 2000. Microsculpture of the wing surface in Odonata: evidence for cuticular wax covering. Arthropod Structure & Development, 29, 129-135.

GREENLAND, D. 1989. BOUNDARY-LAYER CLIMATES - OKE,TR. Professional Geographer, 41, 388-389.

GUPTA, D. Functional clothing-Definition and classification. Indian Journal of Fibre & Textile Research, 36, 321-326.

HARRIS, C. M. & CREDE, C. E. 1976. Shock and vibration handbook, New York, McGraw-Hill.

HASAN, J., WEBB, H. K., TRUONG, V. K., POGODIN, S., BAULIN, V. A., WATSON, G. S., WATSON, J. A., CRAWFORD, R. J. & IVANOVA, E. P. 2013. Selective bactericidal activity of nanopatterned superhydrophobic cicada *Psaltoda claripennis* wing surfaces. Applied Microbiology and Biotechnology, 97, 9257-9262.

HASAN , J., WEBB, H. K., TRUONG, V. K., WATSON, G. S., WATSON, J. A., TOBIN, M. J., GERVINSKAS, G., JUODKAZIS, S., WANG, J. Y., CRAWFORD, R. J. & IVANOVA, E. P. 2012. Spatial Variations and Temporal Metastability of the Self-Cleaning and Superhydrophobic Properties of Damselfly Wings. Langmuir, 28, 17404-17409.

HELLEMANS, L., WAEYAERT, K., HENNAU, F., STOCKMAN, L., HEYVAERT, I. & VANHAESENDONCK, C. 1991. Can atomic force microscopy tips be inspected by atomic force microscopy. Journal of Vacuum Science & Technology B, 9, 1309-1312.

HERMINGHAUS, S. 2000. Roughness-induced non-wetting. Europhysics Letters, 52, 165-170.

HILLBORG, H. & GEDDE, U. W. 1999. Hydrophobicity changes in silicone rubbers. Ieee Transactions on Dielectrics and Electrical Insulation, 6, 703-717.

HNIZDO, E. & VALLYATHAN, V. 2003. Chronic obstructive pulmonary disease due to occupational exposure to silica dust: a review of epidemiological and pathological evidence. Occupational and Environmental Medicine, 60, 237-243.

HOLDGATE, M. W. 1955. The wetting of insect cuticles by water. Journal of Experimental Biology, 32, 591-617.

HOPCROFT, M. A., NIX, W. D. & KENNY, T. W. 2010. What is the Young's Modulus of Silicon? Microelectromechanical Systems, Journal of, 19, 229-238.

HOWARD, F. G. & GOODMAN, W. L. 1985. Axisymmetric bluff-body drag reduction through geometrical modification. Journal of Aircraft, 22, 516-522.

HOWLETT, R. 1995. Life in moving fluids – the physical biology of flow, 2nd edition - Vogel,S. Nature, 373, 114-114.

HSU, B. B. & KLIBANOV, A. M. 2010. Light-activated covalent coating of cotton with bactericidal hydrophobic polycations. Biomacromolecules, 12, 6-9.

HU, H. M., WATSON, G. S., WATSON, J. A. & CRIBB, B. W. 2011a. Multi-functional insect cuticles: informative designs for man-made surfaces. World Academy of Science, Engineering and Technology, 5, 1370-1371.

HU, H. M., WATSON, J. A., CRIBB, B. W. & WATSON, G. S. 2011b. Fouling of nanostructured insect cuticle: adhesion of natural and artificial contaminants. Biofouling, 27, 1125-1137.

IVANOVA, E., HASAN, J., TRUONG, V., WANG, J., RAVEGGI, M., FLUKE, C. & CRAWFORD, R. 2011. The influence of nanoscopically thin silver films on bacterial viability and attachment. Applied Microbiology and Biotechnology, 91, 1149-1157.

IVANOVA, E. P., HASAN, J., WEBB, H. K., GERVINSKAS, G., JUODKAZIS, S., TRUONG, V. K., WU, A. H. F., LAMB, R. N., BAULIN, V. A., WATSON, G. S., WATSON, J. A., MAINWARING, D. E. & CRAWFORD, R. J. 2013. Bactericidal activity of black silicon. Nature Communications, 4, 2838-2844.

IVANOVA, E. P., HASAN, J., WEBB, H. K., TRUONG, V. K., WATSON, G. S., WATSON, J. A., BAULIN, V. A., POGODIN, S., WANG, J. Y., TOBIN, M. J., LÖBBE, C. & CRAWFORD, R. J. 2012a. Natural Bactericidal Surfaces: Mechanical Rupture of Pseudomonas aeruginosa Cells by Cicada Wings. Small, 8, 2489-2494.

IVANOVA, E. P., HASAN, J., WEBB, H. K., TRUONG, V. K., WATSON, G. S., WATSON, J. A., BAULIN, V. A., POGODIN, S., WANG, J. Y., TOBIN, M. J., LÖBBE, C. & CRAWFORD, R. J. 2012b. Natural Bactericidal Surfaces: Mechanical rupture of *Pseudomonas aeruginosa* cells by cicada wings. Small, 8, 2489-2494.

JING, G. Y., MA, J. & YU, D. P. 2007. Calibration of the spring constant of AFM cantilever. Journal of Electron Microscopy, 56, 21-25.

JUNG, Y. C. & BHUSHAN, B. 2008. Wetting behaviour during evaporation and condensation of water microdroplets on superhydrophobic patterned surfaces. Journal of Microscopy-Oxford, 229, 127-140.

KANG, Y. K., PARK, C. H., KIM, J. & KANG, T. J. 2007. Application of electrospun polyurethane web to breathable water-proof fabrics. Fibers and Polymers, 8, 564-570.

KIM, J., CHAUDHURY, M. K. & OWEN, M. J. 1999. Hydrophobicity loss and recovery of silicone HV insulation. Ieee Transactions on Dielectrics and Electrical Insulation, 6, 695-702.

KNAAPEN, A. M., BORM, P. J. A., ALBRECHT, C. & SCHINS, R. P. F. 2004. Inhaled particles and lung cancer. Part A: Mechanisms. International Journal of Cancer, 109, 799-809.

LAFUMA, A. & QUERE, D. 2003. Superhydrophobic states. Nature Materials, 2, 457-460.

LARGE, M. C. J., WICKHAM, S., HAYES, J. & POLADIAN, L. 2007. Insights from nature: optical biomimetics. Physica B: Condensed Matter, 394, 229-232.

LAU, K. K. S., BICO, J., TEO, K. B. K., CHHOWALLA, M., AMARATUNGA, G. A. J., MILNE, W. I., MCKINLEY, G. H. & GLEASON, K. K. 2003. Superhydrophobic carbon nanotube forests. Nano Letters, 3, 1701-1705.

LEE, A. R., POTTER, F.M. 1938. Some chemical and physical problems of the road and building industries. Journal of the Society of Chemical Industry, 57, 568-578.

LEHTO, A., KOJOLA, H., LOVGREN, T. & LONNBERG, H. 1999. World Patent. 54730.

LINSKENS, H. F. & CRESTI, M. 2000. Pollen-allergy as an ecological phenomenon: a review. Plant Biosystems, 134, 341-352.

LIU, B. & LANGE, F. F. 2006. Pressure induced transition between superhydrophobic states: configuration diagrams and effect of surface feature size. Journal of Colloid and Interface Science, 298, 899-909.

LOSEY, J. E., RAYOR, L. S. & CARTER, M. E. 1999. Transgenic pollen harms monarch larvae. Nature, 399, 214-214.

LUO, C., MENG, F., LIU, X. & GUO, Y. 2006. Reinforcement of a PDMS master using an oxide-coated silicon plate. Microelectronics Journal, 37, 5-11.

MARMUR, A. 2006. Soft contact: measurement and interpretation of contact angles. Soft Matter, 2, 12-17.

MARTINES, E., SEUNARINE, K., MORGAN, H., GADEGAARD, N., WILKINSON, C. D. W. & RIEHLE, M. O. 2005. Superhydrophobicity and superhydrophilicity of regular nanopatterns. Nano Letters, 5, 2097-2103.

MCHALE, G. 2007. Cassie and Wenzel: were they really so wrong? Langmuir, 23, 8200-8205.

MCKENDRY, R., THEOCLITOU, M. E., RAYMENT, T. & ABELL, C. 1998. Chiral discrimination by chemical force microscopy. Nature, 391, 566-568.

MERONEY, R. N., LEITL, B. M., RAFAILIDIS, S. & SCHATZMANN, M. 1999. Wind-tunnel and numerical modeling of flow and dispersion about several building shapes. Journal of Wind Engineering and Industrial Aerodynamics, 81, 333-345.

MEYER, E., HUG, H.J., BENNEWITZ, R. 2004, Scanning Probe Microscopy: The Lab on a Tip: Springer-Verlag, Berlin.

MOCKENHAUPT, B., ENSIKAT, H.-J. R., SPAETH, M. & BARTHLOTT, W. 2008. Superhydrophobicity of biological and technical surfaces under moisture condensation: stability in relation to surface structure. Langmuir, 24, 13591-13597.

MOULDS, M. S. 1990. Australian cicadas, Kensington, N.S.W., New South Wales University Press.

MURATA, H., KOEPSEL, R. R., MATYJASZEWSKI, K. & RUSSELL, A. J. 2007. Permanent, non-leaching antibacterial surfaces - 2: how high density cationic surfaces kill bacterial cells. Biomaterials, 28, 4870-4879.

NARHE, R. D. & BEYSENS, D. A. 2007. Growth dynamics of water drops on a square-pattern rough hydrophobic surface. Langmuir, 23, 6486-6489.

NEVSHUPA, R. A., SCHERGE, M. & AHMED, S. I. U. 2002. Transitional microfriction behavior of silicon induced by spontaneous water adsorption. Surface Science, 517, 17-28.

NOSONOVSKY, M. 2007a. Multiscale roughness and stability of superhydrophobic biomimetic interfaces. Langmuir, 23, 3157-3161.

NOSONOVSKY, M. 2007b. On the range of applicability of the Wenzel and Cassie equations. Langmuir, 23, 9919-9920.

NOSONOVSKY, M. & BHUSHAN, B. 2005. Roughness optimization for biomimetic superhydrophobic surfaces. Microsystem Technologies, 11, 535-549.

NOSONOVSKY, M. & BHUSHAN, B. 2007. Hierarchical roughness makes superhydrophobic states stable. Microelectronic Engineering, 84, 382-386.

OGLETREE, D. F., CARPICK, R. W. & SALMERON, M. 1996. Calibration of frictional forces in atomic force microscopy. Review of Scientific Instruments, 67, 3298-3306.

OLAH, A., HILLBORG, H. & VANCSO, G. J. 2005. Hydrophobic recovery of UV/ozone treated poly(dimethylsiloxane): adhesion studies by contact mechanics and mechanism of surface modification. Applied Surface Science, 239, 410-423.

ORMSTAD, H., GAARDER, P. I. & JOHANSEN, B. V. 1997. Quantification and characterisation of suspended particulate matter in indoor air. Science of the Total Environment, 193, 185-196.

PANCHAGNULA, M. V. & VEDANTAM, S. 2007. Comment on how Wenzel and Cassie were wrong by Gao and McCarthy. Langmuir, 23, 13242-13242.

PARKER, A. R. & LAWRENCE, C. R. 2001. Water capture by a desert beetle. Nature, 414, 33-34.

PARKER, A. R. & TOWNLEY, H. E. 2007. Biomimetics of photonic nanostructures. Nature Nanotechnology, 2, 347-353.

PEREZ-GOODWYN, P. 2009. Anti-Wetting Surfaces in Heteroptera (Insecta). In: GORB, S. N. (ed.) Functional Surfaces in Biology. Berlin: Springer-Verlag

PIKE, J. K., HO, T. & WYNNE, K. J. 1996. Water-induced surface rearrangements of poly(dimethylsiloxane-urea-urethane) segmented block copolymers. Chemistry of Materials, 8, 856-860.

POGODIN, S., HASAN, J., BAULIN, V. A., WEBB, H. K., TRUONG, V. K., NGUYEN, T. H. P., BOSHKOVIKJ, V., FLUKE, C. J., WATSON, G. S., WATSON, J. A., CRAWFORD, R. J. & IVANOVA, E. P. 2013. Biophysical model of bacterial cell interactions with nanopatterned cicada wing surfaces. Biophysical Journal, 104, 835-840.

QUERE, D. 2004. Surface wetting - model droplets. Nature Materials, 3, 79-80.

RALSTON, E. & SWAIN, G. 2011. Can biomimicry and bioinspiration provide solutions for fouling control? Marine Technology Society Journal, 45, 216-227.

RANJIT PRAKASH, A., ADAMIA, S., SIEBEN, V., PILARSKI, P., PILARSKI, L. M. & BACKHOUSE, C. J. 2006. Small volume PCR in PDMS biochips with integrated fluid control and vapour barrier. Sensors and Actuators B: Chemical, 113, 398-409.

REN, X., BACHMAN, M., SIMS, C., LI, G. P. & ALLBRITTON, N. 2001. Electroosmotic properties of microfluidic channels composed of poly(dimethylsiloxane). Journal of Chromatography B: Biomedical Sciences and Applications, 762, 117-125.

SADER, J. E. 1995. Parallel beam approximation for V-shaped atomic force microscope cantilevers. Review of Scientific Instruments, 66, 4583-4587.

SADER, J. E., CHON, J. W. M. & MULVANEY, P. 1999. Calibration of rectangular atomic force microscope cantilevers. Review of Scientific Instruments, 70, 3967-3969.

SADER, J. E. & SADER, R. C. 2003. Susceptibility of atomic force microscope cantilevers to lateral forces: Experimental verification. Applied Physics Letters, 83, 3195-3197.

SCARDINO, A. J. & DE NYS, R. 2011. Mini review: biomimetic models and bioinspired surfaces for fouling control. Biofouling, 27, 73-86.

SCHAER, T. P., STEWART, S., HSU, B. B. & KLIBANOV, A. M. 2012. Hydrophobic polycationic coatings that inhibit biofilms and support bone healing during infection. Biomaterials, 33, 1245-1254.

SCHULTZ, M. P., BENDICK, J. A., HOLM, E. R. & HERTEL, W. M. 2011. Economic impact of biofouling on a naval surface ship. Biofouling, 27, 87-98.

SEDIN, D. L. & ROWLEN, K. L. 2000. Adhesion forces measured by atomic force microscopy in humid air. Analytical Chemistry, 72, 2183-2189.

SHIRTCLIFFE, N. J., MCHALE, G., ATHERTON, S. & NEWTON, M. I. 2010. An introduction to superhydrophobicity. Advances in Colloid and Interface Science, 161, 124-138.

SINNIAH, S. K., STEEL, A. B., MILLER, C. J. & REUTTROBEY, J. E. 1996. Solvent exclusion and chemical contrast in scanning force microscopy. Journal of the American Chemical Society, 118, 8925-8931.

SKLODOWSKA, A., WOZNIAK, M. & MATLAKOWSKA, R. 1999. The method of contact angle measurements and estimation of work of adhesion in bioleaching of metals. Biological Procedures Online, 1, 114-121.

SMITH, J. L. & LEE, K. 2003. Soil as a source of dust and implications for human health. Advances in Agronomy, 80, 1-32.

SNEDDON, I. N. 1965. The relation between load and penetration in the axisymmetric boussinesq problem for a punch of arbitrary profile. International Journal of Engineering Science, 3, 47-57.

STRATAKIS, E., RANELLA, A. & FOTAKIS, C. Biomimetic micro/nanostructured functional surfaces for microfluidic and tissue engineering applications. Biomicrofluidics, 5, 013411.

SUN, M. H., LUO, C. X., XU, L. P., JI, H., QI, O. Y., YU, D. P. & CHEN, Y. 2005. Artificial lotus leaf by nanocasting. Langmuir, 21, 8978-8981.

SUN, M. X., WATSON, G. S., ZHENG, Y. M., WATSON, J. A. & LIANG, A. P. 2009. Wetting properties on nanostructured surfaces of cicada wings. Journal of Experimental Biology, 212, 3148-3155.

SUN, T. L., FENG, L., GAO, X. F. & JIANG, L. 2006. Bioinspired surfaces with special wettability. Accounts of Chemical Research, 39, 487-487.

TADA, H., MANN, S. E., MIAOULIS, I. N. & WONG, P. Y. 1998. Effects of a butterfly scale microstructure on the iridescent color observed at different angles. Applied Optics, 37, 1579-1584.

TAS, N., SONNENBERG, T., JANSEN, H., LEGTENBERG, R. & ELWENSPOEK, M. 1996. Stiction in surface micromachining. Journal of Micromechanics and Microengineering, 6, 385-397.

THIO, B. J. R., LEE, J.-H. & MEREDITH, J. C. 2009. Characterization of ragweed pollen adhesion to polyamides and polystyrene using atomic force microscopy. Environmental Science & Technology, 43, 4308-4313.

THUNDAT, T., WARMACK, R. J., CHEN, G. Y. & ALLISON, D. P. 1994. Thermal and ambient-included deflections of scanning force microscope cantilevers. Applied Physics Letters, 64, 2894-2896.

TOBIN, M. J., PUSKAR, L., HASAN, J., WEBB, H. K., HIRSCHMUGL, C. J., NASSE, M. J., GERVINSKAS, G., JUODKAZIS, S., WATSON, G. S., WATSON, J. A., CRAWFORD, R. J. & IVANOVA, E. P. 2013. High spatial resolution mapping of superhydrophobic cicada wing surface chemistry using synchrotron radiation infrared microspectroscopy. Journal of Synchrotron Radiation. Journal of Synchrotron Radiation, 20, 482-489

TROYNIKOV, O., ASHAYERI, E. & FUSS, F. K. 2011. Tribological evaluation of sportswear with negative fit worn next to skin. Proceedings of the Institution of Mechanical Engineers Part J-Journal of Engineering Tribology, 226, 588-597.

VINCENT, J. F. V. 2008. Biomimetic materials. Journal of Materials Research, 23, 3140-3147.

VINCENT, J. F. V. 2009. Biomimetics - a review. Proceedings of the Institution of Mechanical Engineers Part H-Journal of Engineering in Medicine, 223, 919-939.

VINCENT, J. F. V. & WEGST, U. G. K. 2004. Design and mechanical properties of insect cuticle. Arthropod Structure & Development, 33, 187-199.

VUKUSIC, P. & SAMBLES, J. R. 2003. Photonic structures in biology. Nature, 424, 852-855.

VUKUSIC, P., SAMBLES, J. R. & LAWRENCE, C. R. 2004. Structurally assisted blackness in butterfly scales. Proceedings of the Royal Society of London Series B-Biological Sciences, 271, S237-S239.

WAGNER, P., FURSTNER, R., BARTHLOTT, W. & NEINHUIS, C. 2003. Quantitative assessment to the structural basis of water repellency in natural and technical surfaces. Journal of Experimental Botany, 54, 1295-1303.

WAGNER, T., NEINHUIS, C. & BARTHLOTT, W. 1996. Wettability and contaminability of insect wings as a function of their surface sculptures. Acta Zoologica, 77, 213-225.

WARMACK, R. J., ZHENG, X. Y., THUNDAT, T. & ALLISON, D. P. 1994. Friction effects in the deflection of atomic-force microscope cantilevers. Review of Scientific Instruments, 65, 394-399.

WATSON, G. S. 2001. Quantitative measurements of tip-to-surface interactions in 3 dimensions by atomic force microscopy (AFM) methodology and applications. PhD, Griffith University, Nathan Campus.

WATSON, G. S., BLACH, J. A., CAHILL, C., NICOLAU, D. V., PHAM, D. K., WRIGHT, J. & MYHRA, S. 2004a. Interactions of poly(amino acids) in aqueous solution with charged model surfaces - analysis by colloidal probe. Biosensors and Bioelectronics, 19, 1355-1362.

WATSON, G. S., BROWN, C. L., MYHRA, S., HU, S., ROCH, N. C. & WATSON, J. A. 2006a. 'Patterning' frictional differentiation to a polymer surface by atomic force microscopy. In: CHIAO, J. C., DZURAK, A. S., JAGADISH, C. & THIEL, D. V. (eds.) Device and Process Technologies for Microelectronics, MEMS, and Photonics IV. Bellingham: Spie-Int Soc Optical Engineering.

WATSON, G. S., BROWN, C. L., MYHRA, S., ROCH, N. C., HU, S. & WATSON, J. A. 2006b. 'Patterning' frictional differentiation to a polymer surface by atomic force microscopy - art. no. 60371B. In: CHIAO, J. C., DZURAK, A. S., JAGADISH, C. & THIEL, D. V. (eds.) Device and Process Technologies for Microelectronics, MEMS, and Photonics IV. Bellingham: Spie-Int Soc Optical Engineering.

WATSON, G. S., CRIBB, B. W. & WATSON, J. A. 2010a. How micro/nanoarchitecture facilitates anti-wetting: an elegant hierarchical design on the termite wing. Acs Nano, 4, 129-136.

WATSON, G. S., CRIBB, B. W. & WATSON, J. A. 2010b. The role of micro/nano channel structuring in repelling water on cuticle arrays of the lacewing. Journal of Structural Biology, 171, 44-51.

WATSON, G. S., CRIBB, B. W. & WATSON, J. A. 2010c Experimental determination of the efficiency of nanostructuring on non-wetting legs of the water strider. Acta Biomaterialia, 6, 4060-4064.

WATSON, G. S., CRIBB, B. W. & WATSON, J. A. 2011a. Contrasting micro/nano architecture on termite wings: two divergent strategies for optimising success of colonisation flights. PLoS ONE, 6, e24368.

WATSON, G. S., DINTE, B. P., BLACH-WATSON, J. A. & MYHRA, S. 2004b. Friction measurements using force versus distance friction loops in force microscopy. Applied Surface Science, 235, 38-42.

WATSON, G. S., DINTE, B. P., BLACH, J. A. & MYHRA, S. 2002. Demonstration of atomic scale stick-slip events stimulated by the force versus distance mode using atomic force microscopy. Journal of Physics D-Applied Physics, 35, 2066-2074.

WATSON, G. S., HU, S., CRIBB, B. W., MYHRA, S., BROWN, C. L. & WATSON, J. A. 2008a. Micro and nano-structures found on insect wings - designs for minimising adhesion and friction. 2nd International Conference on Advanced Nano Materials. Aveiro, Portugal Journal of Nanoscience and Nanotechnology.

WATSON, G. S., MYHRA, S., CRIBB, B. W. & WATSON, J. A. 2008b. Putative functions and functlona efficiency of ordered cuticular nanoarrays on insect wings. Biophysical Journal, 94, 3352-3360.

WATSON, G. S., MYHRA, S., CRIBB, B. W. & WATSON, J. A. 2008c. Putative functions and functlonal efficiency of ordered cuticular nanoarrays on insect wings. Biophysical Journal, 94, 3352-3360.

WATSON, G. S., MYHRA, S., WATSON, J. A. & CRIBB, B. W. 2007. Nanoscale Structure and Properties of Microbial Cell Surfaces. Nova Publishing.

WATSON, G. S. & WATSON, J. A. 2004. Natural nano-structures on insects - possible functions of ordered arrays characterized by atomic force microscopy. Applied Surface Science, 235, 139-144.

WATSON, G. S. & WATSON, J. A. 2008. Quantitative Measurements of Nano Forces Using Atomic Force Microscopy (AFM): Quantifying Nano Forces in Three-Dimensions Using AFM: Applications in the Biological, Physical and Chemical Sciences, VDM Publishing.

WATSON, J. A 2005, 'Micro/nano-physical and chemical architecture of polymer surfaces by ultra-violet exposure and scanning probe microscopy', Ph.D. thesis, Griffith University. Brisbane.

WATSON, J. A., BROWN, C. L., MYHRA, S. & WATSON, G. S. 2006c. Two-dimensional stick-slip on a soft elastic polymer: pattern generation using atomic force microscopy. Nanotechnology, 17, 2581-2589.

WATSON, J. A., CRIBB, B. W., HU, H. S. & WATSON, G. S. 2011b. A dual layer hair array of the brown lacewing: repelling water at different length scales. Biophysical Journal, 100, 1149-1155.

WATSON, J. A., HU, H. M., CRIBB, B. W. & WATSON, G. S. 2011c. Anti-wetting on insect cuticle - Structuring to minimise adhesion and weight. In: PRAMATAROVA, L. (ed.) On Biomimetics. croatia: INTECH.

WEI, P. J., SHEN, Y. X. & LIN, J. F. 2009. Characteristics of water strider legs in hydrodynamic situations. Langmuir, 25, 7006-7009.

WEI, Z. & ZHAO, Y. P. 2007. Growth of liquid bridge in AFM. Journal of Physics D-Applied Physics, 40, 4368-4375.

WENZEL, R. N. 1936. Resistance of solid surfaces to wetting by water. Industrial and engineering chemistry, 28, 988-994.

WHITE, J. H. 1951. Observations on the life history and biology of *Tipula lateralis* Meig. . Annals of Applied Biology, 38, 847-858.

WIER, K. A. & MCCARTHY, T. J. 2006. Condensation on ultrahydrophobic surfaces and its effect on droplet mobility: ultrahydrophobic surfaces are not always water repellant. Langmuir, 22, 2433-2436.

WILLIAMS, J. M., HAN, T. J. & BEEBE, T. P. 1996. Determination of single-bond forces from contact force variances in atomic force microscopy. Langmuir, 12, 1291-1295.

WOODWARD, I., SCHOFIELD, W. C. E., ROUCOULES, V. & BADYAL, J. P. S. 2003. Super-hydrophobic surfaces produced by plasma fluorination of polybutadiene films. Langmuir, 19, 3432-3438.

XIAO, X. D. & QIAN, L. M. 2000. Investigation of humidity-dependent capillary force. Langmuir, 16, 8153-8158.

YEBRA, D. M., KIIL, S. & DAM-JOHANSEN, K. 2004. Antifouling technology - past, present and future steps towards efficient and environmentally friendly antifouling coatings. Progress in Organic Coatings, 50, 75-104.

YING, Z. C., REITSMA, M. G. & GATES, R. S. 2007. Direct measurement of cantilever spring constants and correction for cantilever irregularities using an instrumented indenter. Review of Scientific Instruments, 78, 063708.

YLIPANULA, E. & RANTIOLEHTIMAKI, A. 1995. Birch-pollen antigenic activity of settled dust in rural and urban homes. Allergy, 50, 303-307.

ZHANG, F. X. & LOW, H. Y. 2007. Anisotropic wettability on imprinted hierarchical structures. Langmuir, 23, 7793-7798.

ZHENG, Y., GAO, X. & JIANG, L. 2007. Directional adhesion of superhydrophobic butterfly wings. Soft Matter, 3, 178-182.

ZINKL, G. M., ZWIEBEL, B. I., GRIER, D. G. & PREUSS, D. 1999. Pollen-stigma adhesion in Arabidopsis: a species-specific interaction mediated by lipophilic molecules in the pollen exine. Development, 126, 5431-5440.

11 APPENDICES

OTHER PUBLICATIONS

Multi-Functional Insect Cuticles: Informative Designs for Man-Made Surfaces

Hsuan-Ming S Hu, Jolanta A Watson, Bronwen W Cribb and Gregory S Watson

Abstract**—**Biomimicry has many potential benefits as many technologies found in nature are superior to their man-made counterparts. As technological device components approach the micro and nanoscale, surface properties such as surface adhesion and friction may need to be taken into account. Lowering surface adhesion by manipulating chemistry alone might no longer be sufficient for such components and thus physical manipulation may be required. Adhesion reduction is only one of the many surface functions displayed by micro/nano-structured cuticles of insects. Here, we present a mini review of our understanding of insect cuticle structures and the relationship between the structure dimensions and the corresponding functional mechanisms. It may be possible to introduce additional properties to material surfaces (indeed multi-functional properties) based on the design of natural surfaces.

Keywords**—**Biomimicry, micro/nanostructures, self-cleaning surfaces, superhydrophobicity

H. S. Hu is with the School of Pharmacy and Molecular Sciences, James Cook University, Townsville 4811 Australia (fax: +61 7 4781 6078; e-mail: simon.hu@my.jcu.edu.au).

J. A. Watson is with the School of Pharmacy and Molecular Sciences, James Cook University, Townsville 4811 Australia (e-mail: jolanta.watson@jcu.edu.au).

B. W. Cribb is with the Centre for Microscopy and Microanalysis and School of Integrative Biology, The University of Queensland, St. Lucia 4072 Australia (e-mail: b.cribb@uq.edu.au).

G. S. Watson is with the School of Pharmacy and Molecular Sciences, James Cook University, Townsville 4811 Australia (e-mail: gregory.watson1@jcu.edu.au).

Micro and nanostructures found on insect wings – designs for minimising adhesion and friction

Gregory S. Watson* and Jolanta A. Watson

School of Pharmacy and Molecular Sciences,
James Cook University,
Townsville, QLD 4811, Australia
Fax: +61 7 4781 6078
E-mail: greg.watson@jcu.edu.au
E-mail: jola.watson@jcu.edu.au
*Corresponding author

Simon Hu and Christopher L. Brown

School of Biomolecular and Physical Science,
Griffith University, Kessels Road,
Nathan, QLD 4111, Australia
Fax: 61 7 3735 7656
E-mail: simon.hu@student.griffith.edu.au
E-mail: c.l.brown@griffith.edu.au

Bronwen W. Cribb

Centre for Microscopy and Microanalysis and
School of Integrative Biology,
The University of Queensland,
St. Lucia, QLD 4072, Australia
Fax: +61 7 3346 3993
E-mail: b.cribb@uq.edu.au

Sverre Myhra

Begbroke Science Park,
The University of Oxford,
Sandy Lane, Yarnton, OX5 1PF, UK
Fax: +44 18 6584 8790
E-mail: sverre.myhra@materials.ox.ac.uk

Abstract: Adhesion and friction have been measured on insect wings where contamination (water and/or contaminating particles) can potentially have a detrimental effect on their flight capabilities or daily functioning. Adhesional forces as low as 2 nN were recorded in air for particles with radii of 10–15 nm, and 20 nN for particles of 31 mm radius. The effective coefficients of friction were in the range of 0.01 to 0.10. The low adhesion and frictional values

Please cite this article in press as: Watson et al., A Dual Layer Hair Array of the Brown Lacewing: Repelling Water at Different Length Scales, Biophysical Journal (2011), doi:10.1016/j.bpj.2010.12.3736

A Dual Layer Hair Array of the Brown Lacewing: Repelling Water at Different Length Scales

Jolanta A. Watson,[†]* Bronwen W. Cribb,[‡] Hsuan-Ming Hu,[†] and Gregory S. Watson[†]
[†]School of Pharmacy and Molecular Sciences, James Cook University, Townsville, Queensland, Australia;
and [‡]Centre for Microscopy & Microanalysis and School of Biological Sciences, The University of Queensland, St. Lucia, Queensland, Australia

ABSTRACT Additional weight due to contamination (water and/or contaminating particles) can potentially have a detrimental effect on the flight capabilities of large winged insects such as butterflies and dragonflies. Insects where the wing surface area-body mass ratio is very high will be even more susceptible to these effects. Water droplets tend to move spontaneously off the wing surface of these insects. In the case of the brown lacewing, the drops effectively encounter a dual bed of hair springs with a topographical structure which aids in the hairs resisting penetration into water bodies. In this article, we demonstrate experimentally how this protective defense system employed by the brown lacewing (*Micromus tasmaniae*) aids in resisting contamination from water and how the micro- and nanostructures found on these hairs are responsible for quickly shedding water from the wing which demonstrates an active liquid-repelling surface.

This publication has been removed due to copyright restrictions

Submitted September 6, 2010, and accepted for publication December 20, 2010.

*Correspondence: jolanta.watson@jcu.edu.au

Editor: Levi A. Gheber.

0006-3495/11/02/0001/7 $2.00

doi: 10.1016/j.bpj.2010.12.3736

‘Patterning’ frictional differentiation to a polymer surface by atomic force microscopy

Gregory S. Watson[a], Christopher L. Brown[a], Sverre Myhra[b], Nicolas C. Roch[a], Simon Hu[a], Jolanta A. Watson[a]

[a]Nanoscale Science and Technology Centre, School of Science, Griffith University; Nathan, Queensland 4111, Australia

[b]Oxford University Begbroke Science Park, Yarnton OX5 1PF, UK

ABSTRACT

The surface structure and chemistry of polymers affect their functionality for a great range of applications in areas as diverse as biosensors, corrosion protection, semiconductor processing, biofouling, tissue engineering and biomaterials technology. Some of those applications require purposeful tailoring of laterally differentiated regions (e.g., array structures for multi-channel/multi-analyte biosensors and patterning for promotion of selective adhesion of cells/proteins). While such tailoring is currently taking place on the μm-scale, it is likely in the future to progress into the nm-regime. Attachment of biological moieties at surfaces and interfaces has been shown to be highly dependant on local chemistry at the intended site of attachment. Additionally, the local molecular-scale geometry may promote or hinder attachment events, as in the case of biofilms. To date, however, the effect of frictional properties of surfaces for chemical and biomolecular attachment is a much less understood phenomenon.

In this study we show controlled patterning of a polymer surface (polydimethylsiloxane (PDMS)) arising from manipulation by Atomic Force Microscopy (AFM). PDMS is a bio-active/selective polymer having a broad range of applications, such as biomedical devices, molecular stamps, hydraulic fluid devices and in soft lithography. The polymer surface has been selectively altered by high speed scanning in order to generate regions on the surface that exhibit differentiated frictional properties. By altering the loading force, scan width, and area of the AFM probe-to-polymer contact it is possible to produce a variety of detailed and complex patterns with frictional contrast, including anisotropic frictional gradients on the polymer surface. The controlled manipulation of the polymer surface can be carried out on the micro-, meso- and nano-scale.

Keywords: Atomic force microscopy, PDMS, Stick-Slip, Polymer, Friction, Manipulation

1. INTRODUCTION

Precise manipulation leading to laterally differentiated regions on polymeric materials is required for a range of applications/devices. Patterning surfaces will hinder or promote adhesion of various (bio)chemicals[1-3]. Ion beam sputtering, laser ablation, chemical etching and micro-ablation are just some of the well-established group of technologies collectively referred to as micro-machining. Scanning probe microscopy (SPM) has now become an addition to the variety of tools available. While some technologies such as chemical etching and ion beam sputtering rest on a firm scientific basis, the underlying science is much less satisfactory in the case of mechanical manipulation by SPM methods.

Current explanatory models for tip-induced manipulation of polymer surfaces are in their infancy. Earlier studies have generally been based on insight gained from unrelated materials[4-9] with some studies investigating polymer materials scanned over reasonably small scan ranges (≤ 5×5 μm) with results showing polymer bundles forming as a result of action by the AFM probe[10-14]. The principal objective in this paper is to develop an understanding of tip-induced manipulation of a soft elastic polymer, Poly(dimethylsiloxane), (PDMS), with a focus on the directional response of the AFM probe during manipulation over 10 and 20 μm^2 scan areas.

PDMS is now routinely used in a wide range of patterning and bio-chemical isolation and biomedical applications[15-19], and has a multitude of potential applications including insulation and anti-fouling coatings[20-22]. It offers a range of useful physical, mechanical and chemical properties including transparency, surface hydrophobicity, constant and high ductility over a wide range of temperatures, low toxicity, high electrical resistance, long-term stability and flexibility[23]. PDMS is also used in soft lithography, which is of particular relevance to this study. The fabrication and use of micro/nano stamps and fluidic channels using PDMS material has been demonstrated in a number of studies (e.g., [16, 24-26]). An understanding of the tribological properties and lithographic outcomes from AFM manipulation of PDMS surfaces is a necessary precursor for further technological exploitation.

2. EXPERIMENTAL SECTION

2.1. Specimen materials

PDMS (Sylgard®-184) was supplied by Dow Corning as a two part silicone elastomer. The base and curing agent were mixed at a 10:1 weight ratio, spin-coated onto atomically flat silicon wafer substrates and cured in an ambient environment (25°C and 55% relative humidity) for 48 hours prior to any analysis or manipulation. The average thickness of the polymer was ca. 2 μm.

2.2. AFM instrumentation

The work was carried out on a ThermoMicroscope TMX-2000 Explorer, based on the detection of tip-to-surface forces through the monitoring of the optical deflection of a laser beam incident on a force-sensing/imposing lever. Scanning with the instrument is implemented by probe/lever being in motion while the stage assembly remains stationary. In order to cover the scales of lateral and topographical differentiation, a 130×130 μm^2 tripod scanner (*z*-range of 9.7 μm) was used. The analyses were carried out under air-ambient conditions (20-23°C and 60-70 % relative humidity).

2.3. Probes

The probe consists of a lever with an integral conical tip attached at its free end. The tip-to-surface contact area defines the interaction volume, whereby information such as topography, strength of in-plane and out-of-plane forces is extracted. The contact area also represents the point at which purposeful manipulation is effected. Many polymers can be considered as 'soft' objects. Therefore the imposition of forces at the point of contact will cause deformation and indentation, and an increase in contact area. Thus it is necessary to use levers with force constants, k_N, ≤ 0.1 nNnm^{-1} in order to improve resolution and to avoid surface modification. Levers with k_N ≥ 4 nNnm^{-1} enable surface manipulation.

The characteristics of probes employed in the present study are listed in table 1. Beam-shaped levers were used in order to ensure that only simple bending modes needed to be considered. The data for radius of curvature at the tip apex, R_{Tip}, aspect ratio (opening half angle) of the tip, A_r, and surface chemistry (<10nm, <10° and native Si-oxide film, respectively) are summarized from the suppliers' specifications. The values of the force constant for normal deflection, k_N, of individual probes were determined from the resonance method described by Cleveland *et al* [27], and the torsional, k_T, and longitudinal, k_L, force constants were calculated from the standard expressions for a long and thin lever, described by Gibson *et al* [28].

Table 2. Probe specifications.

Probe	k_N (nNnm^{-1})	k_T (nNnm^{-1})	k_L (nNnm^{-1})
A	0.035	7.2	4.7
B	6.8	150	95
C	7.1	155	100
D	0.1	15	10
E	10.3	220	145
F	0.07	11	7.4
G	14	300	200

2.3. Imaging
Under normal topographical imaging conditions, the 'over-scan' along the fast scan direction, is typically ca. 25%, and is a general characteristic of SPM instruments. This over-scan feature is intended as a means of removing the static friction feature from images. Thus for 20×20 and 10×10 μm^2 fields of view there were 4 and 2.56 μm over-scans, respectively, in the fast scan direction. The over-scan must be taken into account in this study due to the manipulation taking place along the entire fast scan trace. The outcome was then imaged over a larger field of view with a soft lever. As a result the imaged areas are quoted as 24×20 μm^2 and 12.56×10 μm^2. Imaging of the manipulated regions on the polymer was carried out immediately after alteration of the surface.

3. RESULTS AND DISCUSSION

3.1. Surface topography and tip indentation
A contact mode topographical image of a freshly spun PDMS surface is shown in Figure 1(a) in 3-dimensional representation. In order to evaluate the polymer surface topography with minimal surface alteration the image was obtained with probe 'A' in table 1, with a force loading < 20 nN. Subsequent scanning of a larger field of view than the previously imaged region, revealed no discernible surface changes in characteristics/relief and no build up of displaced material at the scan edges. The surface roughness for a 1×1 μm^2 region was 0.5 ± 0.1 nm.

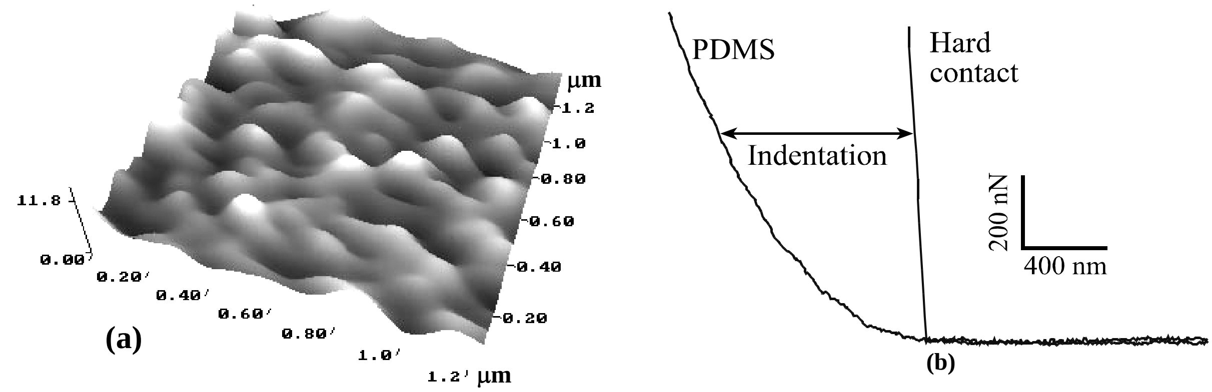

Figure 1. (a) Surface topography of a freshly spun PDMS surface shown in 3-D format. The contact mode image was obtained with probe 'A' at a force-loading of < 20 nN. (b) Representative f-d curves obtained with probe 'B' for an incompressible surface, polished Si, and a PDMS surface. The latter curve shows the extent of tip indentation of the polymer. Tip penetration/indentation of ca. 950 nm is evident for an imposed force of ca. 600 nN. Subsequent imaging of the field of view after f-d analysis revealed total elastic recovery, within the resolution of imaging.

Figure 1(b) shows the approach half-cycles of two representative force versus distance (f-d) curves obtained on a 'hard' surface (clean silicon wafer) and a PDMS surface. The f-d data were obtained with probe 'B' (with a spring constant approximately two hundred times greater than probe 'A'). The shape of the f-d curve taken on the PDMS surface shows significant out-of-plane deformation of the polymer. At a force of 600 nN, there was an indentation, Δz, of ca. 950 nm. Using a model by Sneddon for deformation by a conical tip as a function of sample indentation[29], Young's Modulus for the PDMS material was found to be in the range 3.1 - 7.6 × 10^5 Pa. The results are in good agreement with the values quoted in the literature[30-32].

3.2. Stick-slip behaviour
The PDMS surface was scanned at moderately high force loadings in order to evaluate the extent of polymer manipulation. The field of view was generated with a resolution of 300 lines. The velocity in the fast scan direction was 125 μms^{-1}, and the raster over a field of 24×20 μm^2 was carried out in the constant normal force mode (with probe 'C'). The applied normal force was 950 nN and the fast scan direction (*x*-axis, 24 μm) was perpendicular to the long axis of the lever as shown in the inset in figure 2(a).

A lateral force image, shown in figure 2 (a), was obtained with a soft lever (probe 'A') which was used to scan after the manipulation of the PDMS surface using a stiff lever (probe 'B'). The channel depth and width, as revealed by topographical images (not shown here), was found to be 160-260 nm and 0.4-0.6 μm, respectively. The lateral force image clearly shows the series of horizontal channels and sloping lines connecting successive channels (arrows) showing the stick and slip mechanism, respectively, in the slow scan direction. The discontinuities/channels have an average spacing of approximately 2.3 μm. The location in the slow scan direction is incremented every two scanning lines in the fast scan direction in order to generate the raster pattern. Thus the scanning stage movement for a 20 μm image (slow scan direction) incorporates 300 × 2 scan lines spaced 66.67 nm apart. Thus there will be ca. 69 scan lines for a 2.3 μm stage-path along the slow scan direction, equal to the number of traverses per trough.

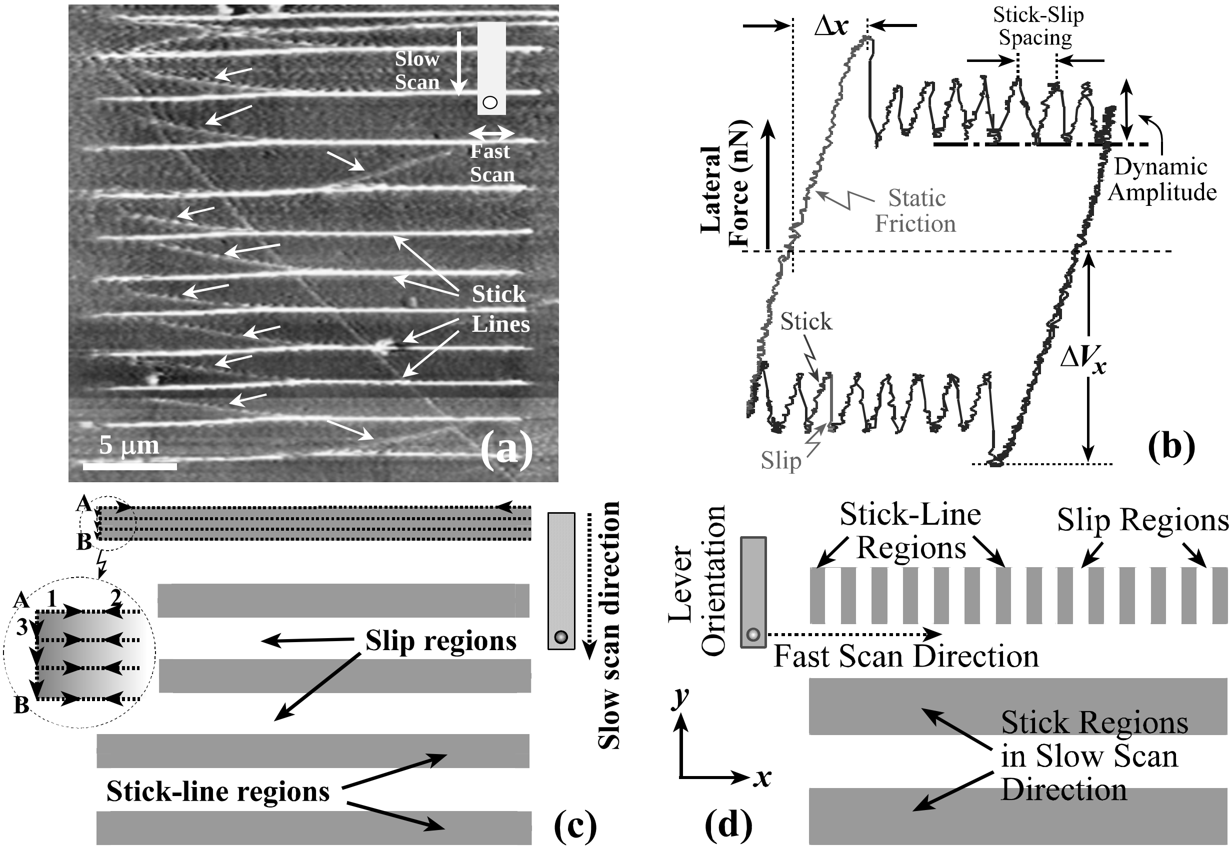

Figure 1. (a) Lateral force image of a manipulated region using a soft lever (probe ‘G’, table 1) showing the resulting stick lines and the path taken by the tip during the slip stage (arrows). (b) Friction loop obtained using probe ‘H’ demonstrating stick-slip behaviour in the fast scan direction. ΔV_x represents the L-R detector signal with Δx showing the lateral (in-plane) displacement of the stage. (c) A diagrammatic representation of the tip sticking, A to B (raster motion from 1 to 3 within a single grey band (channel) shown in the inset), then slipping (white band) through to the next grey region. (d) Schematic representation of the fast scan stick-slip motion of the lever.

Figure 2 (b) shows a representative friction loop acquired during the middle of a manipulating scanning cycle within a stick line in the fast scan direction (probe ‘C’, table 1). The static friction is the regime in which the motion of the tip and sample are coupled. The amplitude and spacing of the stick-slip features are also defined. The friction loop clearly reveals stick-slip behaviour in the fast scan direction during the acquisition of an image and manipulation of the polymer. Figure 2(c) shows a diagrammatic representation of the manipulation event. The tip begins its raster motion at point A moving towards point B. This is illustrated in the inset whereby the raster motion proceeds from 1 to 3 within a single grey band (channel). The tip becomes trapped within the grey horizontal bands which represents one full stick cycle. As a consequence, only a small spatial region along the slow scan direction is imaged. Significant polymer deformation is evident during this process due to the stick point being dragged along in response to the longitudinal/buckling force imposed by the lever. Figure 2 (d) shows a schematic representation of the stick-slip behaviour in the fast scan direction similar to that shown in figure 2 (c) for the stick-slip process in the slow scan direction. As the tip moves across the surface (x-direction) it becomes embedded at the first stick point until a point of instability is reached between the restoring force of the deformed polymer and the torsional force of the tip. This instability causes the tip to be released thereby jumping to its next stick position, repeating the cycle in both the forward and reverse directions of travel.

3.3. Loading Force Dependence

An investigation of loading force dependence on lateral force, channel spacing and depth was conducted. Figure 3 (a) shows a linear dependence of the lateral force on various force loadings using a stiff lever (probe 'D'). At higher force loadings the elastic limit of a softer surface will be exceeded thus resulting in plastic deformation. Trends between loading force and depth (right axis) and spacing (left axis) is shown in (b). The depth and channel spacing increases with loading force due to the tip being embedded deeper into the surface, causing an increase in contact area, greater trapping and elastic deformation of the polymer (both in the x and y directions) The greater in-plane elastic force causes an increase in the spacing.

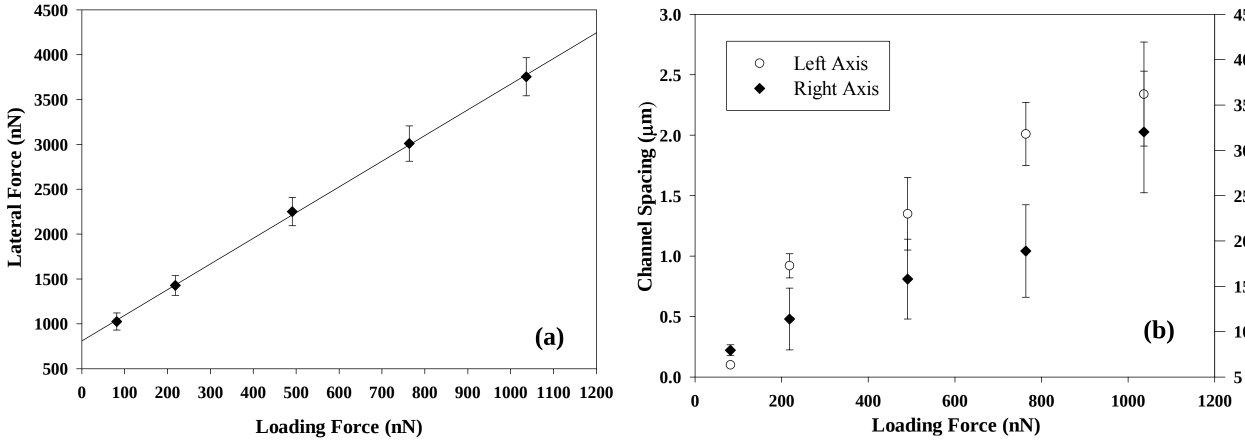

Figure 3. Dependence of lateral force (R = 0.999) (a), channel depth (R = 0.963) (right axis) and spacing between successive channels (left axis) (b), on loading force using probe 'D' defined in table 1.

3.4. Scan Speed Dependence

A study of the dependence of scan speed on loading force, dynamic stick-slip amplitude (defined in figure 2 (b)), number of stick-slip features and their spacing has also been undertaken. Figure 4 (a) shows representative data demonstrating a clear dependence of lateral force on the scan speed in the fast scan direction (left axis). As the speed increases, there is an increase in contact between the sides of the polymer surface and the leading face of the tip, resulting in an increase in lateral force in the slow scan direction. Also, the probe may be increasingly restrained by the polymer. A similar trend occurs in the fast scan direction, whereby the dynamic stick-slip amplitude (right axis in figure 4 (a)) increases. The representative data presented in (b) shows a decrease in the number of stick-slip features (right axis) and an increase in the spacing between them (defined in figure 2 (b)) (left axis).

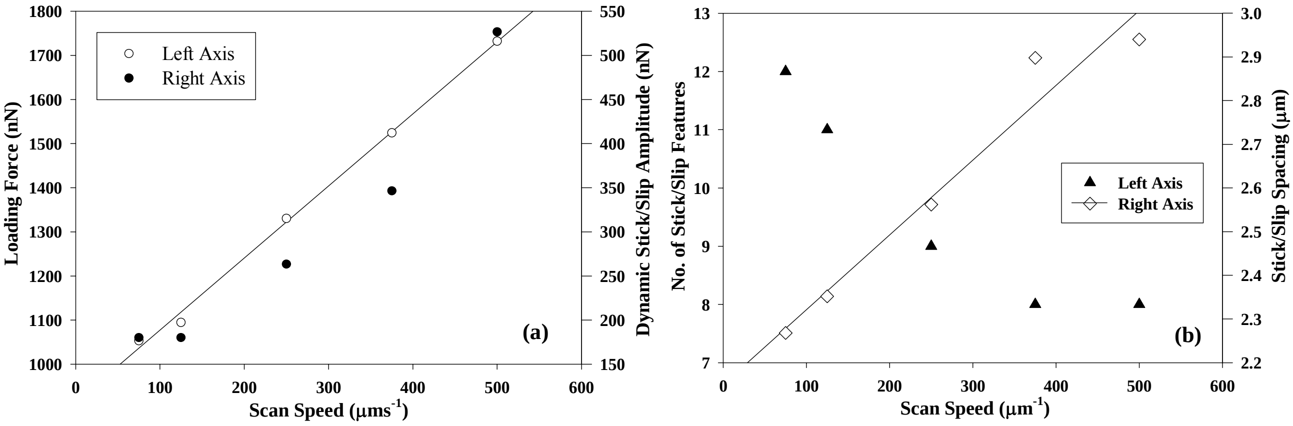

Figure 4. (a) Graphs showing a clear lateral force (R = 0.997) (left axis) and dynamic stick-slip amplitude dependence (right axis) on the increase in scan speed. (b) Dependence of the number of stick/slip features (right axis) and their spacing (left axis) on scan speed (R = 0.957). Data obtained using probe 'A' in table 1.

3.5. Image Resolution Dependence

The dependence of the number of channels, spacing and depth on image resolution has also been studied. Table 2 below indicates from experiments that the higher the resolution, the greater the number of times the tip traverses within a single channel before slipping to the next stick point.

Table 2. Spacing between consecutive rasters (one raster = forward and reverse), and number of rasters per channel (×2 for the forward and reverse motion) for 10×10 μm^2 image

Resolution	One raster spacing (nm)	# of rasters / trough (×2)
50×50	200	6
100×100	100	22
300×300	33	132
400×400	25	156
500×500	20	196

Figure 5 shows the general trends observed as the resolution was gradually increased, using probe 'E' and 'B' during and after manipulation, respectively. The loading force of 465 nN during manipulation, scan speed of 125 μms^{-1} and field of view of 10×10 μm^2 were all kept constant for consistency. The results show an increase in channel spacing and depth after a resolution of 100 lines.

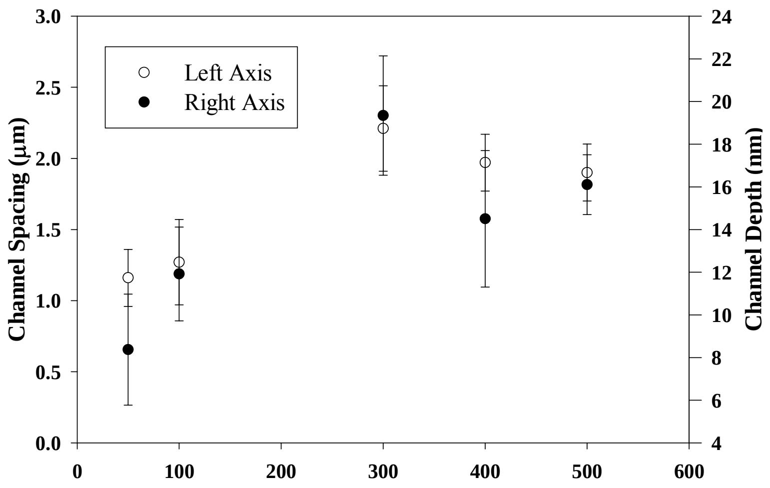

Figure 5. Representative graph showing the spacing between channels (left axis) and their depth (right axis) increasing with an increase in image resolution.

Figure 6 shows the general features of the stick-slip regime for high and low resolution image lithography. At a low resolution (e.g., 50×50 or 100×100 lines), the incremental movement of the tip in the *y*-direction is greater (200 nm at 50×50 resolution) than that at a high resolution (66 nm at 300×300 resolution). This results in a lower number of rasters within a channel allowing the tip apex to be removed from the stick region. As the resolution increases, the number of rasters within a trough increases allowing the tip apex to become embedded further into the polymer surface, trapping the tip more efficiently, and providing a stronger restraining stick region. This results in the reduction in the number of troughs created over a scan area.

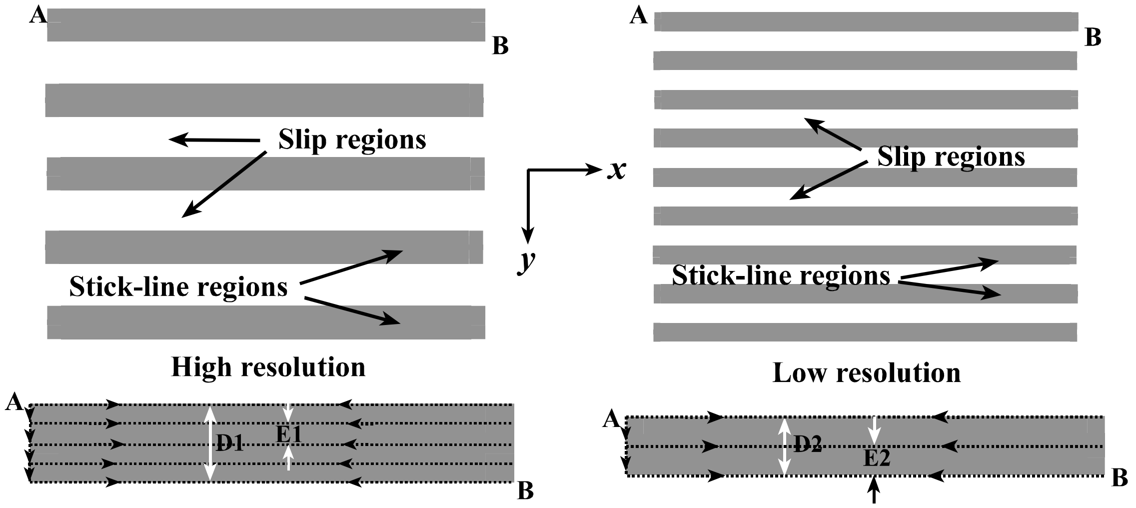

Figure 5. Schematic representation of the general stick-slip features for high and low resolution image lithography. At a high resolution, the raster increment, E1, is lower than the raster increment, E2, at a low resolution. The stick region is also greater at a high resolution, that is, D1 > D2.

3.6. Homogeneous frictional architecture

By altering the loading force it is possible to induce or prevent the stick-slip phenomenon. Figure 6 (a) shows a friction force image of a manipulated region on the PDMS surface. The manipulation was carried out at high force loading (ca. 600 nN) in order to induce stick-slip on the polymer surface, and thus create evenly spaced channels, as previously described in sections 3.2 – 3.5. Figure 6 (b) shows a friction force image resulting from a lower force loading of ca. 200 nN. The outcome is a uniform, laterally differentiated region. The two distinctly different outcomes shown in figure 6(a) and (b) demonstrate the ability to form homogeneous and inhomogeneous frictional surface profiles using manipulative atomic force microscopy.

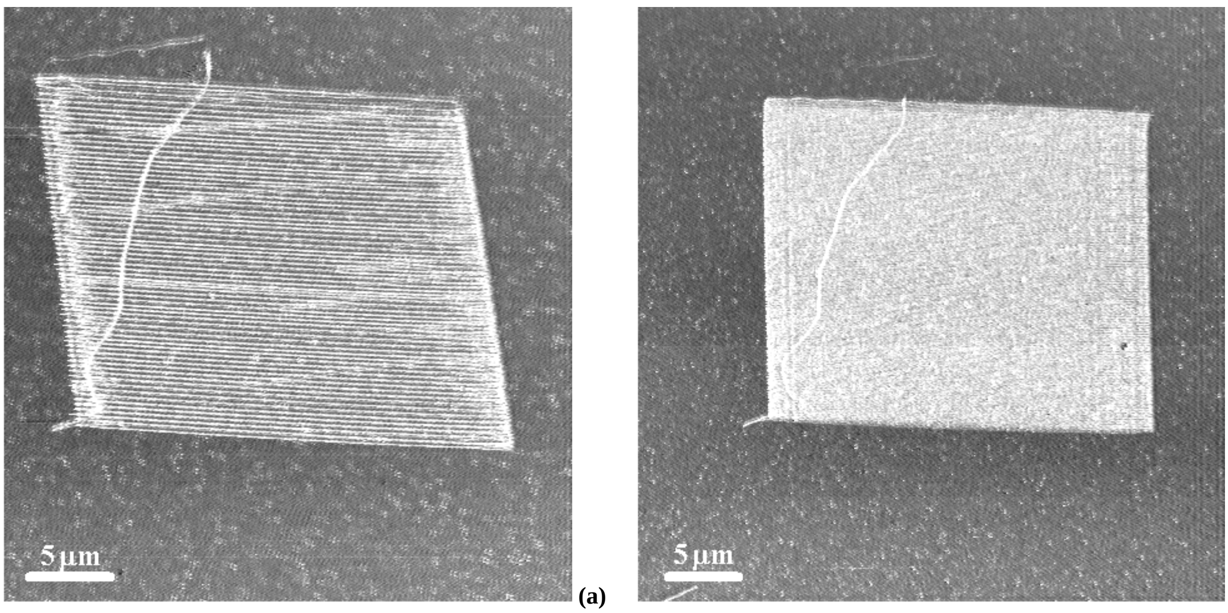

(a) **(b)**

Figure 6 – (a) Friction force image of a manipulated region using a force loading of ca. 600 nN resulting in uniformly spaced channels due to stick-slip. (b) Friction force image of a manipulated region using a lower force loading (ca. 200 nN) showing a uniform laterally differentiated region.

By altering the scan angle, it is possible to produce features with various orientations. Figure 7 shows a topographical (a) and a friction force map (b) showing details of channels with sub-μm spacing created as a result of the stick-slip phenomenon. The channels were scanned 45° to each other, thus creating precise mesh-like patterns. The line profile in (c), corresponding to the image in (a), shows an average depth of the channels to be ca. 15 nm.

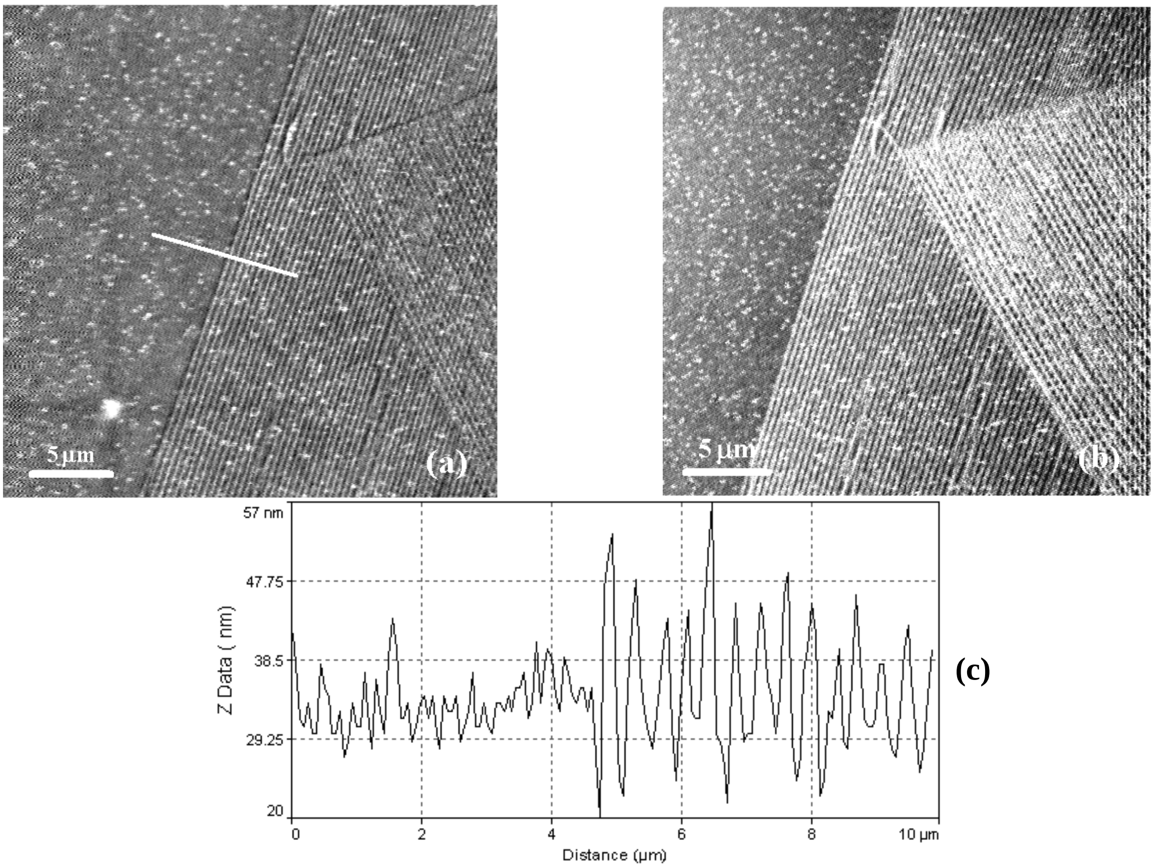

Figure 7 – (a) Topographical and (b) lateral force images of two overlapping areas showing details of channels created at varying orientations. The line profile in (c), corresponding to the topographical image in (a), shows the depth of channels to be ca. 15 nm. The frictional force image (b) shows a higher frictional force within the channels.

Frictional force images in figure 8 show three manipulated regions within a single field of view, with the corresponding friction loops revealing higher friction on the manipulated regions. Squares A and B are the result of three and four repetitive rasters, respectively, using a high spring constant lever. The corresponding friction loops show the difference in friction in the two squares, i.e., ΔF_F of square A is lower than that of square B. Square C is the result of a single raster over a 20×20μm^2 area, with a subsequent raster over a 10×10μm^2 area (square D), creating a frictional 'tier'. The RMS surface roughness of the manipulated region on square B was found to be higher (ca 2.8 nm) than that of the surrounding PDMS surface (ca 1.8 nm), for a 4×4 μm^2 area.

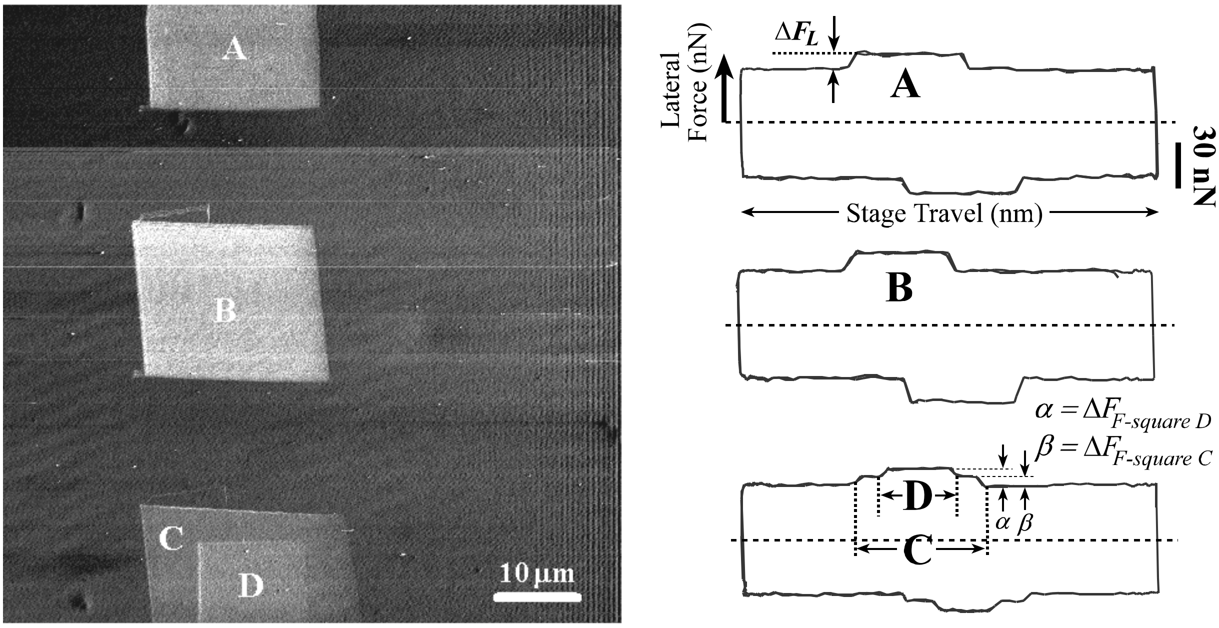

Figure 8 – A frictional force image (left) showing four square regions shows the dependence on the number of successive rasters; three for square A, four for square B, and one for square C. Square D is a result of an additional raster over square C once. The corresponding friction loops (right) demonstrate that friction increased with the number of repetitive rasters. The slight distortion in the images is due to thermal drift.

Figure 9 shows a variety of frictional architectures created on the PDMS surface by altering the loading force, scan size and the number of successive scans. The image shows overlapping of both homogeneous and inhomogeneous features. Squares A, B, D and E are created by maintaining a force loading below the point at which stick-slip is induced, thereby creating uniformly frictionally altered regions. Several squares overlap creating 'tiers' of changing friction, e.g., squares A, B and C. Stick-slip effects are apparent on square C.

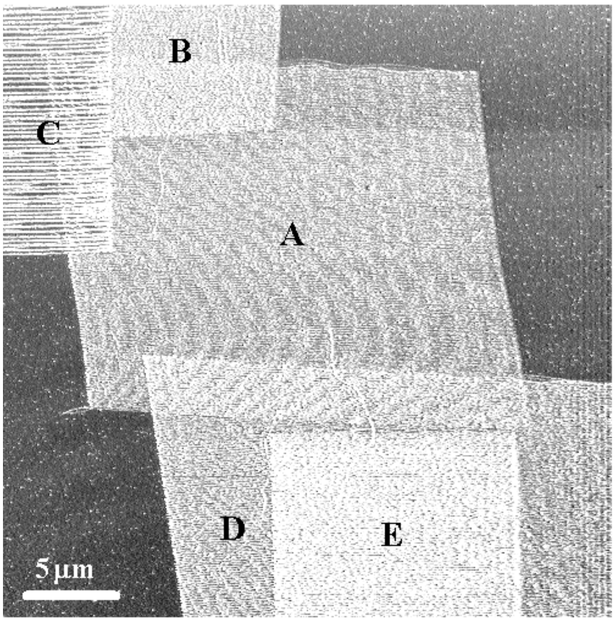

Figure 9 – Frictional force images showing the degree of freedom in feature formation on the polymer surface.

4. CONCLUSION

Stick-slip effects have been observed in previous AFM studies; these have, in most cases, been restricted to atomic and molecular scales[33-35]. In the case of AFM-based manipulation of polymers the focus has generally been on establishing the dependence on loading force[1, 6, 10, 36, 37], and/or temperature and number of rasters[12-14]. The present results for PDMS show, in particular, friction loop acquisition and analysis during manipulation, and describe in some detail the response of the AFM probe when it is in dynamic contact with a soft elastic polymer surface.

Surface alteration has been correlated with the response of the probe to linear motion and to lateral forces imposed by the relaxing polymer. An explanatory model was constructed with the aid of friction loop analysis, whereby the tip not only sticks and slips within the trough, in the fast scan direction, but also from one trough to another, in the slow scan direction. The process was consistently reproduced with levers with a spring constant of > 1 N/m. The in-plane relaxation of the surface in response to tip-induced in-plane forces, dynamic stick-slip amplitude and stick-slip spacings have also been examined.

By altering the scan conditions and probe parameters it is possible to carry out frictional patterning on a polymer surface (in this case PDMS) at the micro and nano scales. The frictional patterning can be carried out to form intricate frictional profiles. The pattered surfaces may have applications in regard to selective adsorption and separation of biological molecules.

ACKNOWLEDGEMENTS

We would like to acknowledge Ray Sweatman for his assistance with spin-coating and with supplying the PDMS materials.

REFERENCES

1. Blach JA, Watson GS, Brown CL, Pham DK, Wright J, Nicolau DV, Myhra S, "A mechanistic approach to tip-induced nano-lithography of polymer surfaces", Thin Solid Films, **459**, 95-99, 2004.
2. Blach-Watson JA, Watson GS, Brown CL, Myhra S, "UV patterning of polyimide: differentiation and characterization of surface chemistry and structure" Applied Surface Science, **235**, 164-169, 2004.
3. Nicolau DV, Taguchi T, Taniguchi H, Yoshikawa S, "Negative and positive tone protein patterning on E-beam/deep-UV resists", Langmuir, **15**, 3845-3851, 1999.
4. Hector LG, Schmid SR, "Simulation of asperity plowing in an atomic force microscope Part I: Experimental and theoretical methods", Wear, **215**, 247-256, 1998.
5. Schmid SR, Hector LG, "Simulation of asperity plowing in an atomic force microscope. Part II: Plowing of aluminium Alloys", Wear, **215**, 257-266, 1998.
6. Fang T-H, Went C-I, Chang J-G, "Machining characterization of the nano-lithography process using atomic force microscopy", Nanotechnology, **11**, 181-187, 2000.
7. Bhushan B, "Nano- to microscale wear and mechanical characterization using scanning probe microscopy", Wear, **251**, 1105-1123, 2001.
8. Pickering JP, Vancso GJ, "On the formation of oriented nanometer scale patterns on amorphous polymer surfaces studied by atomic force microscopy", Applied Surface Science, **148**, 147-154, 1999.
9. Capella B, Sturm H, Weidner SM, "Breaking polymer chains by dynamic plowing lithography", Polymer, **43**, 4461-4466, 2002.
10. Elkaakour Z, Aime JP, Bouhacina T, Odin C, Masuda T, "Bundle formation of polymers with atomic force microscope in contact mode: A friction versus peeling process", Physical Review Letters, **73**, 3231-3234, 1994.
11. Haugstad G, Gladfelter WL, Jones RR, "Scanning force microscopy characterization of viscoelastic deformations induced by precontact attraction in a low cross-link density gelatin film", Langmuir, **14**, 3944-3953, 1998.
12. Schmidt RH, Haugstad G, Gladfelter WL, "Correlation of Nanowear patterns to viscoelastic response in a thin polystyrene melt", Langmuir, **15**, 317-321, 1999.
13. Schmidt RH, Haugstad G, Gladfelter WL, "Scan-induced patterning in glassy polymer films: Using scanning force microscopy to study plastic deformation at the nanometer length scale", Langmuir, **19**, 898-909, 2003.

14. Schmidt RH, Haugstad G, Gladfelter WL, "Scan-induced patterning and the glass transition in polymer films: Temperature and rate dependence of plastic deformation at the nanometer length scale", Langmuir, **19**, 10390-10398, 2003.
15. Xia Y, Whitesides GM, "Soft lithography", Angewandte Chemie International Edition, **37**, 550-575, 1998.
16. Kane RS, Takayama S, Ostuni E, Ingber DE, Whitesides GM, "Patterning proteins and cells using soft lithography", Biomaterials, **20**, 2363-2376, 1999.
17. Brinkmann M, Chan V Z-H, Homas EL, Lee VY, Miller RD, Hadjichristidis N, Avgeropoulos A, "Room-temperature synthesis of a-SiO_2 thin films by UV-assisted ozonolysis of a polymer precursor", Chemical Materials, **13**, 967- 972, 2001.
18. Schnyder B, Lippert T, Kotz R, Wokaun A, Graubner V-M, Nuyken O, "UV-irradiation induced modification of PDMS films investigated by XPS and Spectroscopic Ellipsometry", Surface Science, **532-535**, 1067-1071, 2003.
19. Ikada Y, "Surface modification of polymers for medical applications", Biomaterials, **15**, 725-736, 1994.
20. Kim J, Chaudhury MK, Owen MJ, "Hydrophobicity loss and recovery of silicone HV insulation", IEEE Transactions on Dielectric and Electrical Insulation, **6**, 695-702, 1999.
21. Hillborg H, Gedde UW, "Hydrophobicity changes in silicone rubbers", IEEE Transactions on Dielectric and Electrical Insulation, **6**, 703-717, 1999.
22. Pike JK, Ho T, Wynne K, "Water-induced surface rearrangements of Poly(dimethylsiloxane-urea-urethane) segmented block copolymers", Chemistry of Materials, **8**, 856-860, 1996.
23. Olah A, Hillborg H, Vancso GJ, "Hydrophobic recovery of UV/ozone treated poly(dimethylsiloxane): Adhesion studies by contact mechanics and mechanism of surface modification", Applied Surface Science, **239**, 410–423, 2005.
24. Hu J, Deng T, Beck RG, Westervelt RM, Whitesides GM, "Fabrication of arrays of Schottky diodes using microtransfer molding", Sensors & Actuators A, **75**, 65-69, 1999.
25. Schueller OJA, Brittain ST, Whitesides GM, "Fabrication of glassy carbon microstructures by soft lithography", Sensors & Actuators A, **72**, 125-139, 1999.
26. Deng T, Prentiss M, Whitesides GM, "Fabrication of magnetic microfiltration systems using soft lithography", Applied Physics Letters, **80**, 461-463, 2002.
27. Cleveland JP, Manne S, Bocek D, Hansma PK, "A nondestructive method for determining the spring constant of cantilevers for scanning force microscopy", Review of Scientific Instruments, **64**, 403-405, 1993.
28. Gibson CT, Watson GS, Myhra S, "Scanning force microscopy - calibration procedures for 'best practice'", Scanning, **19**, 564-581, 1997.
29. Sneddon N, "The relation between load and penetration in the axisymmetric boussinesq problem for a punch of arbitrary profile", International Journal of Engineering Science, **3**, 47-57, 1965.
30. Armani D, Liu C, Aluru N, *12th Int. Conf. on MEMS* (Orlando Florida) 222, 1998.
31. McDonald JC, Whitesides GM, "Poly(dimethylsiloxane) as a material for fabrication microfluidic devices", Accounts of Chemical Research, **35**, 491-499, 2002.
32. Roca-Cusachs P, Rico F, Martinez E, Toset J, Farre R, Navajas D, "Stability of microfabricated high aspect ratio structures in Poly(dimethylsiloxane)", Langmuir, **21**, 5542-5548, 2005.
33. Watson GS, Dinte BP, Blach-Watson JA, Myhra S, "Friction measurements using force versus distance friction loops in force microscopy", Applied Surface Science, 235, 38-42, 2004.
34. Mate CM, McClelland GM, Erlandsson R, Chiang S, "Atomic-scale friction of a tungsten tip on a graphite surface", Physical Review Letters, **59**, 1942-1945, 1987.
35. van den Oetelaar RJA, Flipse CFJ, "Atomic-scale friction on diamond (111) studied by ultra-high vacuum atomic force microscopy", Surface Science Letters, **384**, L828-L835, 1997.
36. Garnaes J, Bjornholm T, Zasadzinski JAN, "Nanoscale lithography on langmuir-blodgett films of behinic acid", Journal of Vacuum Science and Technology B, **12**, 1839-1842, 1994.
37. Ling JSG, Leggett GJ, Murray AJ, "Scanning force microscopy of polyester films: Contact versus non-contact imaging and tip-induced wear experiments", Polymer, **39**, 5913-5921, 1998.